

Bimodality and internal variability of the Gulf Stream and the Kuroshio

Bimodaliteit en interne variabiliteit
van de Golfstroom en de Kuroshio
(met een samenvatting in het Nederlands)

PROEFSCHRIFT

TER VERKRIJGING VAN DE GRAAD VAN DOCTOR AAN DE
UNIVERSITEIT UTRECHT OP GEZAG VAN DE
RECTOR MAGNIFICUS, PROF. DR. W.H. GISPEN,
INGEVOLGE HET BESLUIT VAN HET COLLEGE VOOR
PROMOTIES IN HET OPENBAAR TE VERDEDIGEN OP
VRIJDAG 8 JUNI 2001 DES OCHTENDS OM 10.30 UUR

door

MAURICE JOS SCHMEITS

geboren op 4 maart 1971, te Sittard

Promotor: Prof. dr. W.P.M. de Ruijter
Co-promotor: Dr. ir. H.A. Dijkstra
Faculteit Natuur- en Sterrenkunde, Universiteit Utrecht



Dit proefschrift werd mede mogelijk gemaakt door financiële steun van de Nederlandse organisatie voor Wetenschappelijk Onderzoek (NWO).

Cover: Satellite-derived image of the sea surface temperature in the Gulf Stream region near the North American coast on February 27th 2001. The warmest water has been colored orange/red, so that the Gulf Stream is clearly visible. Discernible features are the seaward deflection of the Gulf Stream near $33^{\circ} N$, the separation of the current at Cape Hatteras ($35^{\circ} N$) and a meander of the current between 37° and $39^{\circ} N$. Besides, one warm-core ring and two cold-core rings are visible in the northeastern part of the domain. (Adapted from <http://www.rsmas.miami.edu/environment/imagery>.)

ISBN 90-393-2726-2

Contents

1	Introduction	1
1.1	The ocean circulation	1
1.1.1	Gulf Stream	2
1.1.2	Kuroshio	4
1.2	Traditional model approaches	5
1.3	Bifurcation analysis of intermediate complexity models on a β -plane	6
1.3.1	An equivalent barotropic shallow-water (SW) model	7
1.3.2	The origin of multiple steady states	9
1.3.3	The origin of temporal variability	9
1.3.4	Continental geometry and realistic windstress shape	12
1.4	Central questions addressed in this thesis	16
2	Connection between multivariate time series analysis and bifurcation analysis	19
2.1	Introduction	19
2.2	Bifurcation diagram of the two-layer QG model	20
2.3	Multivariate time series analysis of the two-layer QG model	23
2.4	Discussion	25
3	Bimodal behavior of the Kuroshio and the Gulf Stream	31
3.1	Introduction	31
3.2	Northern hemispheric western boundary currents in POCM	34
3.2.1	Bimodality of the Kuroshio	35
3.2.2	Bimodality of the Gulf Stream	37
3.3	The barotropic shallow-water model	40
3.3.1	Formulation	40
3.3.2	Implementation	41
3.4	Bifurcation analysis of the barotropic shallow-water model	41
3.4.1	Multiple equilibria of the Kuroshio	42
3.4.2	Multiple equilibria of the Gulf Stream	47
3.5	Noise-induced transitions	51
3.5.1	Stochastic windstress forcing	51
3.5.2	Transitions between different paths of the Gulf Stream	53
3.5.3	Transitions between different paths of the Kuroshio	55

3.6	Discussion	56
4	Physics of the 9-month variability in the Gulf Stream region	61
4.1	Introduction	61
4.2	Datasets and their preprocessing	63
4.3	Results of the data analysis	64
4.3.1	Spatiotemporal variability of SST observations	64
4.3.2	Spatiotemporal variability of T/P SSH observations	68
4.3.3	Covarying patterns in SST and T/P SSH observations	71
4.3.4	Spatiotemporal variability of POCM fields	72
4.4	Spatiotemporal variability within the barotropic shallow-water model	77
4.5	Discussion	78
5	Physics of the 7-month variability in the Kuroshio region	83
5.1	Introduction	83
5.2	Datasets and their preprocessing	84
5.3	Results of the data analysis	84
5.3.1	Spatiotemporal variability of T/P-ERS SSH observations	84
5.3.2	Spatiotemporal variability of POCM fields	86
5.4	Spatiotemporal variability within the barotropic shallow-water model	87
5.5	Discussion	91
6	The influence of additive stochastic forcing on the variability in the SW model	95
6.1	Introduction	95
6.2	Multivariate time series analysis of the barotropic SW model with(out) noise	96
6.2.1	North Atlantic	96
6.2.2	North Pacific	100
6.3	Discussion	104
7	Discussion	107
A	Multivariate time series analysis	113
A.1	Multi-channel Singular Spectrum Analysis (M-SSA)	113
A.2	Principal Oscillation Pattern (POP) analysis	114
B	Dynamical systems analysis	117
B.1	Bifurcation theory	117
B.2	Numerical methods	119
	Bibliography	121
	Summary	129
	Samenvatting	131
	Dankwoord	135

Chapter 1

Introduction*

1.1 The ocean circulation

The large-scale ocean circulation is driven both by windstress forcing and by fluxes of heat and freshwater at the ocean-atmosphere surface. The mean pattern of the mainly wind-driven surface circulation is shown in Fig. 1.1. Major features are the equatorial current system, with the eastward Equatorial Countercurrent between westward equatorial currents in both Atlantic and Pacific, the eastward Antarctic Circumpolar Current (ACC), and the large coherent circulation patterns (gyres) at midlatitudes. In the North Atlantic and North Pacific a relatively strong anticyclonic (subtropical) gyre is seen and a relatively weak cyclonic (subpolar) gyre. In the southern hemisphere only the subtropical gyres are seen as a result of the presence of the ACC. Along the western boundaries of the ocean basins strong currents exist. These currents are referred to as western boundary currents and the poleward-flowing currents carry warm water from the tropics to midlatitudes. The major western boundary currents in the North Atlantic and North Pacific are called the Gulf Stream and Kuroshio, respectively. The maximum velocities of these currents occur near the surface, and have a value of $\mathcal{O}(1 \text{ ms}^{-1})$.

Apart from the surface part of the ocean circulation that is mainly wind driven, the deeper part of the ocean circulation is driven mainly by horizontal density gradients, caused by gradients in temperature and salinity, and is called the thermohaline circulation. The Gulf Stream transports relatively warm and saline water which cools and evaporates on its way northward. Because of this cooling and evaporation of already relatively saline water, the water column becomes unstably stratified in certain northern regions, for instance in the Greenland and Labrador Sea, and then vigorous deep convection occurs. A relatively dense water mass (called the North Atlantic Deep Water) is formed which is transported southwards at mid-depth as a deep western boundary current (DWBC). The DWBC crosses the equator and connects to the water masses of the Southern Ocean. Together, the wind-driven and thermohaline ocean circulation form a complex three-dimensional flow of different water masses

*This chapter is partly based on Dijkstra, H. A., M. J. Schmeits, and C. A. Katsman, 1999: Internal variability of the North Atlantic wind-driven ocean circulation. *Surveys in Geophysics*, **20**, 463-503.

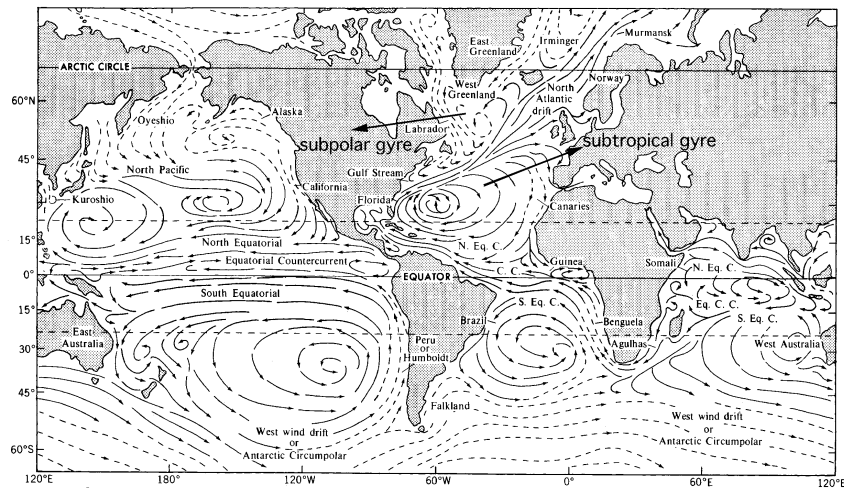


Figure 1.1: Sketch of the global surface (wind-driven) ocean circulation, slightly modified from Peixoto and Oort (1992).

through the ocean basins, which has been termed (Gordon, 1986; Broecker, 1991) the "Ocean Conveyor".

The ocean moderates climate through its large thermal inertia, its large heat capacity and its poleward heat transport by the ocean currents. The total meridional heat transport of the global ocean is about the same as that of the atmosphere, with the North Atlantic and North Pacific heat transport being poleward and of the same order of magnitude. Therefore, changes in the ocean circulation can affect climate substantially. Subtle changes in the North Atlantic and North Pacific surface circulation and their interactions with the overlying atmosphere are likely involved in the interannual through interdecadal variability as observed over the last century. Variations in the mean path of currents like the Gulf Stream are proposed as the cause of climate changes on centennial timescales such as the Little Ice Age (Grove, 1988). Changes in the circulation may also occur on a global scale, involving a transition to different patterns within the "Ocean Conveyor", and these have been suggested to be the cause of large amplitude climate variations in the past, such as the Younger Dryas (Broecker et al., 1985). In the following, we will restrict ourselves to the variability of the mainly wind-driven surface circulation and in particular that within the North Atlantic and North Pacific basins.

1.1.1 Gulf Stream

The most intense current in the North Atlantic Ocean is the Gulf Stream. The position of the Gulf Stream has fascinated oceanographers since its early description by Benjamin Franklin and Timothy Folger (Richardson, 1980). From the enormous amount of data obtained since then, using expendable bathythermograph (XBT) surveys, buoy and ship observations, and

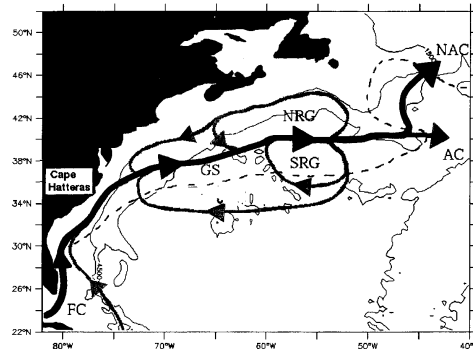


Figure 1.2: Sketch of the mean near-surface circulation, slightly modified from Dengg et al. (1996). Contours denote bathymetry of the Gulf Stream region and dashed is the contour of mean zero wind-stress curl. Bold lines: Florida Current (FC) and Gulf Stream (GS), branching into the North Atlantic Current (NAC) and Azores Current (AC). The abbreviations NRG and SRG indicate the northern and southern recirculation region, respectively.

altimeter and infrared satellite data, the time mean path of the Gulf Stream is quite well known (Auer, 1987). The southern part of the Stream (the Florida Current) flows almost parallel to the coastline (Fig. 1.2). The Gulf Stream near South Carolina, however, can be in a weakly deflected or a strongly deflected state (Fig. 1.3; from Bane and Dewar, 1988), as revealed by satellite images of sea surface temperature (SST) of the North Atlantic. Bane and Dewar (1988) have presented observations which suggest that the seaward deflection of the Gulf Stream has a bimodal character and that the transitions between both states occur on intermonthly timescales. Results from other studies of the Gulf Stream path using in situ measurements and very high resolution infrared satellite data also show indications of bimodal behavior (Olson et al., 1983; Auer, 1987).

At Cape Hatteras, the Gulf Stream leaves the North-American continent and moves further eastward along $40^{\circ} N$. It is accompanied by recirculation regions to the north (Hogg et al., 1986) and the south, indicated by NRG and SRG in Fig. 1.2. Despite the possible bimodal behavior of the Gulf Stream near South Carolina, the position of the separation point appears to be quite stable, changing less than about 50 km over several years (Auer, 1987). Further into the open ocean, the Gulf Stream spreads out due to meandering and displays an enormous amount of variability. In this area, eddies are formed which move away from the main stream, generally in westward/southwestward direction. Their average wavelength is about 200 km and propagation speeds of these eddies are about 5 km day^{-1} . Near Cape Hatteras, the volume transport of the Gulf Stream is estimated to be about 50-65 Sv ($\text{Sv} \equiv 10^6 \text{ m}^3 \text{ s}^{-1}$), which increases to a total of about 145 Sv at $60^{\circ} W$ (Johns et al., 1995). After crossing the Southeast Newfoundland Ridge (at about $50^{\circ} W$) the Gulf Stream splits into two branches: the northern branch becomes the North Atlantic Current, and the southern one the Azores Current (Fig. 1.2; Dengg et al., 1996).

Recently, satellite-derived observations, for example from a seven-year period of the AVHRR mission (Lee and Cornillon, 1995), have provided a wealth of information about

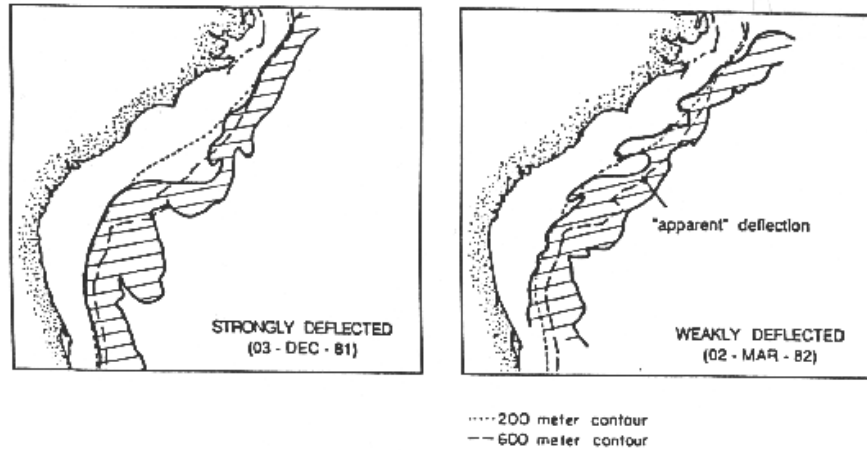


Figure 1.3: Locations of the Gulf Stream on December 3, 1981, and March 2, 1982, during the Gulf Stream Deflection and Meander Energetics Experiment (DAMEX). These retraced versions of the AVHRR SST images from those dates show the stream in a typical strongly deflected configuration (December 3) and weakly deflected configuration (March 2) in the region of the Charleston bump. (From Bane and Dewar, 1988).

variability of the Gulf Stream. Using infrared images for the period April 1982 through December 1989, Lee and Cornillon (1995) found two dynamically distinct modes of variability of the path of the Gulf Stream. The first mode of variability is associated with large-scale lateral shifts of the mean path having an annual period. These shifts are presumably caused by atmospheric forcing. The second mode of variability is associated with changes in meandering intensity, having a 9-month dominant periodicity, and is proposed to be related to internal oceanic dynamics (Lee and Cornillon, 1995).

1.1.2 Kuroshio

The most intense current in the North Pacific Ocean is the Kuroshio. Its time mean path is also quite well known nowadays. From observations, it is found that the Kuroshio path exhibits bimodal behavior to the south of Japan with transitions occurring between a small and a large meander state (Fig. 1.4; adapted from Taft, 1972). Both states can persist over a period ranging from a few years to a decade and transitions between them occur within a couple of months (Kawabe, 1986). The mean zonal geostrophic transport of the Kuroshio is estimated to be about 52 Sv at 137° E (Qiu and Joyce, 1992). At the southeast corner of Honshu, the Kuroshio separates from the Japanese coast and flows eastward, while meandering increases. However, the current keeps a mean latitudinal position of about 35° N up to 180° E.

Similar to the 9-month variability in the Gulf Stream region (Lee and Cornillon, 1995), near-annual variability is also found in recent studies of the Kuroshio Extension (Kelly et al., 1996; Wang et al., 1998). Wang et al. (1998) have used four years of satellite altimeter

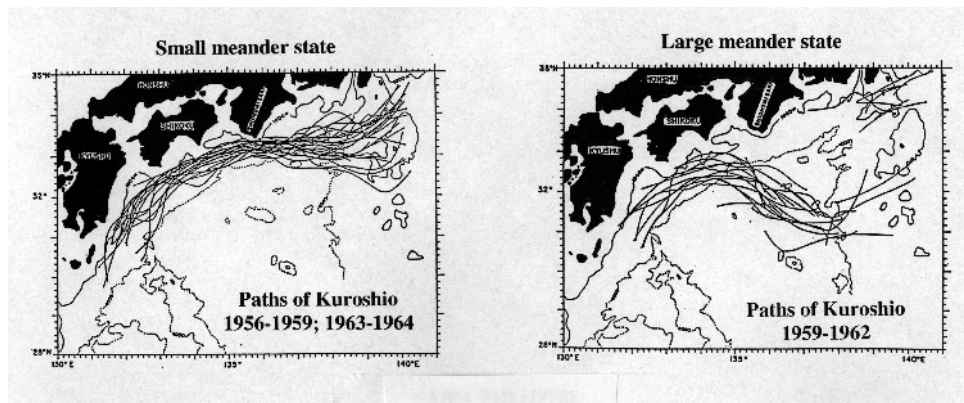


Figure 1.4: Examples of paths of the Kuroshio in its small meander state (left panel) and in its large meander state (right panel). The 1000 m (solid) and 4000 m (dotted) contours are also shown. (Adapted from Taft, 1972).

data from the TOPEX/Poseidon (T/P) exact repeat mission (ERM) together with 2.3-yr data from the GEOSAT ERM. The authors speculate that instability and/or external forcing might be responsible for the generation of the intra-annual variability. They conclude further that bottom topography plays a role in the generation of the intra-annual variability as well. Using both ECMWF atmospheric fields and GEOSAT data, Kelly et al. (1996) also found variability of both the Gulf Stream and the Kuroshio path with timescales of 5-9 months. For both western boundary currents, they found correlations between the height difference across the jet (surface transport) and the path which suggest that there are structural changes in the recirculation gyres, associated with a path change. They concluded that, at least in the North Atlantic, the structural changes in the recirculation gyres may not be related to surface heat flux variations.

Both the mean path of the northern hemispheric western boundary currents as well as the spatiotemporal patterns of their variability are important ingredients to understand the changes in meridional heat transport in the North Atlantic and North Pacific. It is these two different themes which have been focus of theoretical research over the last decades, encompassing work using numerical ocean models and more fundamental theory.

1.2 Traditional model approaches

The Gulf Stream and the Kuroshio are the major western boundary currents of the North Atlantic and North Pacific, respectively. Stommel (1948) and Munk (1950) were the first to explain the intensification of western boundary currents in the ocean using steady linear (quasigeostrophic) rectangular basin models with vertical sidewalls. In these models, balances between lateral or bottom friction, the variation of the Coriolis acceleration with latitude (the β -effect) and the curl of the windstress are studied. On the basin scale, the dominant balance is that between the curl of the windstress and the β -effect, the so-called Sverdrup

balance, leading to the typical gyre structure, and boundary layers in the west are needed to close the circulation. Either lateral or bottom friction is able to generate a boundary layer in the west, giving the Munk or Stommel boundary layer structure, respectively. Recently, Hughes (2000) has given a theoretical argument which shows that, in an ocean with sloping instead of vertical sidewalls, bottom pressure torques are able to balance the windstress curl at each latitude. This removes the requirement for a viscous western boundary current at each latitude suggesting that the dynamics within a western boundary current may be essentially inviscid. When nonlinearities due to advection of vorticity are included, they introduce north-south asymmetries and are responsible for strong recirculation regions. In the fully inertially dominated regime, special type of motion may occur, i.e. Fofonoff modes (Fofonoff, 1954) or modon type solutions (Stern, 1975). Especially in this regime, sensitivities arise to the type of boundary conditions (no-slip versus slip) and the parameterization of frictional processes (Pedlosky, 1996).

In reality, the flows are unsteady, one of the reasons being that they are susceptible to instabilities. Progress in the understanding of two dominant instability mechanisms in geophysical flows, i.e. barotropic and baroclinic instability, has been obtained through their study in β -plane channels (Pedlosky, 1987). In the case of barotropic (baroclinic) instability, the energy is drawn from the kinetic (potential) energy of the basic state associated with the existence of horizontal (vertical) shear. The growth of perturbations and their interaction with the background state (and with each other) leads to a rectification of the mean state and synoptic scale time-dependent features, generally referred to as oceanic eddies. Over the last decades, eddy-resolving ocean models have been developed which are able to produce many features observed in reality, e.g. the formation and propagation of the eddies (Holland and Rhines, 1980; McWilliams, 1996). Although much of the observed variability may be forced by atmospheric noise, results from eddy-resolving models indicate that intrinsic variability of the ocean is large, not only in the region of strong currents but over the whole basin (Miller et al., 1987). Ocean general circulation models (OGCMs), having a realistic continental geometry and bathymetry, are run now with an eddy-permitting resolution on a global scale (Semtner and Chervin, 1992; Stammer et al., 1996; Maltrud et al., 1998), and with a truly eddy-resolving resolution for the Atlantic (Chassignet et al., 2001; Smith et al., 2000; Hurlburt and Hogan, 2000) and the Pacific (Hurlburt et al., 1996). These results show large internal variability on a wide range of timescales and the influence of the eddies on the mean flow. The interpretation of results of these models is not without problems, because of the multitude of physical effects which can influence a phenomenon under study. Many parameter studies which have been performed with idealized models cannot easily be done with these OGCMs.

1.3 Bifurcation analysis of intermediate complexity models on a β -plane

Transition phenomena in models depending on parameters are subject of the theory of dynamical systems (Guckenheimer and Holmes, 1983). This theory provides a catalogue of possible behavior of solutions as parameters are changing in a particular model. Using the mathematical tools of this theory, the phase-parameter space of a particular model can be explored

systematically from the simplest states with a high degree of symmetry to highly complex realistic ones with a much lower symmetry in both space and time (Ghil and Childress, 1987). Transitions between different regimes of behavior occur through so-called bifurcations, while within a particular regime, the behavior is only modified quantitatively. A graph in which the variation of the solutions of a particular problem is displayed in the state-control parameter space is called a bifurcation diagram. The reader is referred to Appendix B for an introduction to bifurcation theory and the numerical methods used to compute steady-state solutions and their linear stability.

1.3.1 An equivalent barotropic shallow-water (SW) model

A first systematic analysis of the nonlinear behavior of western boundary currents, with emphasis on multiple equilibria and low-frequency variations, was carried out by Jiang et al. (1995). They used a reduced-gravity SW model consisting of a rectangular ocean basin on a midlatitude β -plane with Coriolis parameter f ($f = f_0 + \beta_0 y$), forced by a steady double-gyre windstress forcing. In this model, a dynamically active layer of variable thickness h with mean depth D and density ρ is situated above a motionless, infinitely deep and slightly heavier layer having a density $\rho + \Delta\rho$. The interface between the two layers, representing the thermocline, is able to deform; the reduced gravity g' is given by $g' = g\Delta\rho/\rho$. Lateral friction and bottom friction are the only dissipative mechanisms. Hence, in this model the stratification and the description of subgrid-scale mixing processes are highly simplified. Most of their results were obtained with no-slip boundary conditions. The reader is referred to Jiang et al. (1995) (their Table 1) for a list of values of the dimensional parameters they used.

Jiang et al. (1995) integrated the equations in time for different values of the windstress forcing strength α_τ and monitored the position of the confluence point, i.e., the merging point of the two separated western boundary currents, for each solution. They proposed the bifurcation diagram as in Fig. 1.5, using a horizontal resolution of 20 km. The solution structure corresponds to an imperfect pitchfork bifurcation, because the different branches are unconnected but have the appearance of a pitchfork. For small values of α_τ , a unique nearly symmetric (with respect to the mid-axis of the basin) flow was found. For $\alpha_\tau > 0.72$, multiple steady solutions were found, having either a southward or a northward displaced confluence point with respect to the mid-axis of the basin (Fig. 1.6).

Both steady solutions become unstable at larger windstress strength, and stable periodic solutions were found. One of these solutions has a period of about 2.8 years associated with an oscillation of the confluence point over a distance of about 100 km. For even larger values of α_τ , aperiodic solutions were obtained for which the position of the confluence point can make rather large excursions.

The Jiang et al. (1995) study was followed up by the work of Speich et al. (1995), in which the bifurcation structure of the 1.5-layer shallow-water model was determined using continuation techniques (Appendix B.2). The advantage of these methods is that unstable steady states can be determined and hence, the exact position of the limit point and the Hopf bifurcations destabilizing the steady states (Fig. 1.5) can be determined. In the following subsections, the physics of the origin of the multiple equilibria and of the temporal variability will be discussed subsequently.

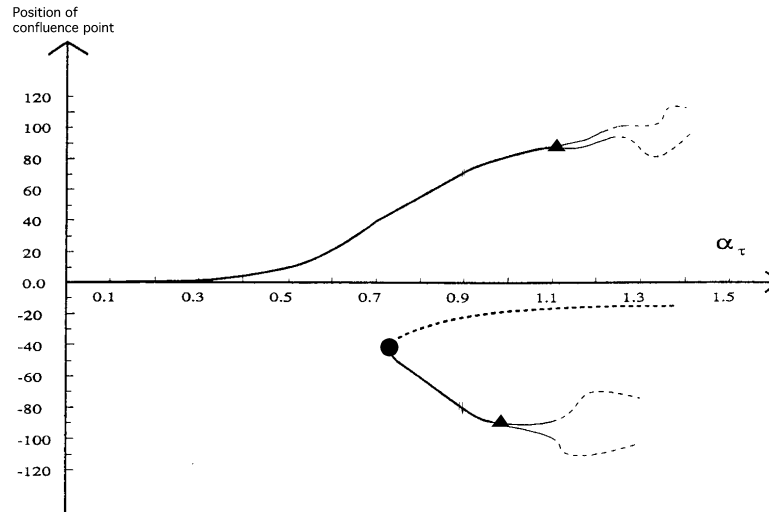


Figure 1.5: Bifurcation diagram (slightly modified from Jiang et al., 1995) to explain the solutions found in the shallow-water model by forward time integration. On the vertical axis, the position of the confluence point (see Fig. 1.6) is plotted, whereas on the horizontal axis, a measure of the windstress strength α_τ is shown. Drawn lines are actually computed values of the confluence point, but dotted lines represent unstable states, which can be guessed based on generic situations in bifurcation theory, but which cannot be computed using forward time integration of the model. The limit point is marked by a filled circle and the Hopf bifurcations by filled triangles.

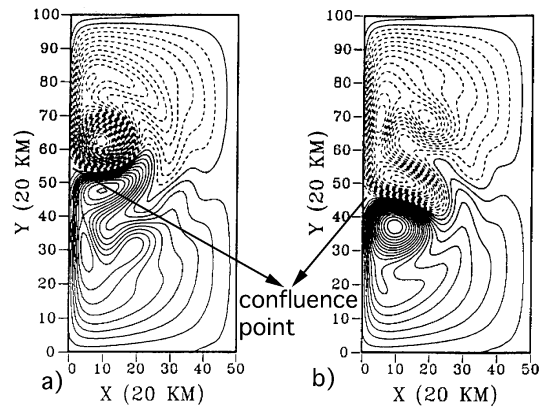


Figure 1.6: Patterns of the layer thickness anomaly of two steady-state solutions of the 1.5-layer shallow-water model at $\alpha_\tau = 0.9$ (slightly modified from Jiang et al., 1995). The position of the confluence point is indicated.

1.3.2 The origin of multiple steady states

In the shallow-water model of the double-gyre circulation, multiple equilibria occur because of an imperfect pitchfork bifurcation (Fig. 1.5). However, there is a simpler model where a perfect pitchfork bifurcation is present. When the Rossby number is small the shallow-water model can be simplified, leading to quasigeostrophic (QG) theory (Pedlosky, 1987). In this theory, the flow is described by a potential vorticity equation. For a rectangular basin, the unforced potential vorticity equation and the no-slip boundary conditions have a reflection symmetry with respect to the mid-axis of the basin (Dijkstra and Molemaker, 1999). Since the applied idealized double-gyre wind forcing admits a similar symmetry, pitchfork bifurcations are expected as symmetry breaking bifurcations.

Indeed, Cessi and Ierley (1995) found pitchfork bifurcations (and hence multiple equilibria) through computation of stationary solutions of the barotropic potential vorticity equation over a large range of conditions. Although Cessi and Ierley (1995) investigated the stability to stationary perturbations, they excluded oscillatory perturbations, and hence no complete picture of the stability of the steady states was given. Therefore, their work was followed up by Dijkstra and Katsman (1997), in which the bifurcation structure of the QG model was determined using continuation techniques. A typical bifurcation diagram for the barotropic case with no-slip (slip) boundary conditions at the east-west (north-south) boundaries is shown in Fig. 1.7. In this figure, the value of the streamfunction at a particular gridpoint (ψ_{SW}) is plotted versus the Reynolds number $Re = U_{QG}L/A_H$, where $U_{QG} = 10^{-2} \text{ ms}^{-1}$ denotes a typical velocity scale for a square basin with length scale $L = 1000 \text{ km}$, and A_H denotes the lateral friction coefficient. At large values of A_H (small Re) there is only one unique state, which is the symmetric double gyre pattern (Fig. 1.8a). When friction is decreased, this flow becomes unstable at the pitchfork bifurcation P_1 and two stable asymmetric states (Figs. 1.8b-c) appear for smaller values of A_H (larger Re). The solutions on these branches have the jet displaced either southward or northward similar to those in Fig. 1.6, but these solutions are now exactly symmetrically related. For even smaller friction, the flow becomes inertially dominated (Fig. 1.8d). The asymmetric branches arising from the pitchfork bifurcation P_2 are not shown because all these solutions are unstable.

The origin of the multiple equilibria is the spontaneous symmetry breaking in the solution structure of the symmetric system. The associated physical mechanism (Dijkstra and Katsman, 1997) involves an asymmetric weakening/strengthening of the subpolar/subtropical gyre with a positive feedback from the resulting change in horizontal shear. Dijkstra and Molemaker (1999) have concluded that the occurrence of multiple equilibria in the SW model has its origin in the symmetry breaking within the QG model and hence the physics of their occurrence is the same. On the branches in Fig. 1.7, several limit points and Hopf bifurcation points also occur and the latter will be discussed in the next subsection.

1.3.3 The origin of temporal variability

As lateral friction is decreased in the QG model, the asymmetric steady states become unstable to an oscillatory instability at the Hopf bifurcations H_1 and H_2 (Fig. 1.7). Also in the SW model, Hopf bifurcations destabilize the steady solutions for decreasing friction or equivalently increasing forcing (Fig. 1.5). In this section, we address the origin of these Hopf

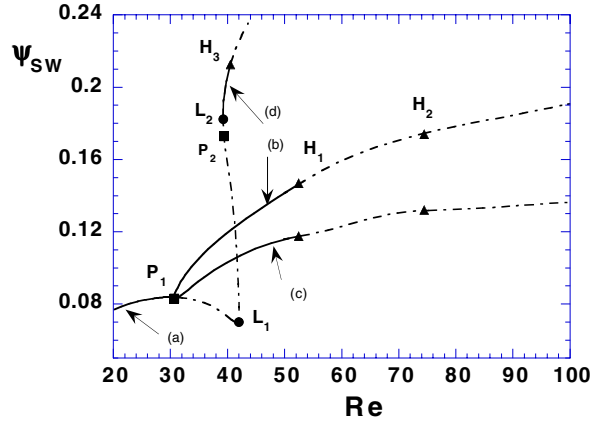


Figure 1.7: Bifurcation diagram for the barotropic QG model for a square basin with $L = 1000$ km and $Re = U_{QG}L/A_H$ as the control parameter. Values of the other parameters can be found in Dijkstra and Katsman (1997).

bifurcations and the timescales of the oscillatory instabilities.

The pattern of the most unstable oscillatory mode can be determined from the solution of the linear stability problem (Appendix B.2: Eq. (B.10)). The corresponding complex eigenfunction $\hat{\mathbf{x}} = \hat{\mathbf{x}}_R + i\hat{\mathbf{x}}_I$ provides the oscillatory perturbation structure $\Xi(t)$ with angular frequency σ_i and growth rate σ_r to which the steady state may become unstable, i.e.

$$\Xi(t) = e^{\sigma_r t} [\hat{\mathbf{x}}_R \cos(\sigma_i t) - \hat{\mathbf{x}}_I \sin(\sigma_i t)] \quad (1.1)$$

Propagation features of a neutral mode ($\sigma_r = 0.0$) can be determined by first looking at $\Xi(-\pi/(2\sigma_i)) = \hat{\mathbf{x}}_I$ and then at $\Xi(0) = \hat{\mathbf{x}}_R$. The period p of the oscillation is given by $p = 2\pi/\sigma_i$.

The mode that destabilizes at the first Hopf bifurcation H_1 in the QG model (Fig. 1.7) has an intermonthly timescale, whereas at the second Hopf bifurcation H_2 an interannual mode destabilizes. The intermonthly mode (Fig. 1.9a) has a basin wide pattern. For the interannual mode (Fig. 1.9b) the perturbation has the characteristic asymmetry of the steady state gyre structure.

Where does the timescale of both type of modes come from? In an unbounded ocean, large time and space scale phenomena are set by Rossby waves. In a frictionless barotropic QG model, free modes are described by

$$\frac{\partial}{\partial t} \nabla^2 \psi + \beta_0 \frac{\partial \psi}{\partial x} = 0 \quad (1.2)$$

with kinematic conditions $\psi = 0$ at the lateral boundaries. The structure and dispersion relation of these modes in a closed rectangular basin with size $L \times 2L$ are given by (Pedlosky, 1987)

$$\psi = \Psi_0 \sin \frac{n\pi x}{L} \sin \frac{m\pi y}{2L} e^{-i(\sigma_{nm} t + \frac{\beta_0 x}{2\sigma_{nm}})} \quad (1.3a)$$

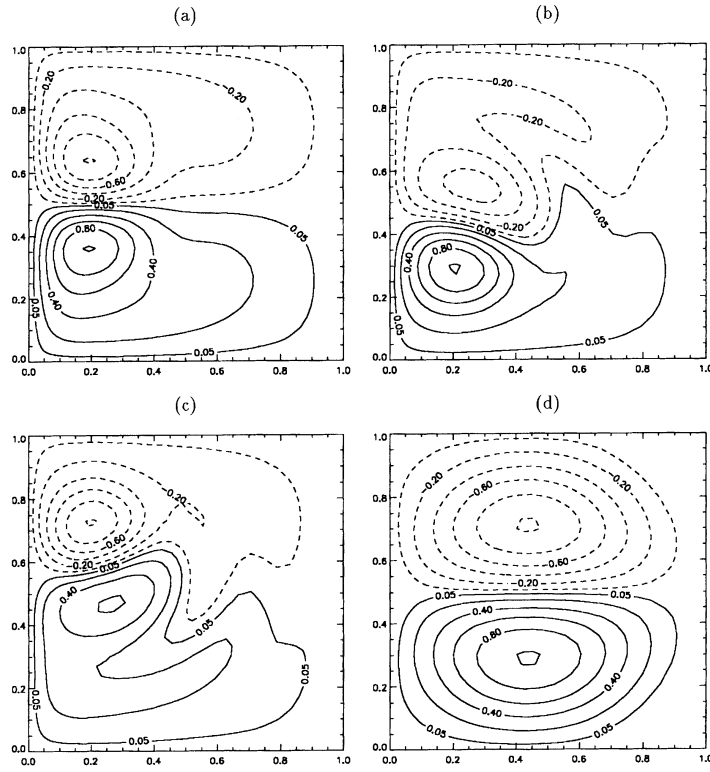


Figure 1.8: Solutions for the streamfunction ψ at labelled points a-d in Fig. 1.7. All contour plots are scaled with the absolute maximum and the contour levels are with respect to this maximum. Along the axes, the dimensionless quantities x/L and y/L are shown.

$$\sigma_{nm} = \frac{\beta_0 L}{\sqrt{2((n\pi)^2 + (m\pi/2)^2)}} \quad (1.3b)$$

where Ψ_0 is an arbitrary amplitude and the indices (n, m) refer to the spatial structure of these basin modes. For typical values of the parameters, the gravest barotropic ocean basin mode $(n, m) = (1, 1)$, having spatial structure in both horizontal directions, the timescale is about 20 days. It can be expected that friction slightly increases this timescale of propagation. Exactly these free modes are destabilized through the presence of horizontal shear to lead to the intermonthly basin modes as found in the QG model. Their pattern is indeed basin wide as are the Rossby basin modes, they propagate westward, the period of propagation has the same timescale and they have therefore been called (unstable) ocean basin modes (Fig. 1.9a; Dijkstra and Katsman, 1997).

On the contrary, the interannual mode (Fig. 1.9b) seems to have no origin related to free mode propagation. The pattern of this mode already indicates a close orientation within the gyres and the interannual timescale of this mode is very likely related to the circula-

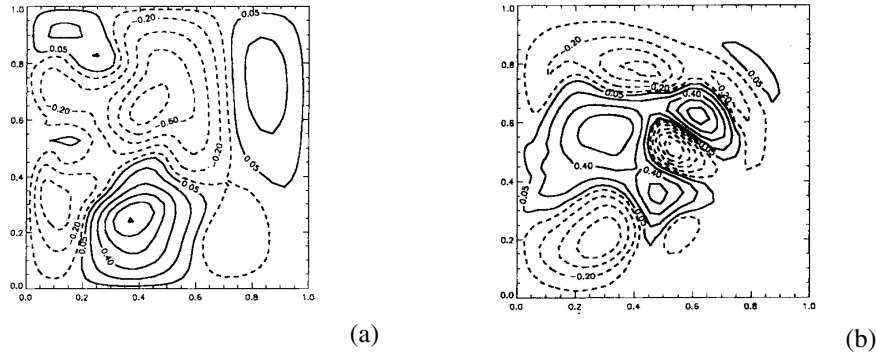


Figure 1.9: Snapshot of the neutral streamfunction perturbation corresponding to $\Xi(0)$ at the Hopf bifurcation H_1 (Fig. 1.7). (b) Same as (a) but for the mode at H_2 . Note that the amplitudes of both modes are arbitrary.

tion timescale within the gyres which is in the order of 3 years. An attempt to describe the mechanism of propagation can be found in Speich et al. (1995). Although this mode can be destabilized by horizontal shear at small friction it disappears when the gyres become very weak; it therefore has been called (unstable) gyre mode (Dijkstra and Katsman, 1997).

For the SW model, three modes become unstable nearly at the same conditions at the Hopf bifurcation H_1 (Dijkstra and Molemaker, 1999, their Fig. 5). The basic state at H_1 is very similar to Fig. 1.6b and is therefore not shown. The real part of the first two eigenmodes is shown in Fig. 1.10. The first mode (Fig. 1.10a) is neutral and its period is approximately 5 months. The pattern shows a maximum response located to the north of the mid-axis and the mode propagates westward. When the Rossby deformation radius and basin size are adjusted, it can be shown to deform into the basin mode of the QG model in Fig. 1.9a (Dijkstra et al., 1999). The second mode (Fig. 1.10b) has a period of about 1.5 years, it is slightly damped and its pattern shows a propagation of the perturbations southwestward. It is similar to the gyre mode of the QG model in Fig. 1.9b (Dijkstra et al., 1999). The third mode (not shown) is also slightly damped and has a similar period (3.7 months) as the first mode. The modes at the Hopf bifurcation H_2 (Dijkstra and Molemaker, 1999, their Fig. 5) have very similar timescales and patterns as those at H_1 , and the basic state is very similar to Fig. 1.6a. It can be concluded that the modes of variability of the SW and QG model are closely linked (Dijkstra and Molemaker, 1999).

Certainly, these bifurcation studies would be quite academic if all features would be lost in more realistic settings, i.e. when stratification, continental geometry, realistic windstress shape, bottom topography etc. are included. In the next subsection, this matter of robustness is addressed with respect to the inclusion of continental geometry and realistic windstress shape.

1.3.4 Continental geometry and realistic windstress shape

Dijkstra and Molemaker (1999) have incorporated schematically - because of the finite ele-

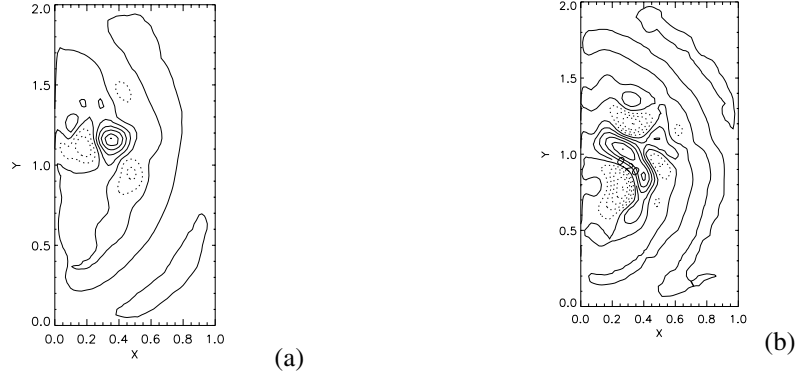


Figure 1.10: First two eigenmodes at the Hopf bifurcation H_1 (Dijkstra and Molemaker, 1999, their Fig. 5). On the axes, the dimensionless quantities x/L and y/L are shown again. (a) Layer thickness perturbations h for the real part of the most unstable mode with $\sigma_r = 0.0 \text{ yr}^{-1}$ and $\sigma_i = 16.4 \text{ yr}^{-1}$. (b) as above but for the 2nd mode ($\sigma_r = -1.1 \text{ yr}^{-1}$, $\sigma_i = 4.1 \text{ yr}^{-1}$). Again, the amplitude is arbitrary for both modes.

ment discretization - the geometry of the North Atlantic basin in a 1.5-layer SW model on a β -plane and forced the model with the annual mean windstress from the Hellerman and Rosenstein (1983) dataset. For quite realistic values of the parameters (Dijkstra and Molemaker, 1999, their Table 2) the bifurcation diagram is shown in Figure 1.11 using the Ekman number $E = A_H/f_0L^2$ as control parameter. On the vertical axis, the maximum northward volume transport Φ (in Sv) over a section is shown which is calculated as

$$\Phi = \max \left[\int_0^{x_e} v h \, dx \right] \quad (1.4)$$

where the maximum is taken both over y and x_e , and v denotes the meridional velocity component.

Main result is the existence of multiple equilibria, just as in the rectangular geometry considered in subsection 1.3.1 (Fig. 1.5). Two solution branches are found, on which solutions are unstable for $E < 7.5 \cdot 10^{-6}$. One of the branches is connected to the large E regime and a solution on this branch is shown for $E = 3.0 \cdot 10^{-6}$ in Fig. 1.11b. The Gulf Stream flows northward along Cape Hatteras and turns into the open ocean at slightly northerly latitudes giving a transport Φ of about 21.5 Sv. There is a very weak northern recirculation region at this value of E . The other branch exists only for values of E smaller than $3.2 \cdot 10^{-6}$, which is the position of the limit point on this branch. The solution at $E = 3.0 \cdot 10^{-6}$ (Fig. 1.11c) displays a Gulf Stream which turns into the open ocean near Cape Hatteras. There is now a northern recirculation region, although too much concentrated near the coast compared to reality. At this value of E , the maximum transport of this "separated" Gulf Stream is about 26.2 Sv, which is larger than that of the "deflected" Gulf Stream (Fig. 1.11b). It can be concluded that the multiple steady-state solutions of the Gulf Stream in the shallow-water model with basin geometry are deformations of the "jet up" and "jet down" solutions, which are the

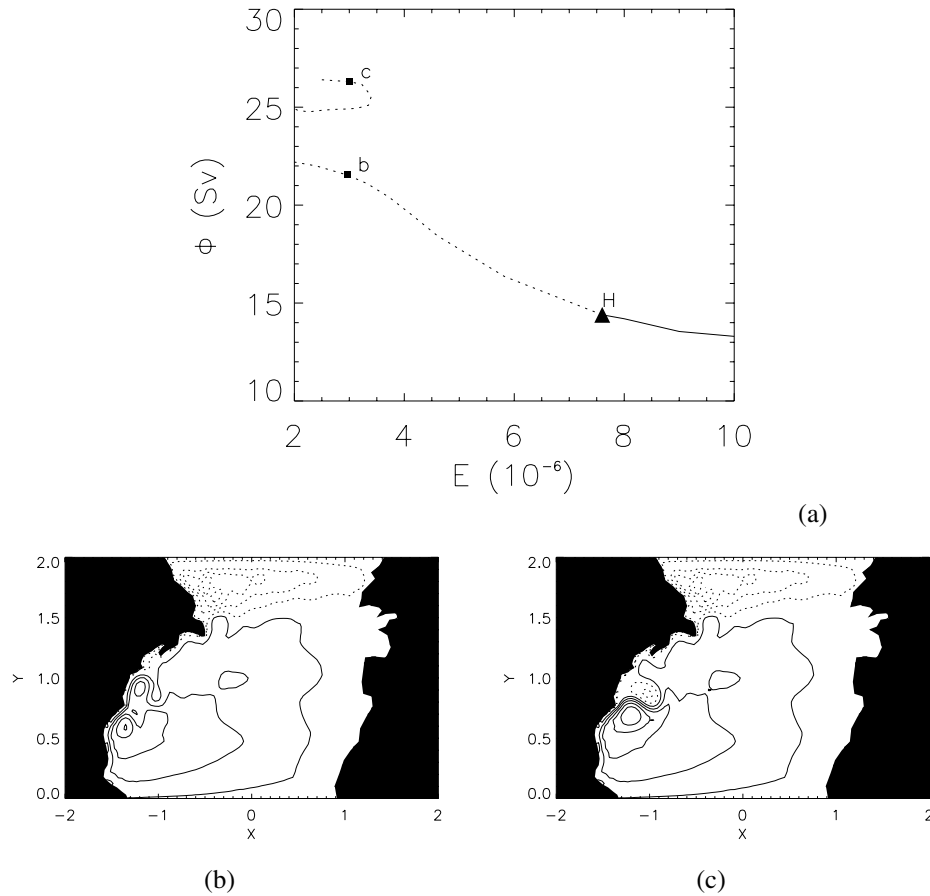


Figure 1.11: Bifurcation diagram for the 1.5-layer shallow-water model (Dijkstra and Molemaker, 1999), with a representation of the continents and with realistic wind forcing. The Ekman number $E = A_H / (f_0 L^2)$ is the control parameter; drawn (dotted) branches indicate stable (unstable) steady states. (b) Contour plot of the layer thickness anomaly for the "deflected" Gulf Stream at $E = 3.0 \times 10^{-6}$. The field is scaled with its absolute maximum and contours are with respect to this maximum. The lateral coordinates x and y are scaled by the basin length scale L . (c) Contour plot of the layer thickness anomaly for the "separated" Gulf Stream at $E = 3.0 \times 10^{-6}$.

multiple equilibria in the rectangular basin case (Figs. 1.6 and 1.8b-c). This strongly suggests that the simultaneous existence of the "deflected" and "separated" Gulf Stream is not due to continental geometry, but is strongly controlled by internal dynamics (Dijkstra et al., 1999).

The first Hopf bifurcation is found at $E = 7.5 \times 10^{-6}$ on the branch of the "deflected" Gulf Stream solution (H in Fig. 1.11a). At $E = 3.0 \times 10^{-6}$, the "deflected" solution in Fig. 1.11b is unstable to only one oscillatory mode. The real and imaginary part of the eigenvector of this

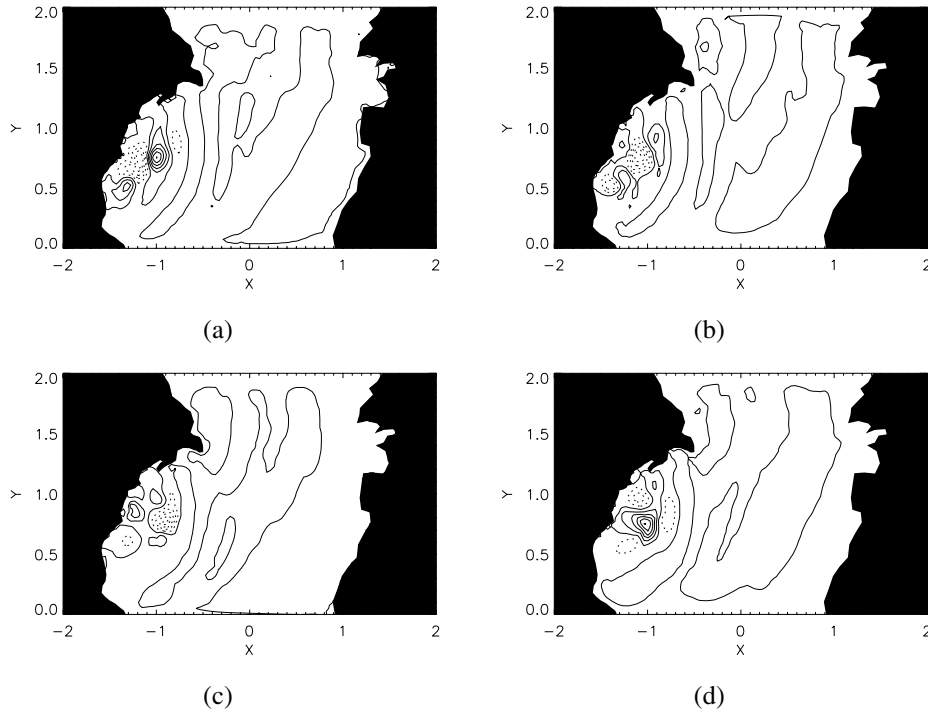


Figure 1.12: *Eigenfunctions corresponding to the unstable mode at the marked points in Fig. 1.11a for $E = 3.0 \cdot 10^{-6}$; shown are the layer thickness perturbations (from Dijkstra and Molemaker, 1999). (a-b): Real and imaginary part of the unstable oscillatory mode on the steady state shown in Fig. 1.11b, with $\sigma_r = 2.2 \text{ yr}^{-1}$ and $\sigma_i = 16.1 \text{ yr}^{-1}$. (c-d): As in (a-b) but for the steady state shown in Fig. 1.11c, with $\sigma_r = 0.47 \text{ yr}^{-1}$ and $\sigma_i = 19.2 \text{ yr}^{-1}$.*

mode are shown in Figs. 1.12a-b; the period of oscillation is about 5 months. The center of action for the oscillation is located in the Gulf Stream region and the scale of the perturbations is about 500 km. The orientation of the perturbations does not appear directly related to the orientation of the jet itself. The disturbances propagate south-westward against the flow direction of the mean current of the steady state. The "separated" solution (Fig. 1.11c) is also unstable to only one oscillatory mode (Figs. 1.12c-d) having a period of about 4 months. Thickness perturbations with a scale of about 400 km are again localized in the jet and the response outside the jet is weak. It can be concluded that the timescales of these modes does not depend much on the continental geometry and windstress and even their pattern is not strongly modified (cf. Fig. 1.10a). The reason is that already in rectangular geometry, these modes are strongly localized within the high shear regions of the gyre, which basically does not change through the range of different models (Dijkstra et al., 1999).

1.4 Central questions addressed in this thesis

Within a hierarchy of equivalent barotropic models on a β -plane (section 1.3), it is found that multiple mean flows are dynamically possible for the North Atlantic wind-driven circulation. The existence of these multiple mean paths can be traced back to its origin: a symmetry breaking pitchfork bifurcation within the barotropic quasigeostrophic double gyre flow in a rectangular basin (Dijkstra and Molemaker, 1999). One underlying (optimistic) idea in applying dynamical systems theory to understand internal variability of the wind-driven ocean circulation, is that stationary equilibria play an important role in determining the mean state of the real system (Dijkstra et al., 1999) or in other words that steady states, although unstable, act to guide the trajectory in phase space (Legras and Ghil, 1985).

For the barotropic North Atlantic circulation, the modes of variability arising as instabilities on the mean states are closely linked within the hierarchy of the quasigeostrophic and shallow-water models as presented above (section 1.3; Dijkstra and Molemaker, 1999). In the range of parameters studied, there are only a few modes which contribute to the dynamics; these are the barotropic basin and gyre modes. Application of dynamical systems theory to the issue of temporal variability in the wind-driven ocean circulation requires the (optimistic) view that each mode of temporal variability can be traced back to originate from one specific Hopf bifurcation, which can be studied in isolation within a certain minimal model (Dijkstra et al., 1999).

By going through the hierarchy of models, one has gotten an idea of the robustness of these phenomena and has a clear entrance to understand their physics. However, a legitimate question is how relevant these results are for the actual ocean circulation. This is the main topic addressed in this thesis which is further specified as follows.

Given the observed (possible) bimodal behavior of the Kuroshio (Gulf Stream) (Figs. 1.3 and 1.4) and the existence of multiple steady states of the Gulf Stream in an equivalent barotropic SW model on a β -plane (Fig. 1.11; Dijkstra and Molemaker, 1999), the main question addressed in chapter 3 is:

(i) Can the observed (possible) bimodal behavior of the Kuroshio (Gulf Stream) be explained by transitions between multiple steady states, as suggested by Charney and Flierl (1981) and Masuda (1982) for the Kuroshio?

More specifically:

- Are there signatures of multiple steady states of the Kuroshio and the Gulf Stream in eddy-permitting OGCMs?
- Are there (transitions between) multiple steady states of the Kuroshio and the Gulf Stream in a SW model on the sphere with similar patterns compared to those in the observations and eddy-permitting OGCMs?
- What are the physical processes responsible for this bimodal behavior?

Given the observed variability of the Gulf Stream and the Kuroshio on intermonthly timescales (subsections 1.1.1 and 1.1.2) and the existence of unstable intermonthly modes in the Gulf Stream separation region in results of an equivalent barotropic SW model on a

β -plane (Fig. 1.12; Dijkstra and Molemaker, 1999), the main question addressed in chapter 4 (for the Gulf Stream) and chapter 5 (for the Kuroshio) is:

(ii) *Can the observed variability of the Gulf Stream and the Kuroshio on intermonthly timescales be explained by instabilities of the wind-driven ocean circulation?*

More specifically:

- Is there (statistically significant) spatiotemporal variability of the Gulf Stream and the Kuroshio on these timescales in observations and eddy-permitting OGCMs?
- Are there oscillatory instabilities of the mean Gulf Stream and Kuroshio flow in a SW model on the sphere with similar spatial and temporal scales compared to those in the observations and eddy-permitting OGCMs?
- What are the physical processes responsible for variability on these timescales?

The approach that will be followed in chapters 3-5 to answer these questions is to combine data analysis of observations and OGCMs, and dynamical systems analysis of intermediate complexity models. This approach is new, and therefore the connection between both types of analyses will be studied in chapters 2 (*a priori*) and 6 (*a posteriori*).

In chapter 2 the connection between multivariate time series analysis (Appendix A) and bifurcation analysis (Appendix B) will be studied in the context of a two-layer QG model. The bifurcation structure of this model has been studied systematically (Dijkstra and Katsman, 1997), and therefore the statistical modes from the multivariate time series analysis can be compared with the neutral dynamical modes from the linear stability analysis. In other words, we like to know whether the statistical modes have dynamical significance, at least in a "simple" QG model. This question is important for the studies in chapters 4 and 5 using multivariate time series analysis for the analysis of observations and output from an OGCM, because the patterns found in the latter will be linked to the variability associated with the oscillatory instabilities in the SW model on the sphere. To find the dominant spatiotemporal patterns in the two-layer QG model, two analysis techniques will be used in order to make an intercomparison of their skills: Multichannel Singular Spectrum Analysis (M-SSA) (Plaut and Vautard, 1994) and Principal Oscillation Patterns (POPs) (Hasselmann, 1988; Von Storch et al., 1995) (which are described in Appendix A).

In chapter 6, the connection between multivariate time series analysis and bifurcation analysis will be studied in the context of the SW model on the sphere with(out) additive stochastic forcing. The bifurcation structure of this model will be determined in chapters 3-5, and therefore the dominant (and/or statistically significant) statistical modes can be compared with the neutral dynamical modes. More specifically, we will investigate whether the oscillatory modes that become unstable at Hopf bifurcations can still be found in the presence of additive stochastic forcing.

One of the problems associated with the approach of combining analyses of observations, eddy-permitting OGCMs and intermediate complexity models, is that the mean state of eddy-permitting OGCMs and of intermediate complexity models differs from the mean state of the real ocean, in particular with respect to the separation and penetration of western boundary currents. Thus, there is quite a discrepancy between the real ocean on one hand,

and eddy-permitting OGCMs and intermediate complexity models on the other hand, when studying the behavior of western boundary currents. The situation is much better with respect to truly eddy-resolving OGCMs, but their output has only recently become available (Chassignet et al., 2001; Hurlburt and Hogan, 2000; Smith et al., 2000). We will address this and other problems associated with the chosen approach again in chapter 7. Despite these problems, it will be demonstrated in chapters 3-5 that (features of) the observed bimodality and intermonthly variability of the Gulf Stream and the Kuroshio are more or less realistically simulated by an eddy-permitting OGCM and a SW model on the sphere. Therefore, the chosen approach will provide a framework to understand the observed bimodality and intermonthly variability of the Gulf Stream and the Kuroshio.

Chapter 2

Connection between multivariate time series analysis and bifurcation analysis

2.1 Introduction

As we have seen in the previous chapter, using a hierarchy of (equivalent) barotropic models, internal ocean dynamics can induce preference for some frequencies of variability. One of the questions we like to address in this chapter is, whether the oscillatory modes associated with these frequencies can still be found when stratification is included. Besides, we like to know which new frequencies are introduced by the inclusion of stratification.

Cox (1987) and Miller et al. (1987) studied the internal variability in baroclinic models by integrating the equations in time. Cox (1987) used a primitive equation, eddy-resolving numerical model to study the inherent timescales of variability in the subtropical gyre, assuming temporally constant surface forcing. He found three primary scales: mesoscale variability of approximately 50-day period, zonal barotropic bands of 1.1 year period and gyre scale undulations of 4 to 4.5 year period. The latter are identified as first mode baroclinic Rossby waves.

Miller et al. (1987) analyzed the internal variability in a two-layer, flat-bottom, steady-wind driven, eddy-resolving quasigeostrophic (QG) model. They found a distinct frequency separation of baroclinic (periods greater than about 100 days) and barotropic motion (periods less than about 100 days) in the region distant from the model jet. The eddy-generating, free-jet region, however, appeared to contain barotropic and baroclinic energy throughout the model frequency range. The large-scale barotropic flow revealed resonant basin modes driven by mesoscale activity of the turbulent, free-jet region.

Dijkstra and Katsman (1997) addressed the stability of the wind-driven ocean circulation within a two-layer QG model systematically using continuation techniques. They determined the steady state solutions and their linear stability using the Reynolds number as control parameter. Three Hopf bifurcations were found, which are important in the study of the origin

of a particular type of variability because they mark the transition to temporal behavior (Appendix B.1). Apart from the bifurcation analysis, transient flow computations were performed for different values of Re , to investigate the forcing of the second layer (Katsman et al., 1998). Time integrations at values of Re larger than 40 showed complicated temporal behavior and are analysed in this chapter using multivariate time series analysis techniques.

The goal of this study is to find the relevant spatiotemporal patterns which determine the internal variability within the Dijkstra and Katsman (1997)'s two-layer QG model of the wind-driven ocean circulation. To find these patterns, two analysis techniques will be used in order to make an intercomparison of their skills: Multichannel Singular Spectrum Analysis (M-SSA) (Plaut and Vautard, 1994) and Principal Oscillation Patterns (POPs) (Hasselmann, 1988; Von Storch et al., 1995). These techniques are usually employed to determine spatiotemporal patterns in datasets from observations or GCMs. As the dynamics of the two-layer QG model is relatively well-known, the spatiotemporal patterns identified by the two techniques can be compared with the patterns found by Dijkstra and Katsman (1997) at the Hopf bifurcations.

The structure of this chapter is as follows. The two-layer model, its basic bifurcation diagram and time-dependent behavior are presented in section 2.2. In Appendix A the background of the multivariate time series analysis techniques, M-SSA and the POP analysis, is given. The results of the multivariate time series analysis of the QG model, using M-SSA and the POP analysis, are shown in section 2.3, followed by a discussion in section 2.4.

2.2 Bifurcation diagram of the two-layer QG model

In this study output from the two-layer QG model of Katsman et al. (1998) is analyzed using multivariate time series analysis. Therefore, only the essentials of the model will be repeated here. The two-layer QG model, situated on a mid-latitude β -plane, consists of a square basin of horizontal dimension L and of constant depth D ; the two layers having densities ρ_1 and ρ_2 and mean layer thicknesses D_1 and D_2 ($D = D_1 + D_2$), respectively. The circulation at the surface is forced by a steady, symmetric zonal windstress $\tau_0 \tau^x(y)$, which induces a double-gyre flow. No interfacial or bottom friction is applied, so that dissipation occurs only by lateral friction. Slip conditions are prescribed at the northern and southern boundaries and no-slip conditions at the eastern and western boundaries.

The governing equations of the two-layer QG model (Pedlosky, 1987) are rewritten in dimensionless form using horizontal and vertical length scales L and D , a characteristic velocity scale U_{QG} , a timescale L/U_{QG} , and a scale for the windstress τ_0 , indicating the maximum amplitude of the windstress. The resulting potential vorticity equations for the two layers contain five parameters: the Reynolds number Re , the strength of the planetary vorticity gradient β , the windstress forcing strength α_τ , and the rotational Froude numbers F_1 and F_2 based on the first and second layer, respectively. Dijkstra and Katsman (1997) have used the Reynolds number $Re = \frac{U_{QG} L}{A_H}$ as the control parameter of the system, where A_H is the lateral friction coefficient. The values of the other parameters are displayed in their Table 1.

The basic bifurcation diagram for standard values of the parameters and for a 49×33 non-equidistant grid (Dijkstra and Katsman, 1997) is presented in Figure 2.1a (From Dijkstra

et al., 1999). In this diagram the value of the streamfunction at a particular gridpoint $\psi_{SW} = \psi_1(6, 4)$ is plotted against the control parameter, i.e. the Reynolds number in this case. For an extensive discussion of this diagram the reader is referred to Dijkstra and Katsman (1997).

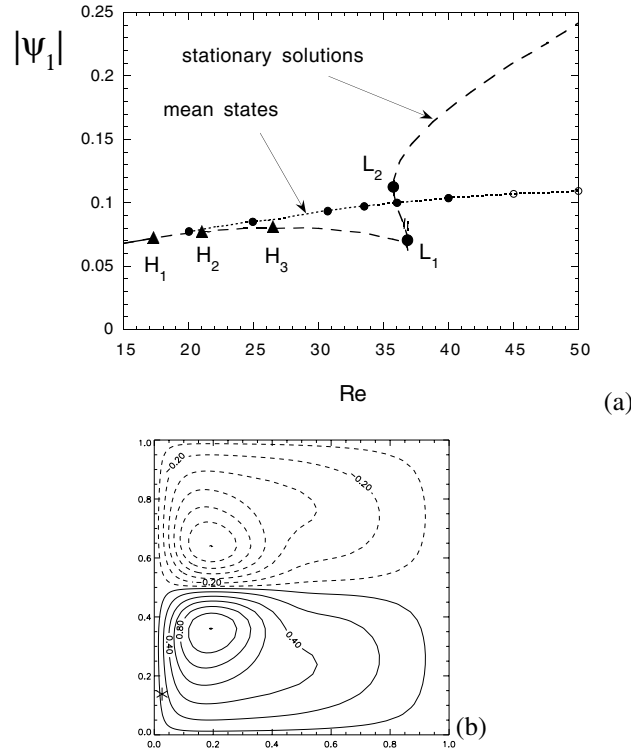


Figure 2.1: (a) Bifurcation diagram for the 2-layer QG model with Re as control parameter and for standard values of the other parameters (Dijkstra and Katsman, 1997, their Table 1). On the vertical axis, the value of $\psi_{SW} = \psi_1(6, 4)$ is plotted. Solid (dashed) lines represent stable (unstable) steady states. Marked are three Hopf bifurcations (H_1 to H_3) and two limit points (L_1 and L_2). The dotted line connects the mean states of time integrations (marked by circles) performed at several values of Re . From Dijkstra et al. (1999). (b) Contour plot of the upper layer streamfunction ψ_1 at the Hopf bifurcation H_1 in (a) (contour interval is 0.2). From Katsman (2001).

For small values of Re linearly stable symmetric double-gyre flow solutions exist. For smaller lateral friction, the basic state (Fig. 2.1b) is destabilized through an oscillatory mode at the Hopf bifurcation H_1 ($Re = 17.2$) in Figure 2.1a. Note that there is no flow in the lower layer ($\psi_2 = 0$) since it is unforced. The spatial pattern of the neutral mode is shown in Figs. 2.2a-b. It is "banana-shaped" (Dijkstra and Katsman, 1997) near the zonal jet. The perturbation moves eastward with the flow direction of the jet. The disturbance adds either a south- or northward component to the eastward flow in the jet, i.e. it causes the jet to meander, and it has an oscillation period of 4.3 months.

A second Hopf bifurcation (H_2 in Fig. 2.1a) occurs at $Re = 21.0$; the basic steady flow has not changed much compared to Figure 2.1b and is therefore not shown. The period of

this oscillation is 8.2 months, and the destabilizing perturbation is shown in Figs. 2.2c-d. The configuration of the disturbance represents local and temporary weakening and strengthening of the jet.

A third Hopf bifurcation (H_3 in Fig. 2.1a) occurs at $Re = 26.5$. The spatial pattern of this neutral mode (Figs. 2.2e-f) is also symmetric with respect to $y = 0.5$, like the neutral mode at H_1 . Moreover, the effect of H_3 appears to be the same as that of H_1 , namely meandering of the jet. However, the period of this oscillation is a bit longer, namely 6.0 months. All three instabilities have a dominant baroclinic nature (Fig. 2.2; Katsman, 2001).

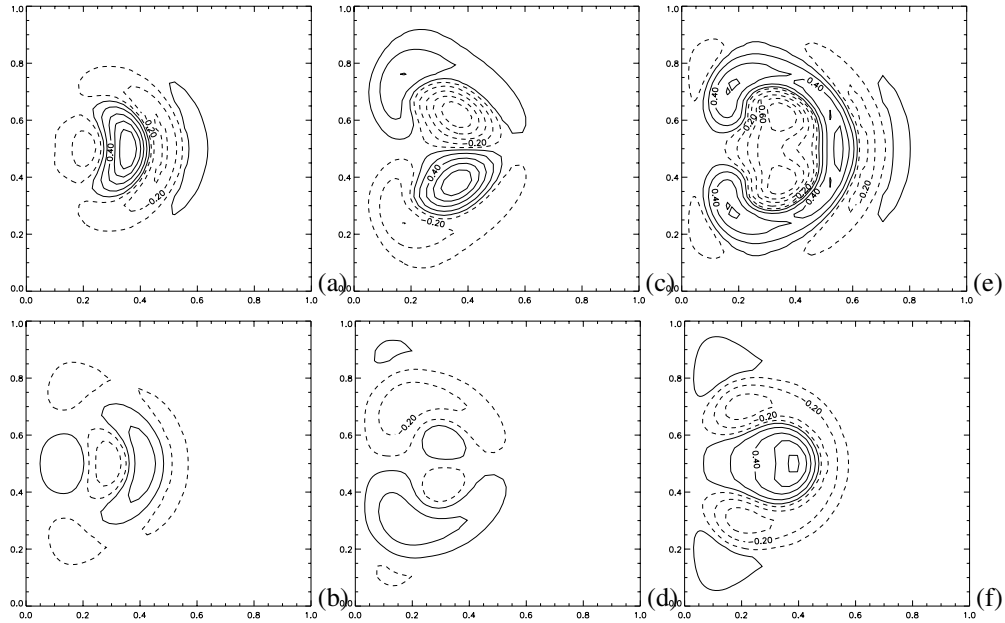


Figure 2.2: (a-b) Contour plot of the (a) upper and (b) lower layer streamfunction of the neutral oscillatory mode at the Hopf bifurcation H_1 in Figure 2.1a at one phase of the oscillation. Contours are with respect to the absolute maximum of the upper layer streamfunction. (c-d) As (a-b), but for the neutral oscillatory mode at the Hopf bifurcation H_2 in Figure 2.1a. (e-f) As (a-b), but for the neutral oscillatory mode at the Hopf bifurcation H_3 in Figure 2.1a. From Katsman (2001).

Apart from the bifurcation analysis, transient flow computations were performed for different values of Re , to investigate the contribution of the different modes of variability to the time-dependent behavior. The mean states of these time integrations are shown as circles in Fig. 2.1a and the periodic orbit coming from the first Hopf bifurcation is stable up to $Re \approx 40$. By comparing the mean state of this periodic orbit, which has a non-zero response in the lower layer, and the unstable steady circulation with a motionless lower layer, the forcing of the second layer was analysed in Katsman et al. (1998). Self-interactions of the most unstable mode turn out to be the main forcing for the mean flow in the lower layer and the rectification is dominated by self-interactions over a large range of friction values.

Time integrations at larger values of Re show more complicated temporal behavior and are analysed using M-SSA and POP analysis in the next section. More specifically, we com-

pare the results from the multivariate time series analysis of the QG model output with the patterns and timescales of the neutral oscillatory modes displayed in Figure 2.2.

2.3 Multivariate time series analysis of the two-layer QG model

First, the number of channels (i.e. 1617 grid points) has been reduced by means of principal component analysis (PCA), so that the number of spatial degrees of freedom has been reduced (see Appendix A for methods and terminology). The resulting leading principal components (PCs) constitute the channels (10 in this study) for the M-SSA and POP analyses; these 10 PCs explain more than 96% of the total variance for each case described below. Second, the M-SSA and POP analyses have been applied to this reduced number of channels. In all cases described below the sampling time is the same as the time step, i.e. 1 week, and the sample size is $N = 200$ (4 years).

A major problem when using M-SSA is the choice of the window length M . It can be shown that M-SSA does not resolve periods longer than the window length. In this study, a standard window length of $M = 60$ (14 months) is used, i.e. less than $1/3$ of the sample size, which is required to avoid statistical errors to dominate the last values of the autocovariance function (Vautard, 1995). For several Reynolds numbers, the window length was also set to 40 (10 months) to investigate whether the results obtained for $M = 60$ are robust. It turned out that this was indeed the case.

The mean streamfunction field at $Re = 40$ (not shown) shows an intensified jet compared to the basic state at $Re = 17.2$ (Fig. 2.1b). When going to larger Reynolds numbers, the recirculation cells are extending further to the east. In the Figures 2.3, 2.4, and 2.5 the dominant M-SSA modes, i.e. reconstructed components (RCs) 1-2, are depicted for $Re = 40$, $Re = 45$, and $Re = 57$, respectively. The pattern of the dominant POP at a certain Reynolds number strongly resembles the pattern of the dominant RC at the same Reynolds number and the oscillation periods, obtained from the POP and M-SSA analyses, are the same. Therefore the POPs are not shown. At $Re = 40$ (Fig. 2.3) the pattern of RC 1-2 can be linked to the neutral mode at H_1 (cf. Fig. 2.2a) and the oscillation period is 3 months, which is shorter than the oscillation period of the neutral mode at H_1 (4.3 months). This may be a result of the decreased lateral friction which causes the frequency of the oscillation to increase. The damping time of the corresponding (dominant) POP is 4 years, which means that this mode is stable in the statistical sense (Von Storch et al., 1995).

At $Re = 45$ (Fig. 2.4) the pattern of RC 1-2 can be linked to the neutral mode at H_2 (cf. Fig. 2.2c) and the period of this oscillation is 5 months, which is also shorter than the oscillation period of the neutral mode at H_2 (8.2 months). The corresponding POP is statistically stable as well: it has a damping time of 5 years.

The pattern of RC 1-2 at $Re = 57$ (Fig. 2.5) deserves special attention, because it was not detected by Dijkstra and Katsman (1997) in the bifurcation analysis of the 2-layer model. However, it was detected by them in the bifurcation analysis of the 1.5-layer model (Fig. 1.9a). The oscillation consists of a basin scale perturbation and the period of this oscillation is 2 months which is the same as the oscillation period of the neutral mode at the first Hopf bifurcation found by Dijkstra and Katsman (1997) in the 1.5-layer model (2.0 months). Again,

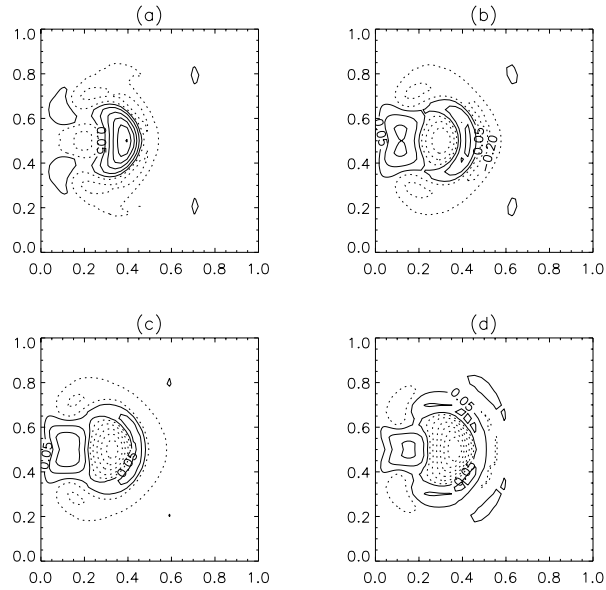


Figure 2.3: Reconstructed component (RC) pair 1-2 of the upper layer streamfunction at $Re = 40$ at several phases of the oscillation. (a) $t = 0$; (b) $t = \pi/4$; (c) $t = \pi/2$; (d) $t = 3\pi/4$. Contours are with respect to the absolute maximum of RC 1-2.

the corresponding POP is stable in the statistical sense which follows from the damping time of 4 years. This mode is called "basin mode" (Dijkstra and Katsman, 1997), because it is the frictional modification of the inviscid basin modes considered in Pedlosky (1987). This instability has a barotropic nature: the streamfunction time series in the upper and lower layers are in phase, the amplitudes are (nearly) equal and the patterns overlapping, at least in the eastern half of the basin (Fig. 2.5). Results from a singular value decomposition (SVD) of the covariance matrix (Prohaska, 1976; Bretherton et al., 1992) between the streamfunction fields from the upper and lower layer confirm the barotropic nature of this mode: the temporal correlation coefficient between the expansion coefficients of the two fields associated with this mode is 1.0.

In Figure 2.6 RC 7-8 is shown for $Re = 42.5$, which explains only 7% of the total variance at that Reynolds number. This pattern can be linked to the neutral mode at H_3 (cf. Fig. 2.2e), although it is not exactly symmetric with respect to $y = 0.5$. The period of this oscillation is 10 months, which is longer than the oscillation period of the neutral mode at H_3 (6.0 months). The corresponding POP is not that statistically stable: it has a damping time of 20 months which is only 2 times the oscillation period.

In Figure 2.7a a histogram is depicted, from which the amount of variance can be deduced that is explained by the various M-SSA modes as a function of the Reynolds number. At all events up to $Re = 42.5$ the pattern linked to the neutral mode at H_1 is dominant; at $Re = 45$ and $Re = 50$ the pattern linked to the neutral mode at H_2 is dominant; at all events from

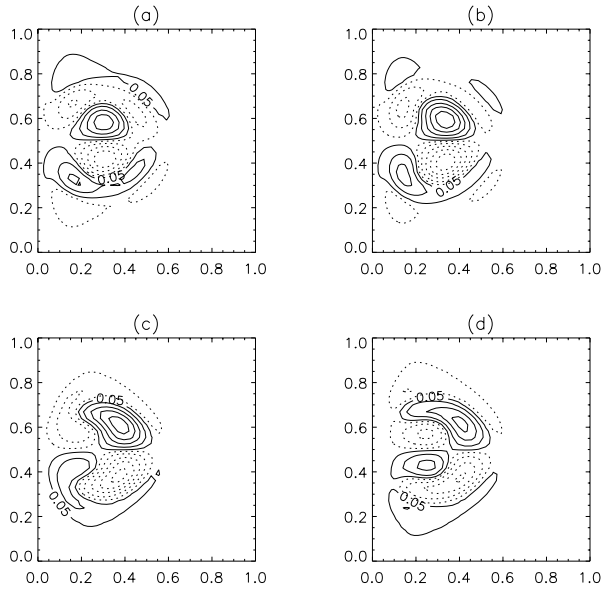


Figure 2.4: RC pair 1-2 of the upper layer streamfunction at $Re = 45$ at several phases of the oscillation. (a) $t = 0$; (b) $t = \pi/4$; (c) $t = \pi/2$; (d) $t = 3\pi/4$.

$Re = 56.5$ the basin mode (BM) is dominant. Although the patterns of the dominant modes (Figs. 2.3, 2.4 and 2.5) are more or less modified according to the amount of explained variance, the structures remain easily recognizable. In Figure 2.7b a histogram is depicted, from which the percentage of the total variance can be deduced that is explained by the various POPs as a function of the Reynolds number. Although the quantitative picture differs somewhat from Figure 2.7a, the qualitative picture is the same for both figures. The total amount of explained variance, however, is somewhat lower for the POPs than for the M-SSA modes, particularly at $Re = 50$.

2.4 Discussion

The internal variability in Dijkstra and Katsman (1997)'s two-layer QG model of the wind-driven ocean circulation is systematically studied and the stability of periodic orbits is determined. The periodic orbit, coming from the first Hopf bifurcation (at $Re = 17.2$), remains stable until $Re = 40.5$. Around this value of Re a bifurcation of the (stable) periodic orbit, i.e. a Naimark-Sacker (or torus) bifurcation, occurs (Van der Vaart, personal communication). Between $Re = 40.5$ and $Re = 56.5$, the time-dependent behavior of the QG model is dominated by at most four different modes, the amount of explained variance of each depending on the value of the Reynolds number (Fig. 2.7). Three M-SSA modes (Figs. 2.3, 2.4 and 2.6) can be linked to the neutral modes at the Hopf bifurcations H_1 , H_2 , and H_3 (Fig.

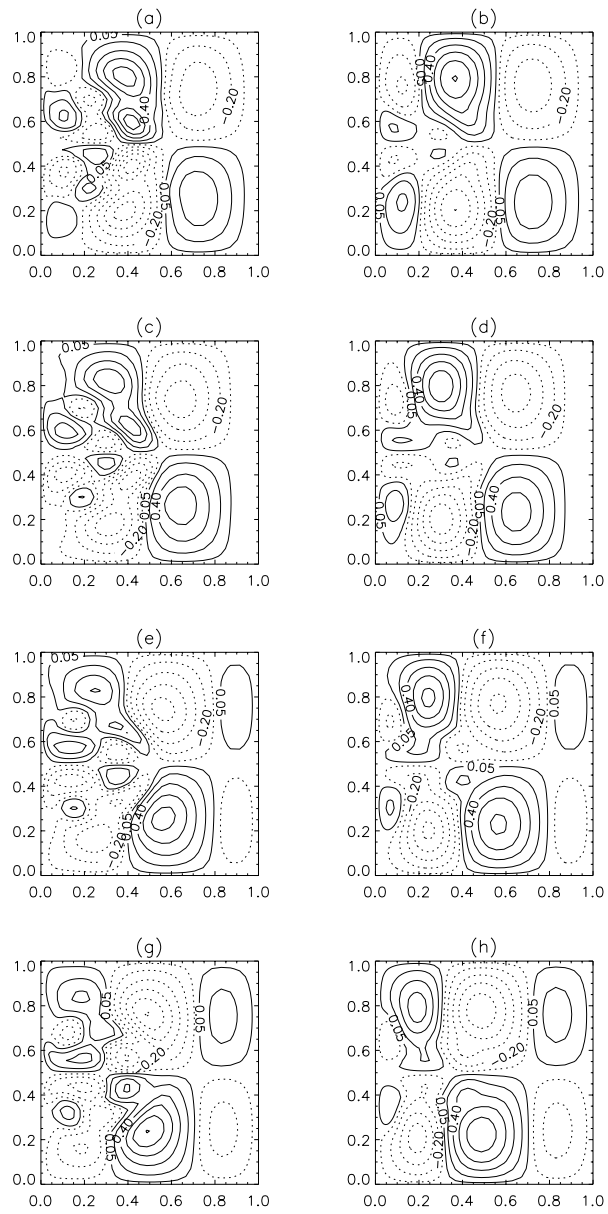


Figure 2.5: RC pair 1-2 of the upper (a,c,e,g) and lower (b,d,f,h) layer streamfunction at $Re = 57$ at several phases of the oscillation. (a-b) $t = 0$; (c-d) $t = \pi/4$; (e-f) $t = \pi/2$; (g-h) $t = 3\pi/4$.

2.2) in the bifurcation diagram of the two-layer model (Fig. 2.1a; Dijkstra et al., 1999), with

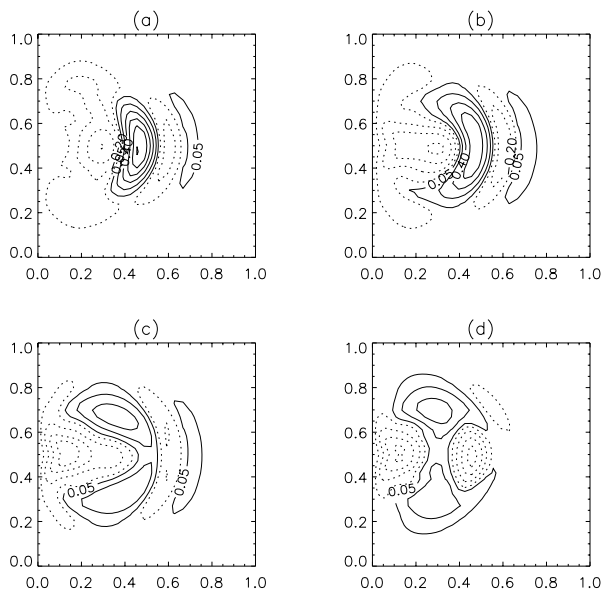


Figure 2.6: RC pair 7-8 of the upper layer streamfunction at $Re = 42.5$ at several phases of the oscillation. (a) $t = 0$; (b) $t = \pi/4$; (c) $t = \pi/2$; (d) $t = 3\pi/4$.

timescales of 3, 5, and 10 months, respectively. The other M-SSA mode (Fig. 2.5), called the basin mode, can be linked to the neutral mode at the Hopf bifurcation H_1 (Fig. 1.9a) in the bifurcation diagram of the 1.5-layer model (Fig. 1.7), with a timescale of 2 months. This demonstrates that for a full explanation of the origin of temporal variability, a hierarchy of models is useful (Dijkstra et al., 1999).

From $Re = 57$ to Re somewhere between 65 and 70, the periodic orbit associated with the basin mode is stable. Physically speaking, the basin mode may be resonantly excited by mesoscale activity of the free-jet region (Miller et al., 1987). Thus, the limit cycles remain important during the time evolution of the system far into the unstable regime (Dijkstra and Katsman, 1997). The unstable steady states at larger Reynolds numbers, however, do not appear to be important.

In summary, only a few modes seem to be involved in causing the complex time-dependent behavior, even in the irregular regime. This same point was made in Berloff and Meacham (1998) from the different trajectories for the single gyre baroclinic model, who in addition claim that the route to chaos is the classical three frequency route. A very large part of the variability in the time integrations can be attributed to the modes that go unstable at H_1 , H_2 and H_3 , and to the barotropic basin mode (Fig. 2.7).

On the basis of the results of the M-SSA and POP analyses in this study, it cannot be concluded which method should be preferred when dealing with vector time series. In the literature, however, a hint is given. The POP analysis uses a first-order autoregressive model, whereas M-SSA uses a model of order $M - 1$. On the basis of this, Plaut and Vautard (1994)

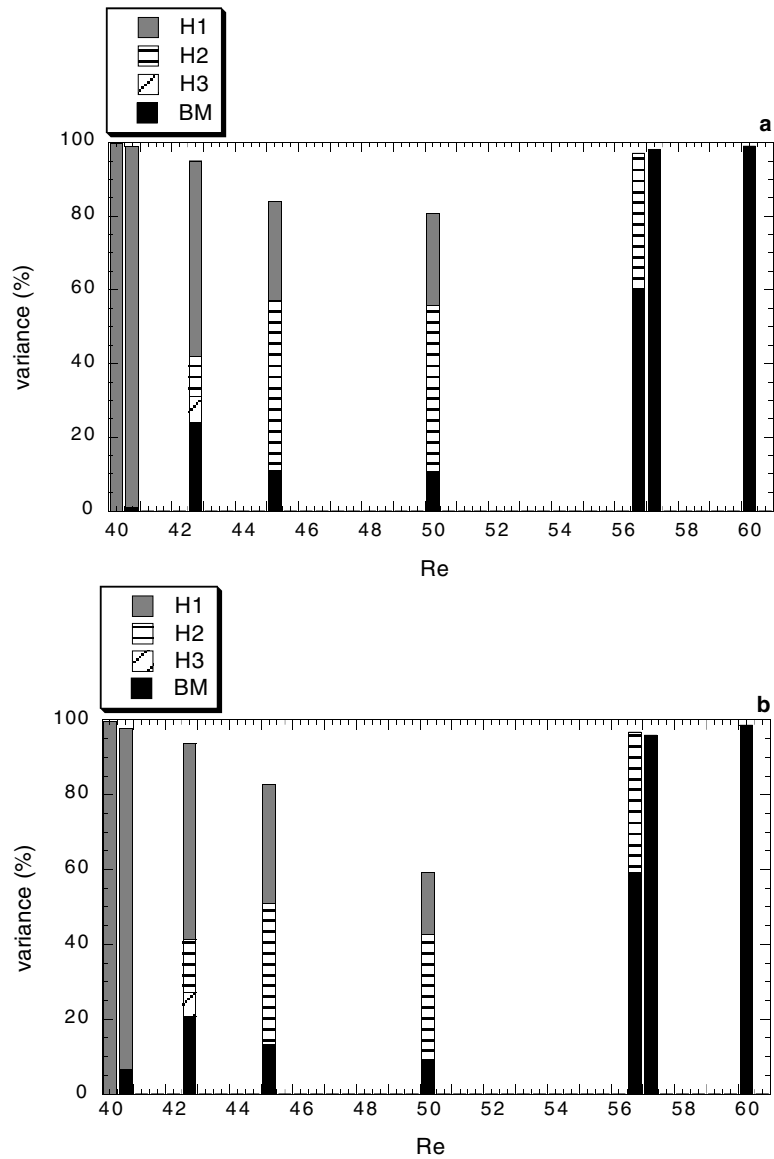


Figure 2.7: Histograms of the percentage of the total variance explained by different modes in the time integrations of the two-layer QG model using (a) M-SSA and (b) POP analysis. Here, H_1 , H_2 and H_3 refer to the patterns of neutral modes (Fig. 2.2) at the Hopf bifurcations in Fig. 2.1a, and BM to the barotropic basin mode (Fig. 1.9a).

hypothesize that the POP analysis should act on a less wide range of timescales. Therefore, M-SSA is used as the principal multivariate time series analysis technique in the rest of this

thesis.

As the results from the multivariate time series analysis of the two-layer QG model could be successfully linked to the results from the bifurcation analysis of the same model, this gives some hope with respect to the dynamical significance of the statistical modes that come out of the multivariate time series analysis of observations. However, the number of degrees of freedom is much larger in real datasets and there is also much noise in the system. We will investigate the connection between multivariate time series analysis and bifurcation analysis again for the barotropic shallow-water model with and without noise (see chapter 6). But before that, we are going to combine data analysis and dynamical systems analysis to study the bimodality and internal variability of the Kuroshio and the Gulf Stream, which is the main subject of this thesis.

Chapter 3

Bimodal behavior of the Kuroshio and the Gulf Stream*

3.1 Introduction

The Kuroshio in the North Pacific Ocean and the Gulf Stream in the North Atlantic Ocean are the major northern hemispheric western boundary currents which transport an enormous amount of volume, heat and salt polewards. The mean position of these currents is therefore important for the global climate system. Although the North Pacific basin has larger dimensions than the North Atlantic basin, the mean windstress forcing is very similar and a close dynamical correspondence between both western boundary currents is expected.

From observations, it is found that the Kuroshio path exhibits bimodal behavior to the south of Japan with transitions occurring between a small and a large meander state (Fig. 1.4; adapted from Taft, 1972). Both states can persist over a period ranging from a few years to a decade and transitions between them occur within a couple of months (Kawabe, 1986). A 42-year long time series of the mean distance of the Kuroshio axis from the Japanese coast (Qiu and Miao, 2000) shows that large meander states occurred, for example, during 1959-1962, 1975-1979 and 1982-1985.

Satellite images of sea surface temperature (SST) of the North Atlantic have revealed that the Gulf Stream near South Carolina can be in a weakly deflected or a strongly deflected state (Fig. 1.3; from Bane and Dewar, 1988). Bane and Dewar (1988) have presented observations which suggest that the seaward deflection of the Gulf Stream has a bimodal character and that the transitions between both states occur on intermonthly timescales. Results from other studies of the Gulf Stream path using in situ measurements and very high resolution infrared satellite data also show indications of bimodal behavior. In Fig. 4 of Olson et al. (1983), a histogram of the cross-stream frontal position (over the period 1976-1980) shows a bimodal distribution in the area just before separation (at about $77^{\circ} W$). Similarly, in Fig. 8c of Auer (1987) using AVHRR data over the period 1980-1985, a probability distribution of the

*This chapter is based on Schmeits, M. J., and H. A. Dijkstra, 2001: Bimodal behavior of the Kuroshio and the Gulf Stream. *J. Phys. Oceanogr.*, accepted.

Gulf Stream Landward Surface Edge shows an indication for bimodality in the area just after separation (at $71^\circ W$). The two peaks in the histograms of Olson et al. (1983) and Auer (1987) are separated from each other by about 50 km in cross-stream direction and 0.5° in latitude, respectively.

The question arising from these observations is clear: what are the physical processes responsible for this bimodal behavior? A central element in the classical explanation of the bimodality of the Kuroshio is the existence of multiple equilibria (Charney and Flierl, 1981; Masuda, 1982). In most of the previous modeling studies (e.g. Chao, 1984), regional models were used with in/outflow boundary conditions and multiple paths of the Kuroshio were found. For instance, using a barotropic quasigeostrophic model with geometry and bottom topographic features incorporated, Chao (1984) found multiple quasi-steady (small and large meander) paths of the Kuroshio if the volume transport exceeds a certain critical value. For values smaller than this critical transport, about 30 Sv in his model, only a small meander state is found. When the continental geometry representing the Kyushu wedge is removed, the large meander state can no longer be found, indicating that the geometry is crucial for the existence of the bimodality. For the Gulf Stream, Bane and Dewar (1988), following Legeckis (1976), have attributed the deflection to the flow of the Stream over the "Charleston bump", a topographic feature located on the upper continental slope at about $31^\circ N$ offshore of Charleston, South Carolina.

Although not really challenging the multiple equilibria viewpoint of the bimodality of the Kuroshio, Qiu and Miao (2000) have pointed out that the path flow variations are not necessarily controlled by the external inflow changes. In fact, they have shown, using the relatively long (from 1960) in-situ observational time series, that there is no close correspondence between upstream volume transport and transitions in the mean path of the Kuroshio. Moreover, as Qiu and Miao (2000) have pointed out, regional models with in/outflow boundary conditions (e.g. Chao, 1984) may strongly influence the dynamics of the flow and not be able to realistically capture the Kuroshio's recirculation gyre, which is an inseparable part of the Kuroshio current system.

To study Kuroshio path transitions, Qiu and Miao (2000) have therefore chosen to use a 2-layer primitive-equation model of the North Pacific Ocean with a horizontal resolution of $\frac{1}{6}^\circ$ in a realistic configuration driven by monthly climatological windstress data (Hellerman and Rosenstein, 1983). Variations between a straight path and a meander path of the Kuroshio are found on interannual timescales, when the wind forcing is strong enough. They propose that the observed alternations of the Kuroshio's two states are due to a self-sustained internal oscillation involving the evolution of the southern recirculation gyre and the stability of the Kuroshio current system, rather than being controlled by the temporal changes in the upstream Kuroshio transport. In one phase of the oscillation, low potential vorticity water of southern origin is advected with the inertially controlled Kuroshio path, which strengthens the southern recirculation gyre. This leads initially to the straight path, but as the intensification of the recirculation gyre progresses, it eventually leads to the development of a meander path due to baroclinic instability. As the meander grows in amplitude, it eventually breaks off to form an isolated eddy, thereby mixing high potential vorticity water of coastal origin into the recirculation gyre which weakens the latter. The Kuroshio will return to the straight path state after re-strengthening of the recirculation gyre due to the gradual accumulation of the low potential vorticity anomalies.

Hurlburt et al. (1996) have also used a primitive-equation model of the North Pacific in a realistic configuration, driven by the Hellerman and Rosenstein (1983) monthly windstress climatology, but with 6 vertical layers and a horizontal resolution of $\frac{1}{8}^\circ$. Various transitions between a straight Kuroshio path and a meander Kuroshio path have been found, with each state lasting for several years; the model results show persistent bistable states with mesoscale variability but little variation in 1-year means. The major differences between the Hurlburt et al. (1996) results (their Figs. 6e and g) and those of Qiu and Miao (2000) (their Fig. 8) are that in the former results (i) the straight path is more zonally oriented, contrary to observations (cf. Fig. 1.4), and (ii) the zonal penetration scale of the Kuroshio Extension is much longer, probably as a result of the higher resolution. From the set of model runs in Hurlburt et al. (1996), they conclude that the meander path depends on the occurrence of baroclinic instability west of the Izu Ridge and that otherwise a straight path occurs. Increases in wind forcing on interannual timescales give rise to a predominant meander path, while decreases yield a predominant straight path.

Indications of bimodal behavior are also found in very high resolution simulations of the Gulf Stream (Smith et al., 2000), although it has not been recognized as such. For instance, during the spinup phase of a simulation using the Los Alamos Parallel Ocean Program model (with a horizontal resolution of $\frac{1}{10}^\circ$ and 40 vertical levels), the simulated Gulf Stream south of Cape Hatteras 'occasionally meandered too far from the coastline'. Because it was suggested that this might be caused by the inadequate resolution of the Munk layer, the viscosity and diffusivity were both increased by a factor of 3 to reduce this "problem" (Smith et al., 2000).

Much work has been done to understand the separation of the Gulf Stream near Cape Hatteras (Dengg et al., 1996). In a high resolution Modular Ocean Model simulation with $\frac{1}{3}^\circ$ horizontal resolution (Beckmann et al., 1994; Bryan et al., 1995), the time mean state shows a large anti-cyclonic gyre north of Cape Hatteras giving an actual separation north of the observed position with non-desirable consequences for the simulated heat transport. However, the Los Alamos Parallel Ocean Program model shows realistic separation near Cape Hatteras (Smith et al., 2000, their Fig. 6). The mean position of the Gulf Stream, as defined by the 12°C isotherm at 400 m depth averaged over a four year period, shows only a slight southward offset of the path after separation. Also the Gulf Stream path statistics are reasonable, with the magnitude of the simulated meander envelope being similar to that of the observed envelope. Although many parameter studies which have been performed with idealized models cannot easily be done with the high resolution models, it is clear that when the resolution increases in the models and friction coefficients decrease, the inertial character of the flow increases and separation becomes more realistic (McWilliams, 1996; Hurlburt and Hogan, 2000).

In section 3.2 below, the behavior of the northern hemispheric western boundary currents is investigated in output from the Parallel Ocean Climate Model (POCM). Bimodality is found in both the Kuroshio and the Gulf Stream region although of different intensity and frequency. To find a theoretical framework to understand the bimodality in this model, we continue a line of studies addressing the stability and variability of western boundary currents within a hierarchy of models using techniques of dynamical systems theory (Speich et al., 1995; Dijkstra and Katsman, 1997; Dijkstra and Molemaker, 1999; Dijkstra et al., 1999; Schmeits and Dijkstra, 2000, section 1.3). Over the last decade, theoretical studies of behavior of nonlinear western boundary currents have indicated that multiple steady states

of the wind-driven gyres appear in idealized closed rectangular basins through spontaneous symmetry breaking (Cessi and Ierley, 1995; Jiang et al., 1995; Dijkstra and Katsman, 1997). In (equivalent) barotropic models, asymmetric states are found under symmetric (with respect to the mid-basin axis) forcing conditions. These multiple steady states persist when continental geometry and realistic windstress forcing are considered (Dijkstra and Molemaker, 1999). Given this robustness and the dynamical correspondence of Kuroshio and Gulf Stream, it is expected that in closed basin models for the North Pacific and North Atlantic, these multiple equilibria are present. Indeed, in section 3.4 below it is shown that qualitatively the bifurcation diagrams for both cases are the same within a barotropic shallow-water (SW) model (section 3.3), although the associated flow patterns and stability characteristics differ markedly. Moreover, the multiple paths have resemblance to those found in observations and in POCM.

Next, the possibility of transitions between the steady states through atmospheric noise is investigated. Sura et al. (2001) have used a reduced-gravity double-gyre ocean model for a rectangular basin to study the influence of an additive stochastic windstress component on the behavior of the wind-driven circulation. When forced with a spatially inhomogeneous stochastic forcing, in order to mimic the observed concentration of atmospheric eddy activity along the storm track, the model shows bimodal behavior. In one regime a quasi-antisymmetric flow pattern is found, while the other regime shows a non-symmetric flow pattern. Although no stationary solutions have explicitly been calculated in their study, Sura et al. (2001) have suggested that the non-symmetric regime corresponds to one member of a known non-symmetric pair of stationary solutions. This is confirmed by comparing their snapshots of the non-symmetric regime to the "jet up" stationary solution of Speich et al. (1995) (see also Fig. 1.6a), who have used a very similar model. Sura et al. (2001) have not found signatures of the symmetry related solution, that is the "jet down" stationary solution of Speich et al. (1995) (see also Fig. 1.6b). Their study has indicated that the bimodality does not appear without stochastic forcing nor with spatially homogeneous stochastic forcing. They have therefore concluded that the regime transitions are induced by the inhomogeneity of the white noise variance. In section 3.5, we will investigate the effect of an additive stochastic wind stress component on the behavior of the North Atlantic and North Pacific wind-driven circulation in a more realistic model context than that of Sura et al. (2001).

3.2 Northern hemispheric western boundary currents in POCM

The basic POCM formulation has been described by Semtner and Chervin (1992) and Stammer et al. (1996). The POCM output analysed is from run 4C having an average horizontal resolution of $\frac{1}{4}^\circ$ and 20 nonequidistant levels in the vertical direction. The model contains bottom topography, extrapolated from a bathymetric dataset. The global simulation was performed over the period 1979-98 and the ocean was forced by either ECMWF reanalysis (1979-93) or ECMWF operational (1994-98) fields of heat fluxes, freshwater fluxes, and windstress. These fields are updated every 3 days and interpolated to the time step. The annual river outflow was also included in the freshwater flux. Diffusion is handled using bi-harmonic closure for both momentum and tracers (Stammer et al., 1996). For more details

about this simulation the reader is referred to <http://vislab-www.nps.navy.mil/~rftt>. We have used monthly mean sea surface temperature (SST), sea surface height (SSH), and temperature fields at three depth levels, namely 160 m (T160), 310 m (T310), and 610 m (T610), in the Gulf Stream region ($23^\circ - 48^\circ N, 90^\circ - 30^\circ W$) and in the Kuroshio region ($25^\circ - 50^\circ N, 120^\circ - 180^\circ E$). SSH is a prognostic variable in POCM because of the incorporation of a free surface formulation.

3.2.1 Bimodality of the Kuroshio

In Fig. 3.1a, the latitudinal position of the maximum zonal geostrophic velocity at $136^\circ E$ is plotted over the period 1979-1998, and several transitions between two states occur on interannual timescales. In Figs. 3.1b and c, SSH deviations are superimposed on SST for the two states. One state, called Kuroshio meander state K_b^P (Fig. 3.1b), resembles the observed small meander state (Fig. 1.4). It is characterized by a northerly position of the maximum zonal geostrophic velocity at a latitude of about $33^\circ N$ (Fig. 3.1a), accompanied by an anti-cyclonic recirculation cell to the south. The other state, denoted as Kuroshio meander state K_c^P (Fig. 3.1c), resembles the observed large meander state (Fig. 1.4). It is characterized by a southerly position of the maximum zonal geostrophic velocity at a latitude of about $31.5^\circ N$ (Fig. 3.1a), accompanied by a cyclonic recirculation cell to the north. In both cases the main separation latitude of the Kuroshio is too far north (at about $40^\circ N$), as is also a problem in other high resolution models (e.g. Maltrud et al., 1998). By comparing the patterns of both states to the observed ones (cf. Fig. 1.4), the main differences are that the simulated small meander of K_b^P has a larger amplitude than the observed one, and that the simulated large meander of K_c^P has a smaller zonal extension than the observed one. Shaded contour plots of SST (Figs. 3.1b and c) indicate that heat is strongly advected with the mean current. The Kuroshio advects more heat northward in the case of small meander state K_b^P (Fig. 3.1b) than in the case of large meander state K_c^P (Fig. 3.1c).

The simulated Kuroshio has a larger eastward geostrophic transport when it is in its small meander state (K_b^P) than when it is in its large meander state (K_c^P), at least at $136^\circ E$ (Fig. 3.1a). Observations point at geostrophic transports of equal magnitude for both states at $137^\circ E$ (Qiu and Joyce, 1992). Finally, Fig. 3.1a suggests that the timing of the transitions from the large (K_c^P) to the small (K_b^P) meander state is related to the occurrence of strong El Niño events (beginning of 1983 and 1998). In other words, anomalous conditions during a strong El Niño (for instance in the pattern or amplitude of the windstress field) may induce transitions from the large to the small meander state. Note, however, that the transitions between the two states occur at different times in POCM than those in reality (Kawabe, 1995).

In Fig. 3.2 a sequence of POCM temperature fields at depth during 1998 shows the evolution of the Kuroshio from the large (K_c^P) to the small (K_b^P) meander state and back (see Fig. 3.1a). The upper left panel shows the Kuroshio in its large meander state. The meander grows in amplitude in the subsequent months (upper right panel) and it eventually breaks off to form an isolated eddy (situated at about ($133^\circ E, 28^\circ N$) in middle left panel), which drifts westward. After the detachment of the eddy, the Kuroshio path turns to the small meander state for a few months (middle panels). However, finally a new meander starts to develop at the end of the year (lower panels). Similar detachments of eddies from Kuroshio meanders

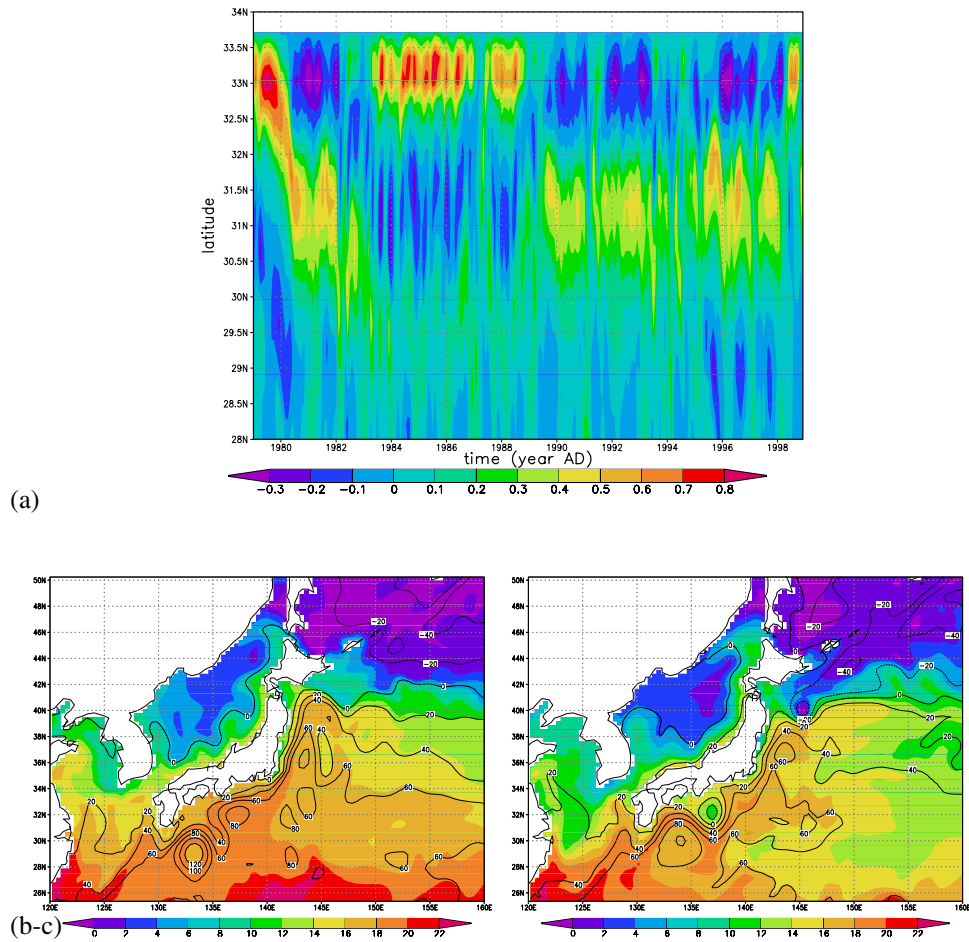


Figure 3.1: (a) Contour plot of zonal geostrophic velocity (m s^{-1}), calculated from meridional SSH gradients in POCM, at 136°E as a function of latitude for the period 1979-1998. (b-c) Contour plot of monthly mean SSH deviations (cm), superimposed on a shaded contour plot of monthly mean SST ($^{\circ}\text{C}$) for (b) January 1988, representing the small meander state K_b^P of the Kuroshio in POCM and (c) January 1996, representing the large meander state K_c^P of the Kuroshio in POCM (cf. Fig. 1.4).

have been detected in another primitive-equation model and in in-situ observations (Qiu and Miao, 2000, their Figs. 9 and 10). Moreover, Fig. 3.2 indicates that the signatures of the different meander paths are also found in the deeper ocean which leads us to the hypothesis that the transition between both meander states is a barotropically controlled phenomenon.

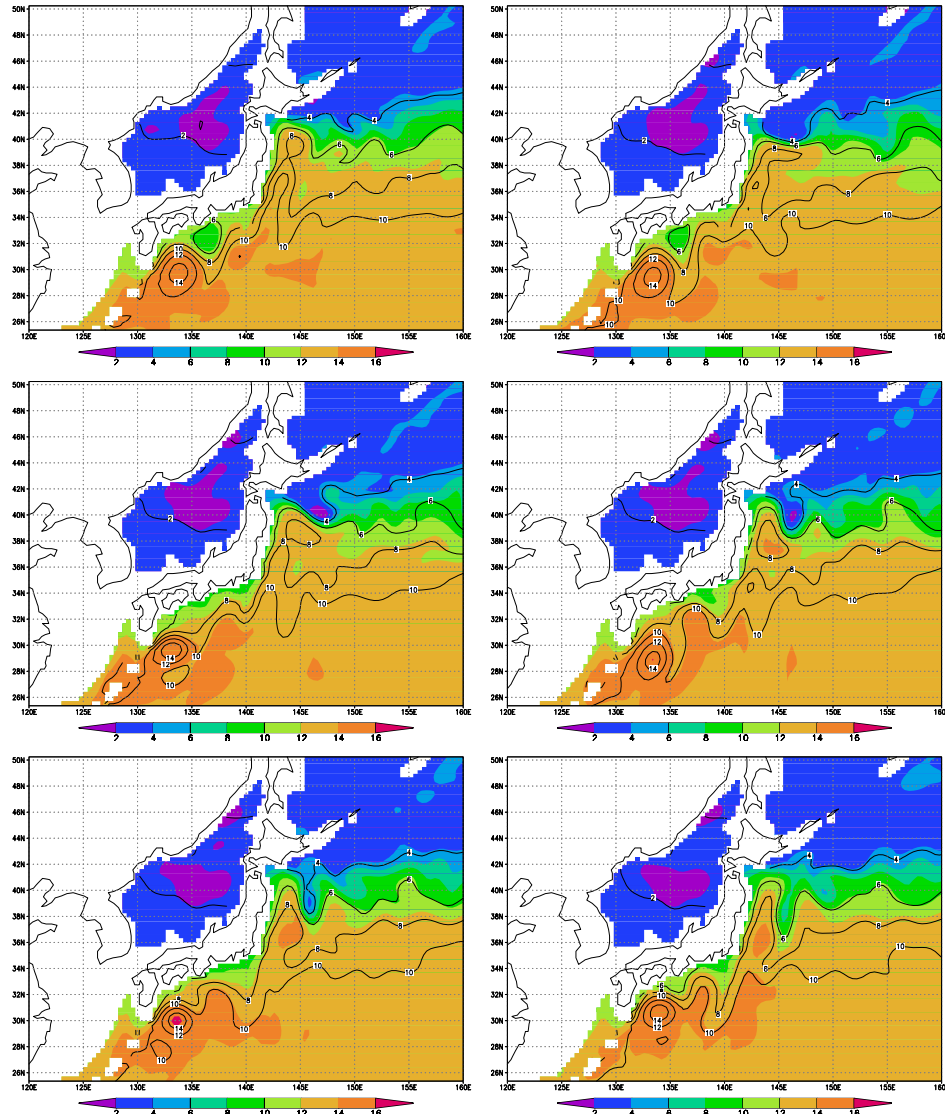


Figure 3.2: Sequence of contour plots of monthly mean T_{610} ($^{\circ}\text{C}$), superimposed on shaded contour plots of monthly mean T_{310} ($^{\circ}\text{C}$) from POCM, showing the evolution of the simulated Kuroshio from the large (K_C^P) to the small (K_b^P) meander state and back during 1998 (see Fig. 3.1a). The patterns are shown for January and March (upper panels), May and July (middle panels), and September and November (lower panels).

3.2.2 Bimodality of the Gulf Stream

In Fig. 3.3a, the latitudinal position of the maximum zonal geostrophic velocity at 75°W is plotted over the period 1979–1997. During the first year, the maximum zonal geostrophic

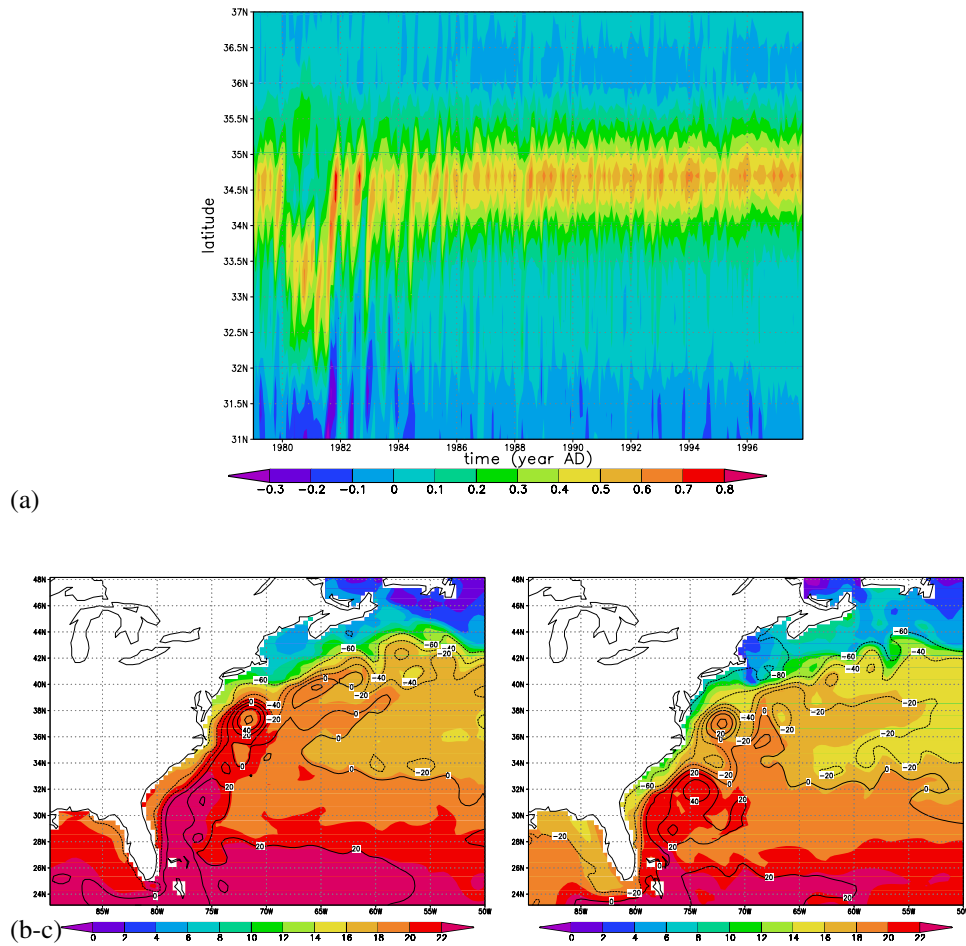
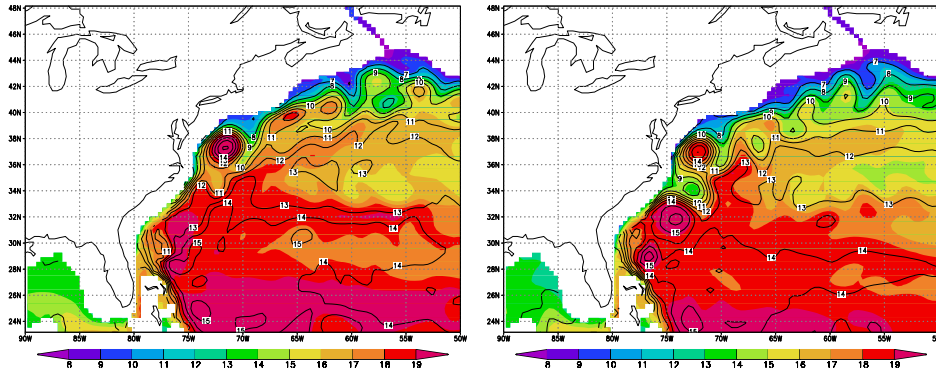


Figure 3.3: (a) Contour plot of zonal geostrophic velocity (m s^{-1}), calculated from meridional SSH gradients in POCM, at 75°W as a function of latitude for the period 1979-1997. (b-c) Contour plot of monthly mean SSH deviations (cm), superimposed on a shaded contour plot of monthly mean SST ($^{\circ}\text{C}$) for (b) January 1979, representing Gulf Stream state G_b^P in POCM and (c) January 1981, representing Gulf Stream state G_c^P in POCM (cf. Fig. 1.3). (d-e) Contour plot of monthly mean T610 ($^{\circ}\text{C}$), superimposed on a shaded contour plot of monthly mean T310 ($^{\circ}\text{C}$) for (d) January 1979 and (e) January 1981.

velocity is at a latitude of about 34.5°N and a contour plot of SSH anomalies is shown for January 1979 in Fig. 3.3b. Like the Kuroshio, the Gulf Stream also separates too far north compared to reality. It is characterized by a weak southern recirculation cell and a strong anti-cyclonic cell near Cape Hatteras, which is not observed in the North Atlantic Ocean. A similar mean state is also found in other high resolution models (Beckmann et al., 1994; Bryan et al.,



(d-e)

Figure 3.3 (continued)

1995; Maltrud et al., 1998). This pattern is quite similar to the observed Gulf Stream in its weakly deflected configuration (cf. Fig. 1.3), as far as the flow between the Florida Straits and Cape Hatteras is concerned, and we will refer to it as Gulf Stream state G_b^P . After a year, a significant shift southward occurs in the latitudinal position of the maximum zonal geostrophic velocity (Fig. 3.3a). The SSH anomalies for January 1981 (Fig. 3.3c) display a Gulf Stream which actually seems to separate twice. First, it separates too far south compared to reality, and later on it separates too far north (at about the same latitude as in Fig. 3.3b). It is characterized by a strong southern and a weak northern recirculation cell, centered at about ($74^\circ W, 32^\circ N$) and ($73^\circ W, 34^\circ N$), respectively, and again the strong unrealistic anti-cyclonic cell near Cape Hatteras. There are some differences between this pattern and the observed Gulf Stream in its strongly deflected configuration (cf. Fig. 1.3) in that the simulated path deflects farther to the north and that the amplitude of the associated meander is much larger than the observed one. We will refer to the simulated path of Fig. 3.3c as Gulf Stream state G_c^P . The southerly position of the maximum zonal geostrophic velocity is maintained for about two years and then the earlier position is retained (Fig. 3.3a).

Also in the Gulf Stream region (Figs. 3.3b and c), heat is strongly advected with the mean flow. The Gulf Stream advects more heat northward in the case of path G_b^P (Fig. 3.3b) than in the case of path G_c^P (Fig. 3.3c). At $75^\circ W$ the maximum temperature gradient, i.e. the cold wall, of Gulf Stream state G_b^P is situated at about $35^\circ N$ (Fig. 3.3b), and the cold wall of Gulf Stream state G_c^P has a more southerly position at about $34^\circ N$ (Fig. 3.3c), in correspondence with Fig. 3.3a. Analysis of the temperature fields at depth in POCM (Figs. 3.3d and e) indicates that the signatures of the different mean paths are also found in the deeper ocean which leads us to the hypothesis that the transition between both patterns is a barotropically controlled phenomenon, as was also hypothesized for the Kuroshio.

To summarize, in the POCM results indications of bimodal behavior are found for both Kuroshio and Gulf Stream. The bimodality of the Kuroshio occurs on interannual timescales and switches in the latitudinal position of the maximum geostrophic velocity are about 2° . For the Gulf Stream region, only one of these transitions is found and the lateral excursion of the maximum geostrophic velocity is smaller. In the next sections, we are going to explore

whether multiple steady states of the Kuroshio and the Gulf Stream are dynamically possible. To test the hypothesis that the transitions are barotropically controlled, a barotropic SW model is used.

3.3 The barotropic shallow-water model

In this section the barotropic shallow-water model is described.

3.3.1 Formulation

Consider a flat-bottomed ocean basin with a realistic horizontal domain, \mathcal{V} , and bounded by a closed contour Γ . The density of the ocean is constant and the flow is driven by a windstress $\tau(\phi, \theta) = \tau_0(\tau^\phi, \tau^\theta)$, where τ_0 is the amplitude and (τ^ϕ, τ^θ) provides the spatial pattern. Lateral friction, with lateral friction coefficient A_H , is the dissipative mechanism in the model. In the usual notation, the velocities in eastward and northward directions are indicated by u and v , respectively and h is the thickness of the water column (with equilibrium value D), and changes due to changes in the sea surface height. The governing shallow-water equations are non-dimensionalized using scales $r_0, D, U, r_0/U$ and τ_0 for length, layer depth, velocity, time, and windstress, respectively, where r_0 is the radius of the earth, and become

$$\begin{aligned} & \epsilon \left(\frac{\partial u}{\partial t} + \frac{u}{\cos \theta} \frac{\partial u}{\partial \phi} + v \frac{\partial u}{\partial \theta} - uv \tan \theta \right) - \\ -v \sin \theta = & -\frac{\epsilon F}{\cos \theta} \frac{\partial h}{\partial \phi} + E \left(\nabla^2 u - \frac{u}{\cos^2 \theta} - \frac{2 \sin \theta}{\cos^2 \theta} \frac{\partial v}{\partial \phi} \right) + \alpha \frac{\tau^\phi}{h} \end{aligned} \quad (3.1a)$$

$$\begin{aligned} & \epsilon \left(\frac{\partial v}{\partial t} + \frac{u}{\cos \theta} \frac{\partial v}{\partial \phi} + v \frac{\partial v}{\partial \theta} + u^2 \tan \theta \right) + \\ +u \sin \theta = & -\epsilon F \frac{\partial h}{\partial \theta} + E \left(\nabla^2 v - \frac{v}{\cos^2 \theta} + \frac{2 \sin \theta}{\cos^2 \theta} \frac{\partial u}{\partial \phi} \right) + \alpha \frac{\tau^\theta}{h} \end{aligned} \quad (3.1b)$$

$$\frac{\partial h}{\partial t} + \frac{1}{\cos \theta} \left(\frac{\partial(hu)}{\partial \phi} + \frac{\partial(hv \cos \theta)}{\partial \theta} \right) = 0. \quad (3.1c)$$

On the boundary Γ of the domain no-slip conditions are prescribed; that is,

$$(\phi, \theta) \in \Gamma : \quad u = v = 0. \quad (3.2)$$

The parameters in these equations are the Rossby number ϵ , the Froude number F , the Ekman number E , and the windstress coefficient α . Expressions for these parameters are

$$\epsilon = \frac{U}{2\Omega r_0}; \quad F = \frac{gD}{U^2}; \quad E = \frac{A_H}{2\Omega r_0^2}; \quad \alpha = \frac{\tau_0}{2\Omega \rho D U}, \quad (3.3)$$

where Ω is the angular velocity of the earth. Standard values of the parameters in this model are listed in Table 3.1. Note that only the amplitude of the windstress (Trenberth et al., 1989) and therefore the value of the parameter α differs between the North Atlantic and North Pacific case.

Dimensional parameters			
Parameter	Value	Parameter	Value
r_0	6.37×10^6 m	τ_0	$0.15^\dagger/0.13^\ddagger$ Pa
D	1.0×10^3 m	A_H	2.0×10^2 m ² s ⁻¹
g	9.8 ms ⁻²	U	1.0×10^{-1} ms ⁻¹
ρ	1.0×10^3 kgm ⁻³	Ω	7.3×10^{-5} s ⁻¹
Dimensionless parameters			
Parameter	Value	Parameter	Value
α	$1.0^\dagger/0.88^\ddagger \times 10^{-2}$	E	3.4×10^{-8}
ϵ	1.1×10^{-4}	F	9.8×10^5

Table 3.1: Standard values of parameters in the barotropic SW model. The superscripts † and ‡ refer to North Atlantic and North Pacific, respectively.

3.3.2 Implementation

On each particular domain below, a finite difference discretization is used on a staggered grid. Continental geometry and boundary conditions are taken into account by first discretizing the equations on the sphere and then substituting equations with boundary conditions, according to whether the point is a land point or an ocean point. To ensure overall mass conservation, an integral condition for h over the domain \mathcal{V} is implemented (Schmeits and Dijkstra, 2000); that is,

$$\int_{\mathcal{V}} h \cos \theta d\phi d\theta = |\mathcal{V}|, \quad (3.4)$$

where $|\mathcal{V}|$ is the (dimensionless) area of the domain since the layer depth is scaled with D . The numerical methods for dynamical systems analysis are described in Appendix B.2.

3.4 Bifurcation analysis of the barotropic shallow-water model

In the results below, bifurcation diagrams are computed for steady wind forcing using the Ekman number as a control parameter, the latter being the most uncertain parameter in the model. Every point on a curve in such a bifurcation diagram corresponds to a stationary state and stability is indicated with the linestyle (drawn is stable and dotted is unstable). On the vertical axis, the maximum northward volume transport Φ (in Sv) over a section is shown which is calculated as

$$\Phi = (UDr_0) \max \int_{\phi_w}^{\phi} v h \cos \theta d\phi \quad (3.5)$$

where the maximum is taken both over ϕ and θ . All parameters except the Ekman number are fixed as in Table 3.1 and the North Atlantic and North Pacific cases differ only in the wind-stress pattern and amplitude, the domain size, the basin geometry and slightly in resolution ($\frac{1}{2}^\circ$ and $\frac{5}{12}^\circ$, respectively).

3.4.1 Multiple equilibria of the Kuroshio

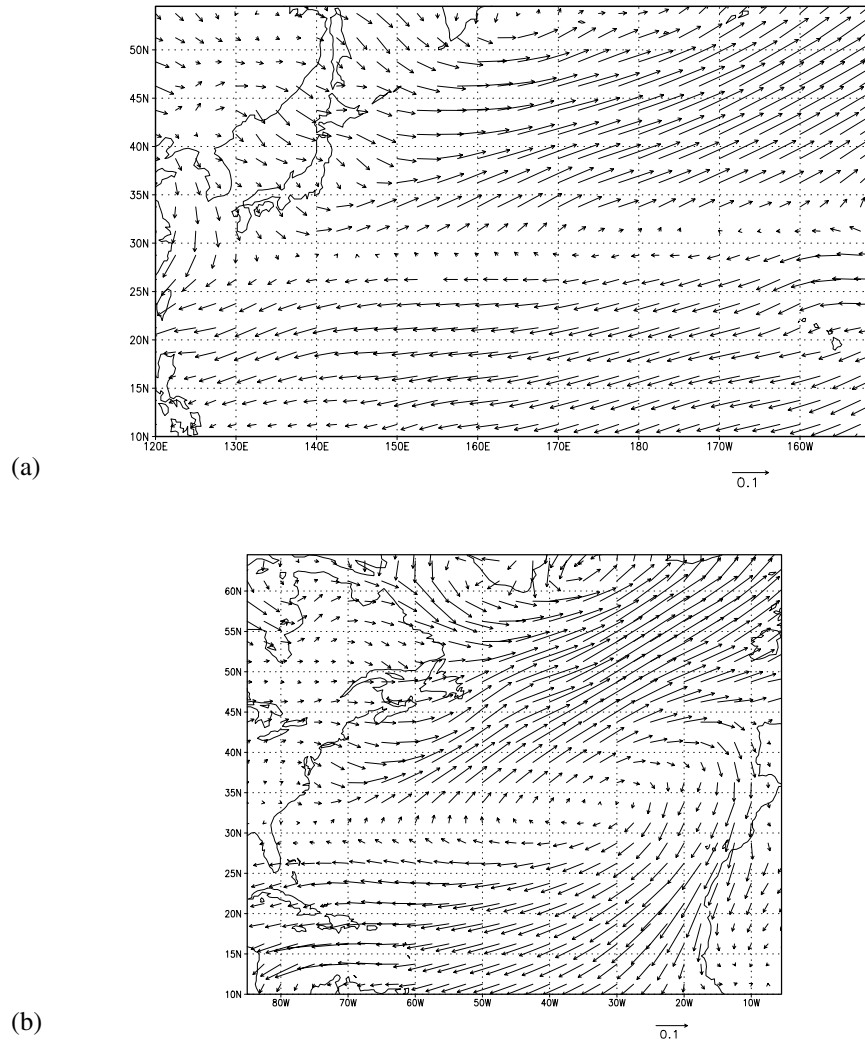


Figure 3.4: Pattern and magnitude (Pa) of the climatological mean windstress forcing (Trenberth et al., 1989) on the (a) North Pacific and (b) North Atlantic domain.

Part of the North Pacific basin $[120^\circ E, 150^\circ W] \times [10, 55]^\circ N$ is considered using a horizontal resolution of $\frac{5}{12}^\circ \times \frac{5}{12}^\circ$. We have taken the 100 m depth contour as the continental boundary because otherwise the modeled Kuroshio would enter the East China Sea. In reality, it is steered by bottom topography, so that it follows a more or less straight path from Taiwan to Japan. The spatial pattern of the climatological windstress forcing (Trenberth et al.,

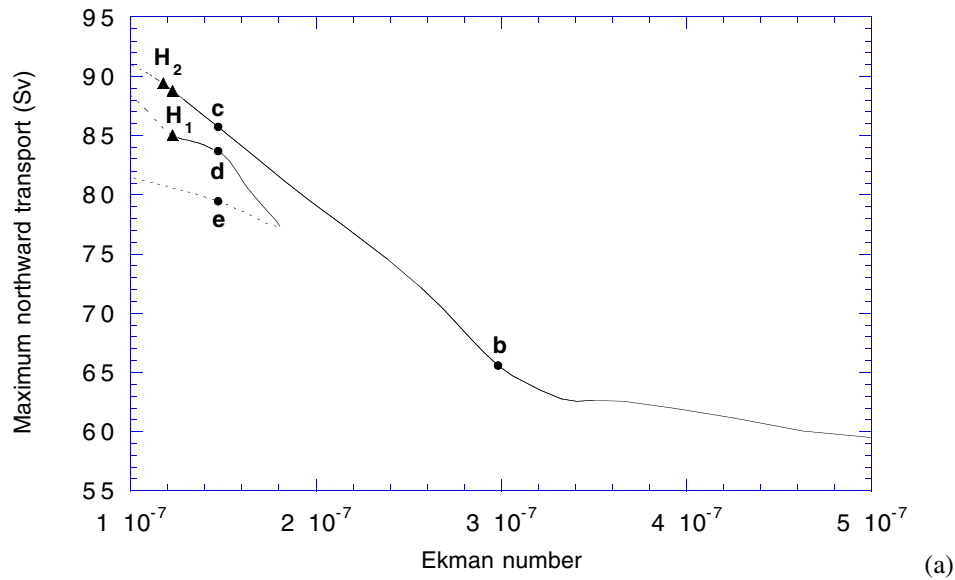


Figure 3.5: (a) Bifurcation diagram for the barotropic shallow-water model on the North Pacific domain with the Ekman number as control parameter. Drawn (dotted) branches indicate stable (unstable) steady states, whereas the Hopf bifurcation points are indicated by triangles. The letters b, c, d and e refer to Fig. 3.5b, 3.5c, 3.5d and 3.5e, respectively. (b) Contour plot of SSH deviations for the steady state solution K_b^S at point b in (a), that is at $E = 3.0 \times 10^{-7}$. The contour levels are scaled with respect to the maximum value of the field. (c) Contour plot of SSH deviations for the steady state solution K_c^S at point c in (a), that is at $E = 1.5 \times 10^{-7}$. (d) Contour plot of SSH deviations for the steady state solution K_d^S at point d in (a), that is at $E = 1.5 \times 10^{-7}$. (e) Contour plot of SSH deviations for the steady state solution K_e^S at point e in (a), that is at $E = 1.5 \times 10^{-7}$.

1989) over the North Pacific domain is displayed in Fig. 3.4a which shows the predominantly easterly (westerly) winds in the lower (mid)latitudes.

The bifurcation diagram for the North Pacific domain (Fig. 3.5a) consists of a perturbed pitchfork bifurcation (Golubitsky and Schaeffer, 1985) and clearly shows that multiple equilibria exist when the lateral friction is small enough. Note that there is quite a range of Ekman numbers where two equilibria are (barotropically) stable. Down to $E = 1.8 \times 10^{-7}$, there is a unique steady solution for each value of the Ekman number (Fig. 3.5a). An example of a stationary solution in this regime is shown as a contour plot of SSH for $E = 3.0 \times 10^{-7}$ in Fig. 3.5b over the whole computational domain. An inset of the flow pattern in the Kuroshio region is presented in Fig. 3.6a, where the colors indicate the magnitude of lateral friction (upper panel), β -effect (middle panel) and inertia (lower panel) in the barotropic potential vorticity equation (similar to the vorticity budget contour plots in the study of Özgökmen et al., 1997). The barotropic potential vorticity equation is derived from (3.1) by taking the

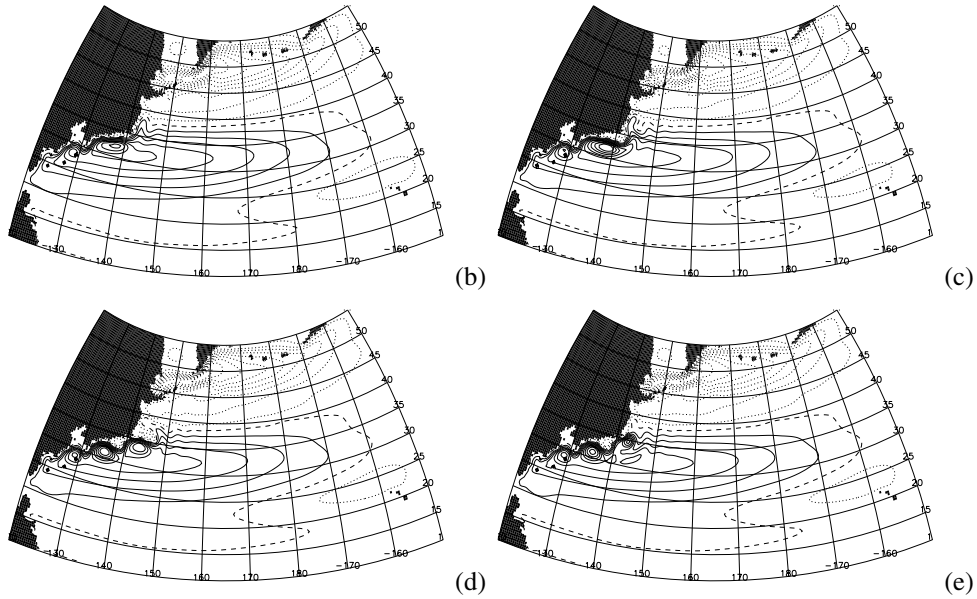


Figure 3.5 (continued)

curl of the momentum equations (3.1a) and (3.1b), and can schematically be written as:

$$\frac{\partial \zeta}{\partial t} = -(I + B + F + W) = 0 \quad (3.6)$$

where ζ is the relative vorticity, I is inertia, B the β -effect, F lateral friction and W the windstress curl. The stationary solution at $E = 3.0 \times 10^{-7}$ displays a Kuroshio path south of Japan, referred to as K_b^S (Fig. 3.6a), quite similar to the observed small meander state (cf. Fig. 1.4). The modeled Kuroshio eventually separates too far north, compared to reality, but at about the same latitude as the simulated Kuroshio in POCM (cf. Fig. 3.1). At this value of E , the transport $\bar{\Phi}$ is about 66 Sv.

The upper branch of solutions in Fig. 3.5a continues to exist for values smaller than $E = 1.8 \times 10^{-7}$, but the solutions lose stability at $E = 1.2 \times 10^{-7}$. They become unstable to one oscillatory mode at a Hopf bifurcation H_1 and to another oscillatory mode at Hopf bifurcation H_2 (Fig. 3.5a). The former oscillatory mode has a timescale of 2 months and has its maximum amplitude in the high shear region to the south of Kamchatka; the latter oscillatory mode has a timescale of 3 months and is located in the separation region of the Kuroshio, where the shear is also high (see section 5.4). A stable stationary solution on this branch is shown for $E = 1.5 \times 10^{-7}$, which is in the multiple equilibria regime, in Fig. 3.5c. It displays a Kuroshio path south of Japan, referred to as K_c^S (Fig. 3.6b), different from both the observed and POCM meander states (cf. Figs. 1.4 and 3.1), with a transport $\bar{\Phi}$ of about 86 Sv. Compared to the solution at $E = 3.0 \times 10^{-7}$ (Fig. 3.5b) to which it is continuously connected, the anti-cyclonic recirculation gyre to the south of Japan has intensified and has caused the Kuroshio to deviate from the coast. The western boundary

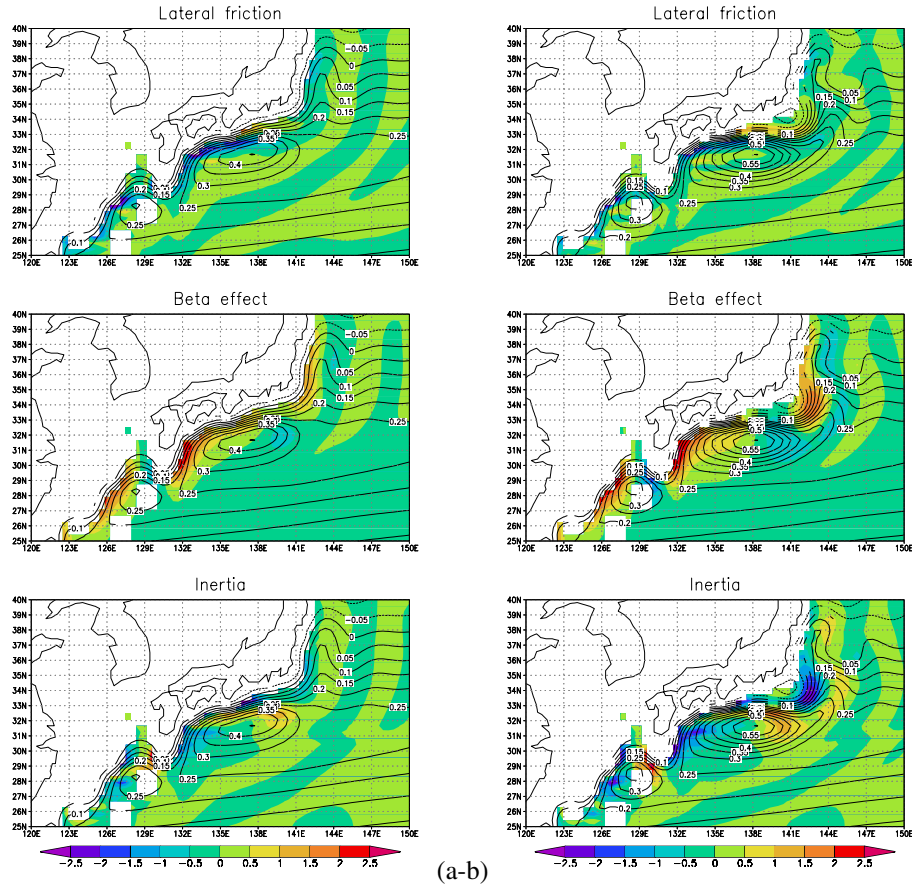


Figure 3.6: (a) As Fig. 3.5b, (b) as Fig. 3.5c, (c) as Fig. 3.5d, and (d) as Fig. 3.5e, but for part of the computational domain $[120, 150]^\circ E \times [25, 40]^\circ N$, and superimposed on a shaded contour plot of the value of the lateral friction term F (upper panel), beta effect term B (middle panel) and inertia term I (lower panel) in the barotropic potential vorticity equation (3.6) (cf. Figs. 1.4 and 3.1).

layer at $E = 1.5 \times 10^{-7}$ is inertially controlled to a large extent (Fig. 3.6b), whereas the boundary layer at $E = 3.0 \times 10^{-7}$ is of the nonlinear Munk type (Fig. 3.6a).

The second branch of solutions exists only for $E < 1.8 \times 10^{-7}$, which is the position of the saddle node bifurcation on this branch. Steady states on the upper part of the branch are stable down to $E = 1.2 \times 10^{-7}$ and become unstable to the same oscillatory mode as the steady states on the upper branch at Hopf bifurcation H_1 (Fig. 3.5a). The solution at $E = 1.5 \times 10^{-7}$ (Fig. 3.5d) displays a Kuroshio path south of Japan, referred to as K_d^S (Fig. 3.6c), quite similar to the observed and POCM large meander states (cf. Figs. 1.4 and 3.1c). It eventually separates at the southeast corner of Honshu, which corresponds to the observed separation point. At this value of E , the transport Φ is about 84 Sv, which is about

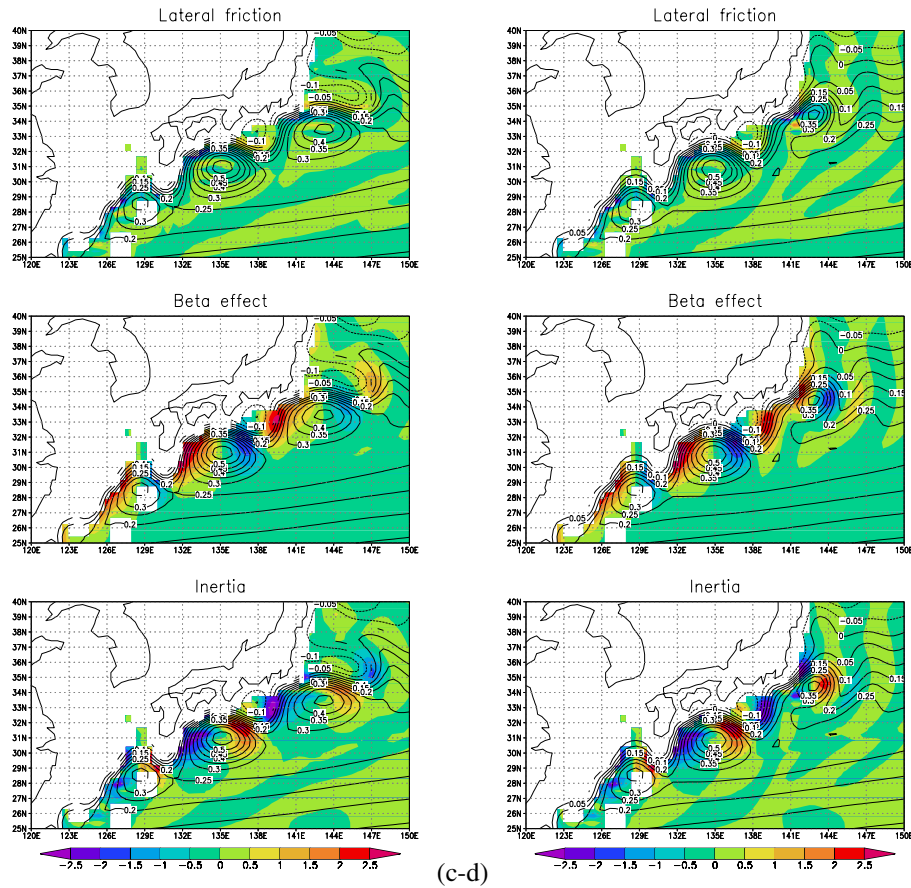


Figure 3.6 (continued)

the same as that of K_e^S (Fig. 3.5c).

The third steady state at $E = 1.5 \times 10^{-7}$, referred to as K_e^S (Fig. 3.5e), is similar to K_d^S (Fig. 3.5d), but it is unstable and it has different final separation behavior. The western boundary layers of K_d^S and K_e^S are highly nonlinear, with lateral friction playing a minor role (Figs. 3.6c and d). Outside the western boundary layers the Sverdrup balance holds for all four steady state solutions. The circulation patterns outside the region of the western boundary current are very similar (Figs. 3.5c, d and e), so that the multiple equilibria are related to the different meandering structures of the Kuroshio. The transports for the stationary solutions in the multiple equilibria regime (Fig. 3.5a) are much larger than current estimates to the south of Japan of about 50-55 Sv (Qiu and Joyce, 1992). This overestimation of the transports is probably due to the neglect of bottom topography in the model.

3.4.2 Multiple equilibria of the Gulf Stream

In this case, the full North Atlantic basin $[85, 5]^\circ W \times [10, 65]^\circ N$ is considered using a horizontal resolution of $\frac{1}{2}^\circ \times \frac{1}{2}^\circ$ as in Schmeits and Dijkstra (2000). The spatial pattern of the climatological windstress forcing (Trenberth et al., 1989) over the North Atlantic domain is plotted in Fig. 3.4b, showing similar features as over the North Pacific domain.

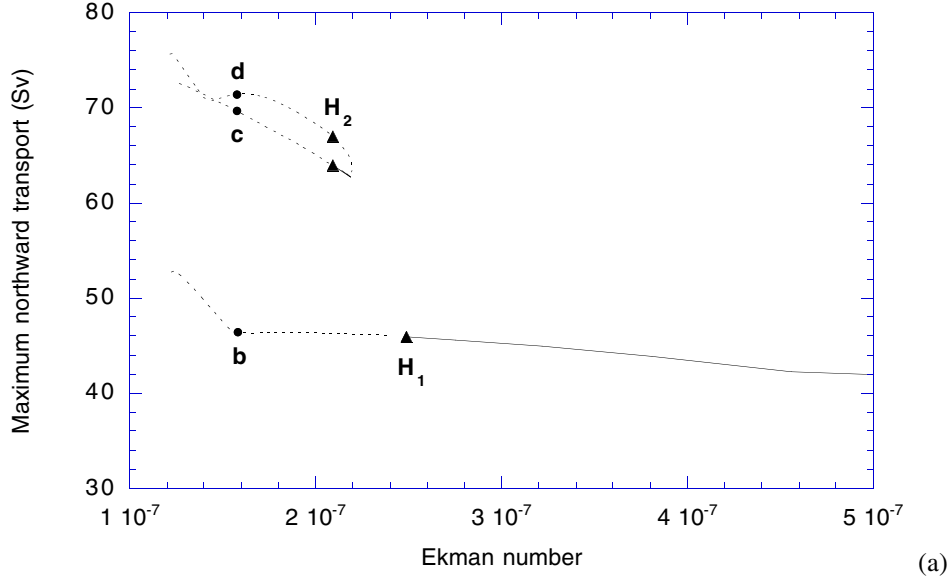


Figure 3.7: Bifurcation diagram for the barotropic shallow-water model on the North Atlantic domain with the Ekman number as control parameter. Drawn (dotted) branches indicate stable (unstable) steady states, whereas the Hopf bifurcation points are indicated by triangles. The letters *b*, *c* and *d* refer to Fig. 3.7b, 3.7c and 3.7d, respectively. The intersection of the upper branch does not indicate a bifurcation; it is due to the choice of norm. (b) Contour plot of SSH deviations for the steady state solution G_b^S at point *b* in (a), that is at $E = 1.6 \times 10^{-7}$. The contour levels are scaled with respect to the maximum value of the field. (c) Contour plot of SSH deviations for the steady state solution G_c^S at point *c* in (a), that is at $E = 1.6 \times 10^{-7}$. (d) Contour plot of SSH deviations for the steady state solution G_d^S at point *d* in (a), that is at $E = 1.6 \times 10^{-7}$.

The bifurcation diagram for the North Atlantic domain is shown in Fig. 3.7a. The diagram again consists of a perturbed pitchfork bifurcation and clearly shows that multiple equilibria exist when the lateral friction is small enough, similar to the North Pacific case. However, there does not exist a range of Ekman numbers where the multiple equilibria are (barotropically) stable. Two solution branches are found; down to $E = 2.2 \times 10^{-7}$, there is only one branch of solutions (Fig. 3.7a). Steady states on this branch are stable down to $E = 2.5 \times 10^{-7}$ and become unstable to one oscillatory mode at the Hopf bifurcation H_1 (Fig. 3.7a). This oscillatory mode has been linked (Schmeits and Dijkstra, 2000, see also section 4.4) to intermonthly variability of the Gulf Stream as found in earlier studies (Lee

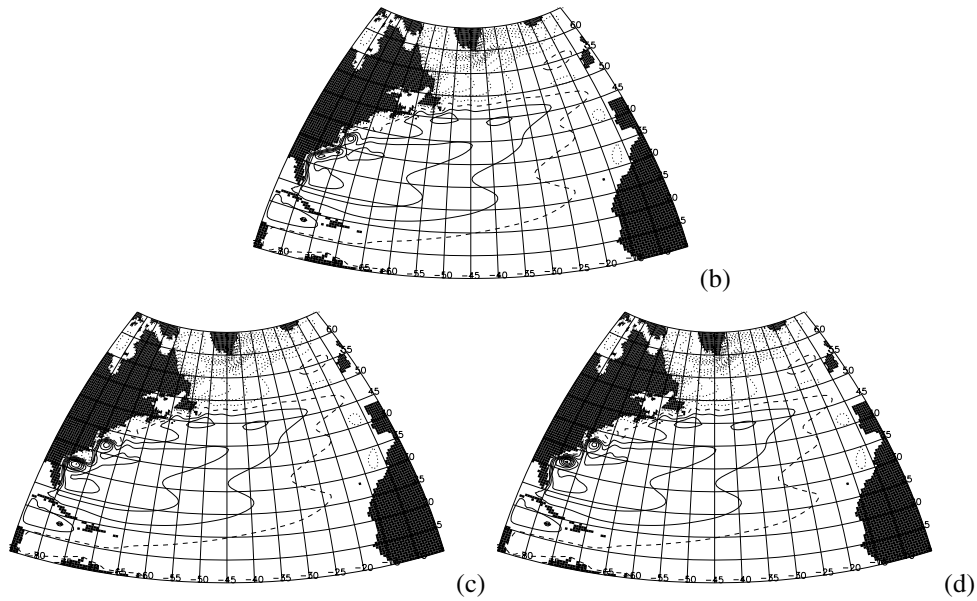


Figure 3.7 (continued)

and Cornillon, 1995).

A stationary solution on this lower branch in Fig. 3.7a is shown as a contour plot of SSH for $E = 1.6 \times 10^{-7}$ in Fig. 3.7b. It displays a Gulf Stream path, referred to as G_b^S (Fig. 3.8a), surprisingly similar to Gulf Stream state G_b^P in POCM (cf. Fig.3.3b), with a transport Φ of about 46 Sv. The small recirculation gyre in the separation region reflects the inability of the flow to rejoin the Sverdrup interior immediately. It first has to get rid of its excess vorticity by recirculating several times. This solution resembles also the 5-year mean plot of upper-layer transport streamfunction for experiment V of Özgökmen et al. (1997) (their Fig. 5a), who have integrated a two-layer QG model (including both quasi-realistic bottom topography and continental geometry), driven by a single-gyre wind forcing. The other branch in Fig. 3.7a exists only for $E < 2.2 \times 10^{-7}$, which is the position of the saddle node bifurcation. A second Hopf bifurcation (H_2) occurs on this branch (Fig. 3.7a) and the period of the oscillatory mode is 2 months. The maximum amplitude of the unstable mode is found in the high shear region to the southeast of Greenland (Schmeits and Dijkstra, 2000, see also section 4.4).

The solution at $E = 1.6 \times 10^{-7}$ on the lower part of the upper branch (Fig. 3.7c) displays a Gulf Stream path, referred to as G_c^S (Fig. 3.8b), quite similar to the observed strongly deflected Gulf Stream (cf. Fig. 1.3). However, the Gulf Stream in the SW model, like the real Gulf Stream, deflects further upstream than Gulf Stream state G_c^P in POCM (cf. Fig.3.3c), and the amplitude of the meander associated with Gulf Stream state G_c^S in the SW model is too large compared with the real Gulf Stream. At this value of E , the transport Φ is about 70 Sv, which is 1.5 times larger than that in Fig. 3.7b, and somewhat larger than current estimates near Cape Hatteras of about 50-65 Sv (Johns et al., 1995). The third steady state at $E = 1.6 \times 10^{-7}$, referred to as G_d^S (Fig. 3.7d), is similar to Gulf Stream solution G_c^S (Fig. 3.7c),

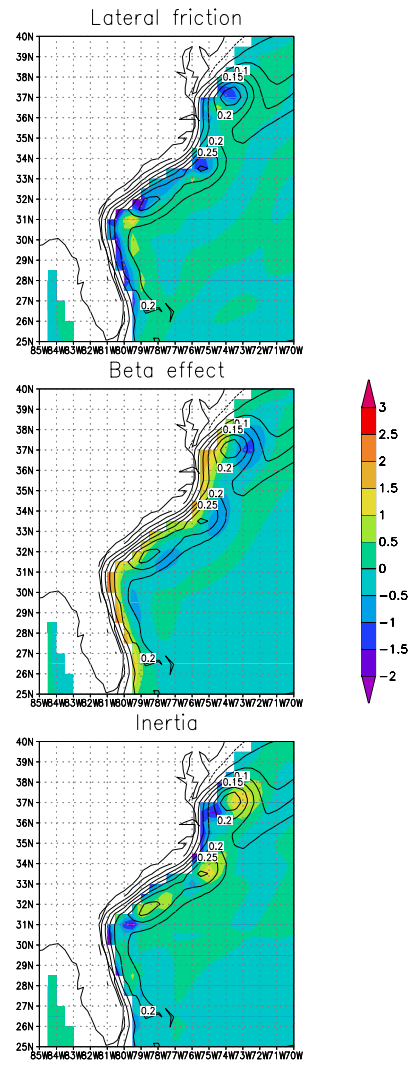
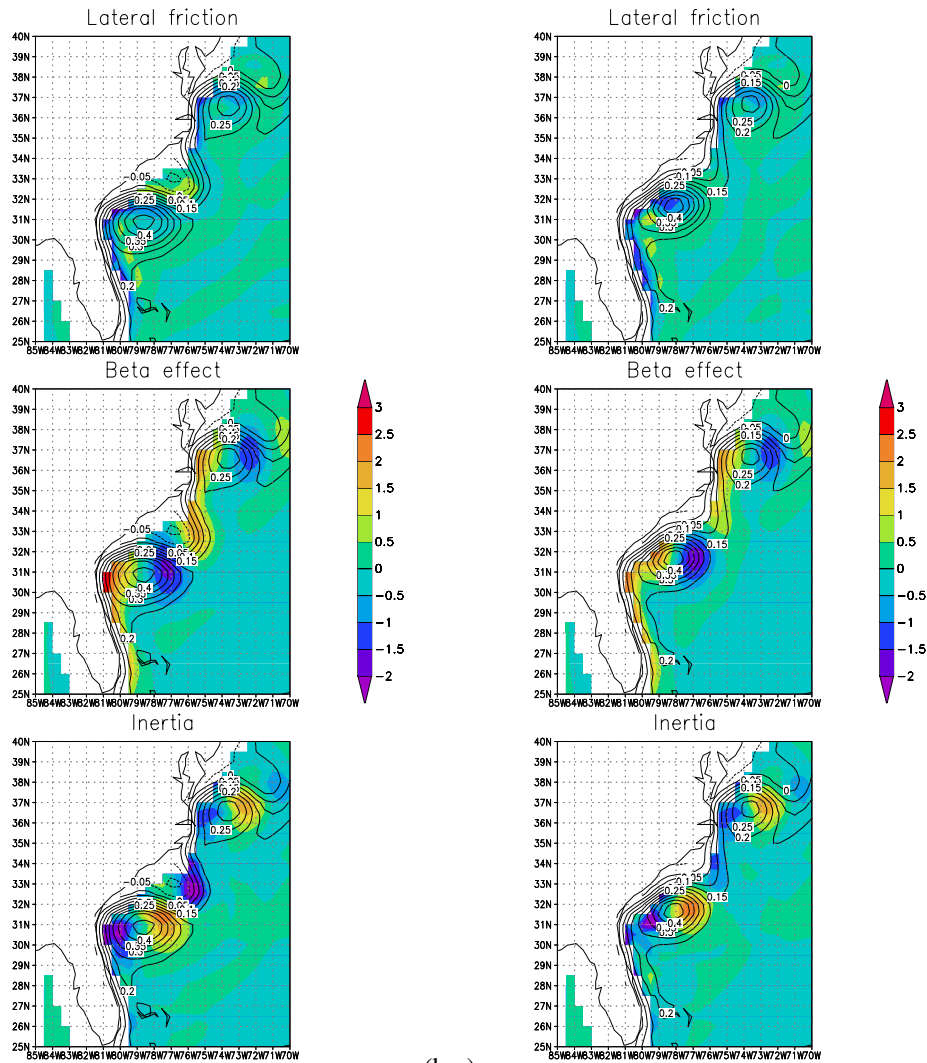


Figure 3.8: (a) As Fig. 3.7b, (b) as Fig. 3.7c, and (c) as Fig. 3.7d, but for part of the computational domain $[85, 70]^\circ W \times [25, 40]^\circ N$, and superimposed on a shaded contour plot of the value of the lateral friction term F (upper panel), beta effect term B (middle panel) and inertia term I (lower panel) in the barotropic potential vorticity equation (3.6) (cf. Figs. 1.3 and 3.3).

but has hardly any cyclonic recirculation cell. The circulation patterns outside the region of the western boundary current are very similar again (Figs. 3.7b, c and d), so that the multiple equilibria are related to the different structures of the Gulf Stream. Outside the western boundary layers the Sverdrup balance holds for all three steady state solutions. For Gulf



(b-c)

Figure 3.8 (continued)

Stream solution G_b^S , the boundary layer is of the nonlinear Munk type (Fig. 3.8a). However, despite the similarity in flow patterns, the vorticity balance in the western boundary layer of experiment V of Özgökmen et al. (1997) (their Fig. 7) is mainly inertially controlled. On the other hand, for Gulf Stream solutions G_c^S and G_d^S the boundary layer is highly nonlinear, with lateral friction playing a minor role (Figs. 3.8b and c).

3.5 Noise-induced transitions

The bifurcation diagrams in the previous section immediately indicate the parameter range in Ekman number where transitions between steady states can occur. In this section, transient flows are computed with the same SW model. Using implicit time integration (Appendix B.2), both steady (Fig. 3.4) and noisy wind forcing (subsection 3.5.1) are employed to determine under which conditions transitions occur.

In all time integrations, described below, the SW model has been run for 6-9 years with the standard set of parameters (Table 3.1) apart from the value of the Ekman number. Since we are interested to monitor whether transitions between different steady states occur, the spatial rms value of the difference between the instantaneous field h^{WBC} and each steady state field \bar{h}_i^{WBC} ($i = 1, 2, 3$), called R_i , is computed in either the Gulf Stream region $[85, 70]^\circ W \times [25, 40]^\circ N$ or the Kuroshio region $[120, 150]^\circ E \times [25, 40]^\circ N$, as follows:

$$R_i = \frac{D \| (h^{WBC} - \bar{h}_i^{WBC}) \|_2}{\sqrt{N_p}} \quad (3.7)$$

Here, $\| \cdot \|_2$ corresponds to the L^2 -norm, and N_p is the total number of grid points in the Gulf Stream or Kuroshio region.

3.5.1 Stochastic windstress forcing

The stochastic windstress forcing has been derived from the monthly mean NCEP Reanalysis 10 m wind data for the period from 1949-1999 (i.e. 612 months). These wind data have been converted to windstress data using a drag coefficient of 1.0×10^{-3} . Besides, the climatological monthly means have been subtracted from the data to form anomalies. The highest variability of the zonal windstress anomalies in the North Atlantic (Fig. 3.9a) is to the south of Iceland where the amplitude of the mean forcing is also high (Fig. 3.4b). In the North Pacific there are several locations with relatively high variability (Fig. 3.9a). As a measure of the "noisiness" of the data (Blanke et al., 1997) we have plotted the one-month-lag autocorrelation of the zonal windstress anomalies in Fig. 3.9b. In the North Atlantic and North Pacific basins the autocorrelation is generally less than 0.2, except in the lowest latitudes.

Figs. 3.9c-d show analogous statistics for meridional stress anomalies. The highest variability in the North Atlantic domain occurs to the southwest of Iceland and to the east of Cuba, and the highest variability in the North Pacific domain occurs to the north of Hawaii (Fig. 3.9c). As was the case for the zonal windstress anomalies, the one-month-lag autocorrelation of the meridional windstress anomalies is generally less than 0.2, except in the lowest latitudes (Fig. 3.9d). We conclude therefore that the windstress anomalies can be used as an uncorrelated noise product. As a phenomenon with short decorrelation time has approximately a flat spectrum at frequencies lower than the inverse of the decorrelation time, we can approximate the stochastic forcing as white on timescales longer than a month. The detailed decorrelation structure of weather noise in timescales shorter than a month has been ignored, on the assumption that this will not matter to the interannual behavior (Blanke et al., 1997).

The maximum amplitude of the windstress anomalies (0.16 Pa for both basins) is of the same order of magnitude as the maximum amplitude of the climatological mean forcing (cf. Table 3.1). Based on the findings of others (e.g. Willebrand et al., 1980) that ob-

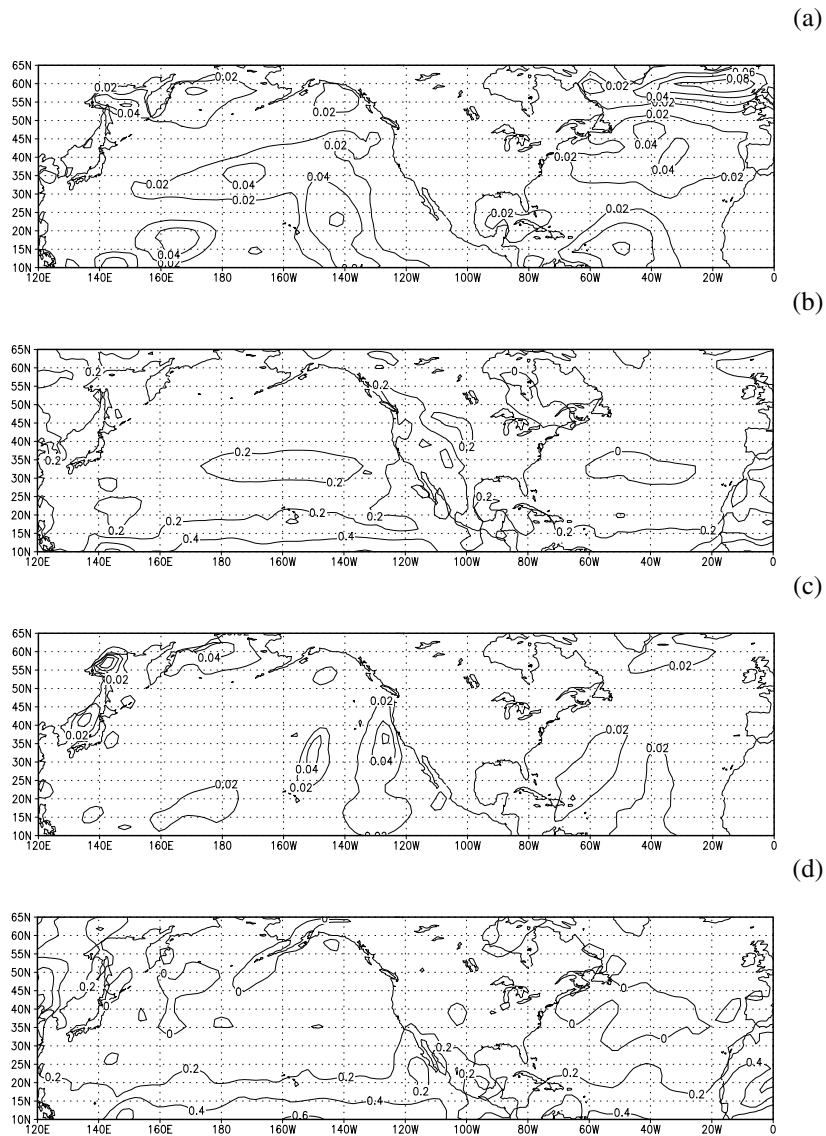


Figure 3.9: Horizontal map of (a) *rms* and (b) 1-month lag autocorrelation computed for the zonal wind stress anomaly over the period 1949-1999. (c-d) As in (a-b) except for the meridional component of the wind stress.

served stochastic forcing produces a primarily barotropic response, it seems justified to use a barotropic ocean model in order to study the effect of stochastic forcing. The stochastic forcing has been implemented in the model as follows. The monthly stochastic forcing is defined by entire windstress anomaly fields chosen randomly among the 612-month sample in order

to preserve the intrinsic spatial coherence of the fields, similar to Blanke et al. (1997).

3.5.2 Transitions between different paths of the Gulf Stream

For $E = 1.6 \times 10^{-7}$, which is a value in the multiple equilibria regime for the North Atlantic basin (Fig. 3.7a), two trajectories were computed. As initial condition the unstable steady solution G_b^S (Fig. 3.7b) indicated by the point b in Fig. 3.7a was chosen which has been slightly perturbed into the direction of the most unstable mode in the case of the climatological mean wind forcing.

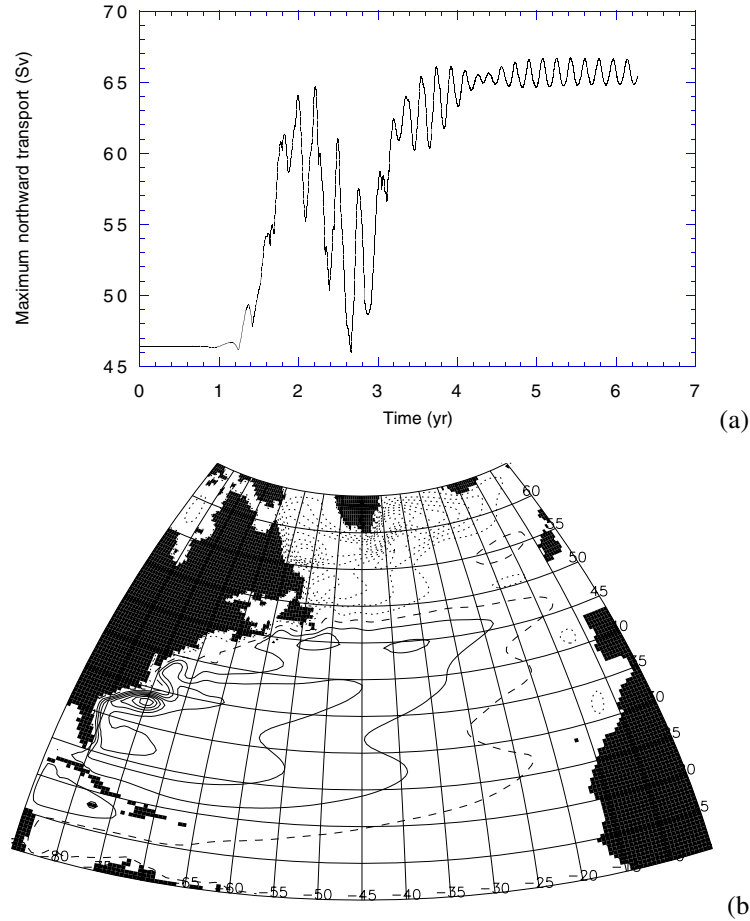


Figure 3.10: (a) Maximum northward transport for the 6-year time integration of the barotropic shallow-water model on the North Atlantic domain with the climatological mean windstress of Fig. 3.4b as forcing and $E = 1.6 \times 10^{-7}$. (b) Mean SSH field of the stable limit cycle (cf. Fig. 3.3c).

For the first trajectory, the flow is forced by the climatological mean wind forcing, there is

no noise added and values of the maximum northward transport are shown in Fig. 3.10a. After an initial transient period, eventually the trajectory is attracted towards a stable limit cycle with a period of about two months, coming from the second Hopf bifurcation in Fig. 3.7a (see also section 6.2.1). The mean SSH pattern associated with the stable limit cycle is shown in Fig. 3.10b; it is very similar to state G_c^P in POCM (cf. Fig. 3.3c).

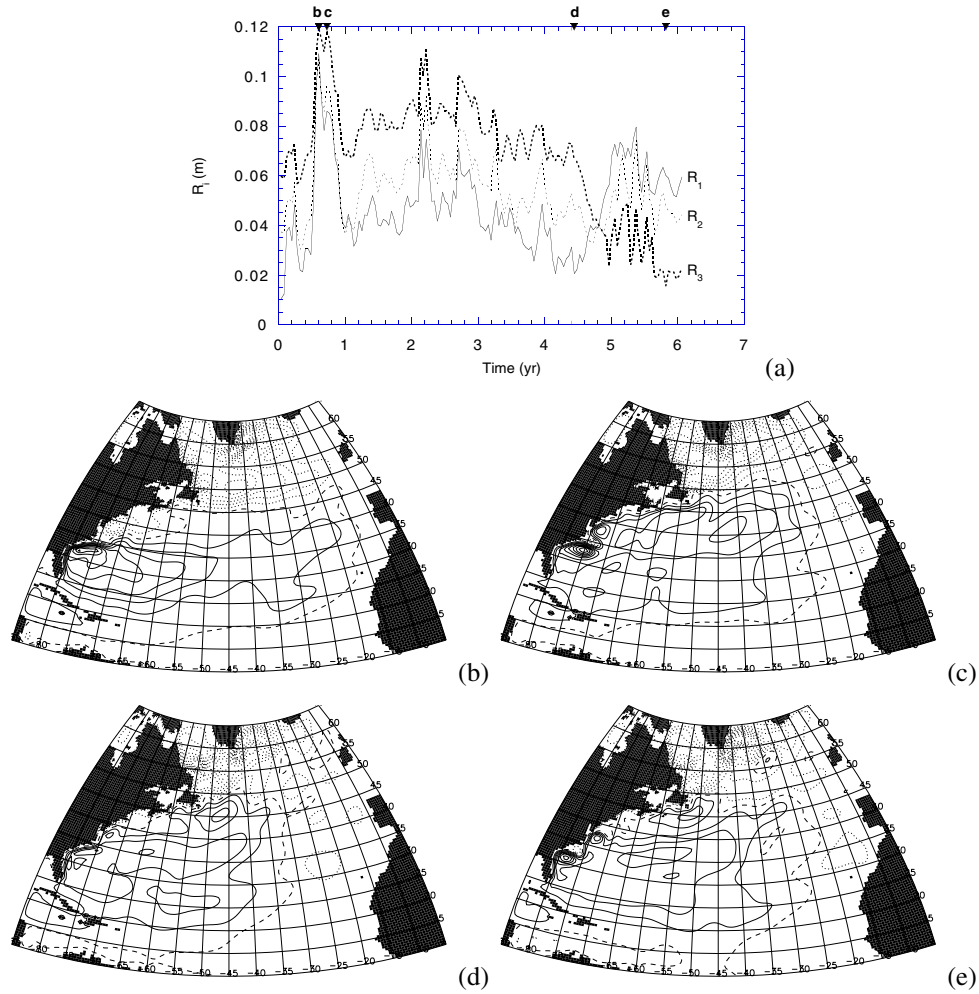


Figure 3.11: Output of the 6-year time integration of the barotropic shallow-water model on the North Atlantic domain with the stochastic forcing added to the climatological mean forcing and $E = 1.6 \times 10^{-7}$. (a) R_i values, defined in (3.7), as a function of time; $i = 1$ (drawn) for the steady state G_b^S (Fig. 3.8a), $i = 2$ (thin dotted) for the steady state G_d^S (Fig. 3.8c), and $i = 3$ (thick dotted) for the steady state G_c^S (Fig. 3.8b). The letters b-e refer to Figs. 3.11b-e. (b-e) Snapshots of SSH deviations for (b) $t = 0.61$ yr, (c) $t = 0.73$ yr (cf. Fig. 3.10b), (d) $t = 4.44$ yr (cf. Fig. 3.7b) and (e) $t = 5.82$ yr (cf. Fig. 3.7c).

For the second trajectory, the stochastic forcing is added to the climatological mean forcing and values of R_i are shown in Fig. 3.11a. The correspondence between the value of i and the steady states is indicated in the figure caption. The trajectory stays more or less close to the unstable steady solution from which it started (G_b^S ; indicated by point b in Fig. 3.7a) during the first five years of the integration, but it is attracted towards one of the other unstable steady solutions (G_c^S ; indicated by point c in Fig. 3.7a) in the last part of the integration. At $t = 0.61$ yr, the trajectory is farthest away from any of the unstable steady state solutions at $E = 1.6 \times 10^{-7}$ (Fig. 3.11a) and a snapshot of SSH at this time is shown in Fig. 3.11b. The Gulf Stream penetrates into the basin to some extent and there are nicely developed northern and southern recirculation gyres. At $t = 0.73$ yr, the trajectory is still far from any of the unstable steady state solutions (Fig. 3.11a), but the SSH pattern (Fig. 3.11c) is quite different from that shown in Fig. 3.11b. At this time, the Gulf Stream is similar to the pattern associated with the limit cycle in the SW model (Fig. 3.10b) and to state G_c^P in POCM (cf. Fig. 3.3c).

At $t = 4.44$ yr, the trajectory is quite close to the unstable steady solution G_b^S (Fig. 3.7b), from which it started. This is confirmed by the SSH pattern (Fig. 3.11d) and the value of R_1 which is only 2.1 cm at this time (Fig. 3.11a). A substantial transition in the flow is observed near $t = 4.8$ yr, with the value of R_1 (R_3) increasing (decreasing) rapidly. At $t = 5.82$ yr, the trajectory is the closest to the unstable steady solution G_c^S (Fig. 3.7c), which is again confirmed by the SSH pattern at this time (Fig. 3.11e), with a R_3 value of only 1.6 cm (Fig. 3.11a).

3.5.3 Transitions between different paths of the Kuroshio

For the North Pacific domain, a value of $E = 1.1 \times 10^{-7}$ was chosen, which is in the multiple equilibria regime (Fig. 3.5a). As initial condition, the unstable steady solution on the upper branch of Fig. 3.5a, with a pattern similar to that of K_c^S (Fig. 3.5c), was chosen. Again, this state is slightly perturbed into the direction of the most unstable mode in the case of the climatological mean wind forcing.

For the first trajectory, the flow is forced by the climatological mean wind forcing and there is no noise added. Values of the maximum northward transport are shown in Fig. 3.12a. The maximum northward transport varies between 81 and 95 Sv, which is the same range of transports as for the multiple steady states at $E = 1.1 \times 10^{-7}$ (cf. Fig. 3.5a). However, it turns out that the trajectory stays relatively close to the unstable steady solution from which it started. There are no transitions to states similar to the other steady state solutions in Fig. 3.5a. In Fig. 3.12b the mean SSH field over the last year of the integration is plotted, the pattern being quite similar to the starting solution.

For the second trajectory, the stochastic forcing is added to the climatological mean forcing and values of R_i are shown in Fig. 3.13a. In this case, the trajectory stays also relatively close to the unstable steady solution from which it started. For another trajectory, again with the additive stochastic forcing but using a smaller value of the Ekman number ($E = 7.3 \times 10^{-8}$), also no transitions in the values of R_i are found (Fig. 3.13b). Several other trajectories have been computed for different values of E , but none of them shows transitions similar to those in the Gulf Stream. Although one cannot exclude that with carefully chosen initial conditions and longer time integrations one might find these transitions,

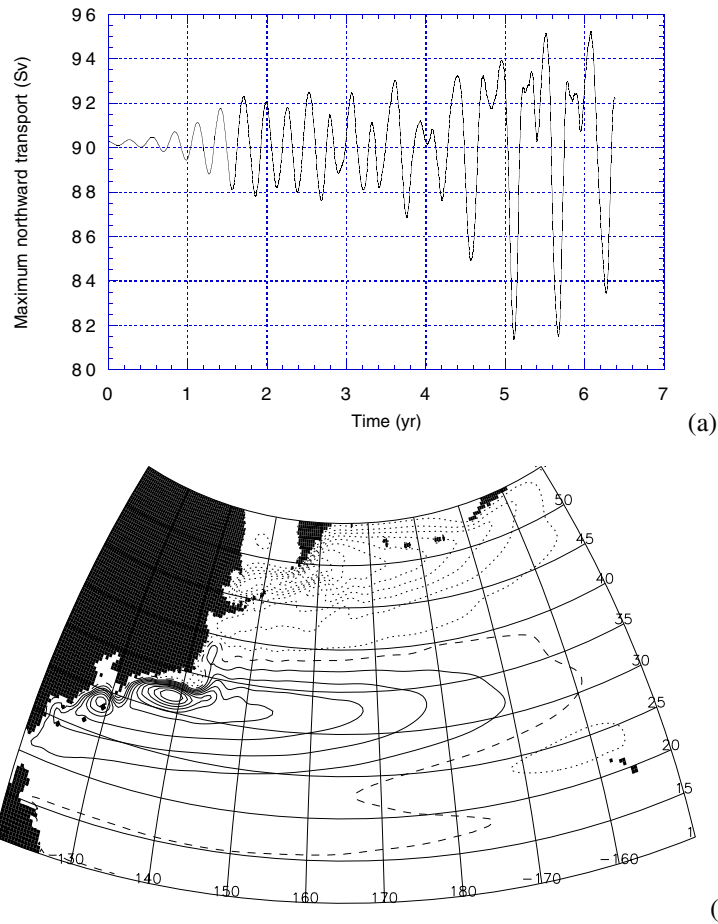


Figure 3.12: (a) Maximum northward transport for the 6-year time integration of the barotropic shallow-water model on the North Pacific domain with the climatological mean windstress of Fig. 3.4a as forcing and $E = 1.1 \times 10^{-7}$. (b) Mean SSH field over the last year of the integration (cf. Fig. 3.5c).

it is remarkable that the noise in the windstress over the Pacific is not able to induce robust transitions between steady states in the multiple equilibria regime.

3.6 Discussion

The results in the previous section raise an interesting issue of non-correspondence of the intermediate model results with observations and high resolution OGCM results. Whereas a clear transition is found between steady states in the Gulf Stream, bimodality is not obvious in observations. On the other hand, there is plenty of observational evidence for bimodality in the Kuroshio, but transitions between steady states in the Kuroshio are hard to find, even

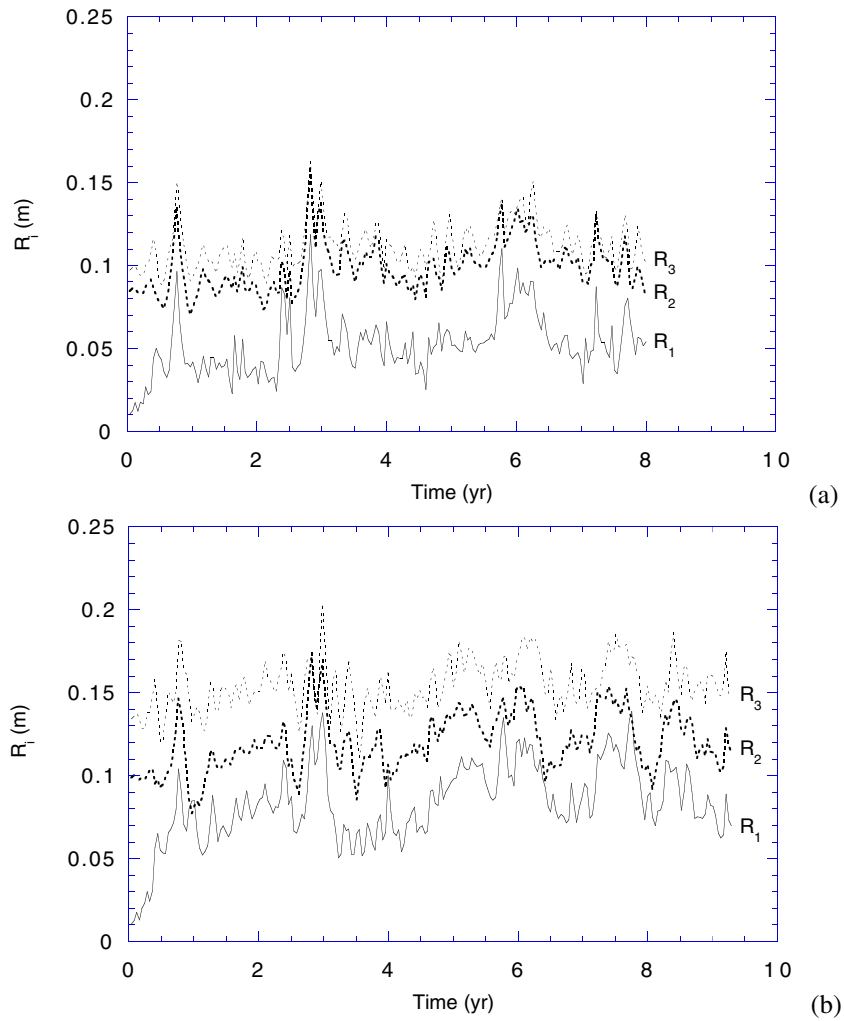


Figure 3.13: (a-b) R_i values, defined in (3.7), as a function of time, for the time integrations of the barotropic shallow-water model on the North Pacific domain with the stochastic forcing added to the climatological mean forcing and (a) $E = 1.1 \times 10^{-7}$ and (b) $E = 7.3 \times 10^{-8}$; $i = 1$ (drawn) for the respective steady state similar to K_e^S (Fig. 3.6b), $i = 2$ (thick dotted) for the respective steady state similar to K_e^S (Fig. 3.6d), and $i = 3$ (thin dotted) for the respective steady state similar to K_d^S (Fig. 3.6c).

in a parameter regime where dynamically multiple states are allowed. What can be learned from this?

Although baroclinic effects and bottom topography are neglected, the intermediate complexity model cannot be rejected *a priori* to be able to describe the main structure of flow

patterns associated with both western boundary currents. For the Gulf Stream, there is a close correspondence between the steady state G_b^S in the intermediate complexity model (Fig. 3.8a) and the Gulf Stream pattern G_b^P in POCM (Fig. 3.3b) and between the mean state of the limit cycle in the intermediate complexity model (Fig. 3.10b) and the Gulf Stream pattern G_c^P in POCM (Fig. 3.3c). For the Kuroshio, the correspondence between the steady states in the intermediate complexity model (Figs. 3.6b-d) and the meander states in POCM (Figs. 3.1b-c) is also reasonable, although less good than for the Gulf Stream.

The results in Qiu and Miao (2000) are qualitatively consistent with the bifurcation diagram in Fig. 3.5a. For a realistic value of the windstress amplitude, variations between a straight path and a meander path have been found on interannual timescales (Qiu and Miao, 2000, their Fig. 7), whereas the Kuroshio stays in the straight path state after an initial period of adjustment when the windstress forcing is reduced by 25% (Qiu and Miao, 2000, their Fig. 14). The model run with the realistic value of the windstress amplitude (and a value of the lateral friction coefficient of $800 \text{ m}^2\text{s}^{-1}$, which corresponds to a value of the Ekman number of 1.35×10^{-7} in our SW model) is probably in the multiple equilibria regime (consistent with Fig. 3.5a), whereas the model run with reduced windstress amplitude (equivalent with a larger value of the Ekman number in our SW model) is probably in that part of parameter space where there is only one state, i.e. the straight path state (consistent with Fig. 3.5a). This leads us to the view that the bimodality of the Kuroshio in the results of Qiu and Miao (2000) is also due to the existence of multiple equilibria. This contrasts their view, namely that the bimodality is a result of a self-sustained internal oscillation, which would imply the existence of a Hopf bifurcation, at which an interannual mode destabilizes.

The bifurcation diagram in Fig. 3.5a is also qualitatively consistent with analyses of observed sea level data by Kawabe (1995). He has concluded that the Kuroshio always takes a non-large meander path (i.e. is in the single equilibrium regime) for small transport, i.e. small amplitude of the forcing (equivalent with a relatively large Ekman number in our SW model), but can take either a large meander path or a non-large meander path (i.e. is in the multiple equilibria regime) for large and medium transports (corresponding to a relatively small Ekman number in our SW model).

The structure of multiple equilibria is also a robust dynamical property of the barotropic model (section 1.3). The existence of the multiple equilibria in the barotropic SW model with realistic geometry and forcing can be traced back to its basics (Dijkstra and Molemaker, 1999) as a spontaneous symmetry breaking. This symmetry breaking was analysed in the highly idealized case in a rectangular basin with symmetric windstress forcing (Cessi and Ierley, 1995) and the associated physical mechanism (Dijkstra and Katsman, 1997) involves an asymmetric weakening/strengthening of the subpolar/subtropical gyre with a positive feedback from the resulting change in horizontal shear. The multiple equilibria in the simple case deform into solutions with different separation behavior of the Gulf Stream for the realistic case and no new equilibria are introduced by the change in geometry (Dijkstra and Molemaker, 1999). The results here, in particular the correspondence between the patterns of the different states, indicate that the multiple equilibria persist in a state-of-the-art ocean model, such as POCM.

Having the multiple equilibria in both western boundary currents, the presence of noise in the windstress forcing is able to induce a transition in the Gulf Stream (Fig. 3.11a) whereas it is unable to induce transitions in the Kuroshio (Fig. 3.13). That the spatial structure of the

noise is important has already be pointed out in Sura et al. (2001). They show that regime transitions are induced by the inhomogeneity of the white noise variance. Indeed, the variance of the windstress forcing over the North Atlantic basin is spatially much more inhomogeneous than that of the windstress forcing over the North Pacific basin (Fig. 3.9a).

If multiple steady states are indeed the underlying cause of the bimodality of the Kuroshio, then there must be physical effects, not considered in the barotropic SW model, which destabilize the Kuroshio mean flow. Simultaneously, similar or additional effects neglected must stabilize the flow in the Gulf Stream area, because actual observed bimodality is weak. Stratification can certainly influence the mean flow through pressure gradients, and additionally instabilities, i.e. baroclinic eddies, can be generated that may cause a strong rectification of the mean state. Baroclinic instability is a major element in the mechanism of transition from the straight to the meander path suggested in Qiu and Miao (2000), but transitions between both paths have also been found in barotropic models (e.g. Chao, 1984). Moreover, there seems to be no reason why the baroclinic effects would differ substantially between the Gulf Stream and Kuroshio. A second effect neglected, namely bottom topography, is substantially different in both regions and this seems to be one of the possibilities to explain the different behavior of the western boundary currents. In a two-layer context, bottom topography does not change the steady state solutions as presented for the barotropic case, since the bottom layer is always motionless in steady state. However, when time integrations are performed, bottom topographic features in the Kuroshio region may induce transitions between the steady states, whereas bottom topography in the Gulf Stream region may prohibit transitions. As it has a large effect on the sea surface height in a barotropic model, bottom topography was not incorporated here. While one also cannot exclude the effect of coupled ocean-atmosphere interaction on the stability of the flows, another important stabilizing mechanism in the North Atlantic may be the presence of the strong deep western boundary current (DWBC), which has been shown to fix the separation point in an idealized model context (Tansley and Marshall, 2000). The DWBC in the North Pacific is much weaker and is shielded from the southern coast of Japan by the Izu Ridge.

The results here also put the difficulties of the separation of the western boundary currents in high resolution ocean models (Özgökmen et al., 1997; Chassignet et al., 2001; Smith et al., 2000) in a different perspective. Our results suggest that the problems may not only be related to errors in representation of topography, forcing or friction, but substantial complexity is introduced through the nonlinear effects in the western boundary current region. In the SW model the Gulf Stream solutions G_c^S and G_d^S (Figs. 3.8b-c) and the Kuroshio in the multiple equilibria regime (Figs. 3.6b-d) are to a large extent inertially controlled, whereas Gulf Stream solution G_b^S (Fig. 3.8a) and Kuroshio's meander state K_b^S (Fig. 3.6a) are more viscously controlled. A delicate balance in the western boundary region may therefore determine which type of path will be present during a certain time interval of the simulation.

There may be a concern with respect to the resolution of the viscous sublayers of the multiple steady state solutions (Figs. 3.6b-d and 3.8a-c), as Smith et al. (2000) have suggested that inadequate resolution of the Munk layer can lead to changes in the Gulf Stream behavior. However, having the constraint that we cannot easily repeat the calculations at much higher resolution, we think that the results on bimodality are robust, even in the regime of small Ekman numbers considered. This is based on the robustness of the (im)perfect pitchfork (and hence of the multiple equilibria) structure in a hierarchy of models, as mentioned above. This

hierarchy includes models with very high resolution in the western boundary layer, such that the viscous sublayer is accurately resolved. Therefore, we think that the remark of Smith et al. (2000) about the regime transitions they found in the Gulf Stream during the spinup phase of the Los Alamos Parallel Ocean Program model supports our view, i.e. that there are multiple steady states in the Gulf Stream, at least in numerical models and even on a truly eddy-resolving resolution ($\frac{1}{10}^\circ$).

At this point, it is still difficult to relate the different amounts of northward heat transport associated with the different paths in POCM to that in reality. The meridional heat transport associated with Kuroshio's small meander state K_b^P (Fig. 3.1b) may be larger than that of Kuroshio's large meander state K_c^P (Fig. 3.1c) because of the differences in meridional heat advection. An analogous argument holds for Gulf Stream patterns G_b^P (Fig. 3.3b) and G_c^P (Fig. 3.3c), respectively. However, the Kuroshio (Gulf Stream) path in POCM is still quite different from the observed time mean Kuroshio (Gulf Stream) path, which penetrates far more into the North Pacific (Atlantic). Hence, the heat transport computed with POCM likely underestimates the actual changes due to a transition in the Kuroshio (Gulf Stream) path. Very high resolution simulations with (improved) ocean models, yielding more realistic Kuroshio (Gulf Stream) paths (e.g. Chassignet et al., 2001; Smith et al., 2000), and longer time series of high resolution data from observations are needed to shed more light on the changes in heat transport associated with the different meandering (deflection) paths.

Chapter 4

Physics of the 9-month variability in the Gulf Stream region^{*}

4.1 Introduction

The Gulf Stream transports a significant amount of heat northward, and it is therefore important to understand its temporal variability on different timescales. In early days, this variability has been studied using in situ data (Hansen, 1970; Fuglister, 1972) but more recently these data have been complemented with satellite-derived observations. At the moment, there is a sufficiently long time series to study variability on timescales up to a year in quite detail. In Table 4.1, details of the spatial and temporal resolution of the data and the methods of analysis are given for several of these studies. Maul et al. (1978) used infrared measurements from the Geostationary Operational Environmental Satellite (GOES) mission over a two-year (1976-78) period and found a dominant timescale of 45 days in the meandering of the Gulf Stream near New England. Using a combination of infrared data and observations of sea-level height anomalies derived from the GEOSAT altimeter over the period November 1986-December 1988, Vazquez et al. (1990) concluded that the annual signal in Gulf Stream variability is dominated by the meandering of the current. The latter study was extended in Vazquez (1993), using complex empirical orthogonal function (CEOF) analysis on the same dataset. It appeared that four CEOFs could account for 60% of the variability and each of these represented different propagating signals, which were shown to be related to Rossby wave propagation, eddy-stream interactions and bottom topography.

Data from cycles 3-54 from the TOPEX/Poseidon mission were analyzed by Wang and Koblinsky (1995) and three dominant modes of variability were identified through empirical orthogonal function (EOF) analysis. The first EOF was associated with the seasonal cycle but the second EOF showed low-frequency wave activity (of about annual period), and by computing eddy kinetic energies and the Reynolds stresses they concluded that bottom topography plays an essential role in the latter component of variability. The third EOF had

^{*}This chapter is based on Schmeits, M. J., and H. A. Dijkstra, 2000: Physics of the 9-month variability in the Gulf Stream region: combining data and dynamical systems analyses. *J. Phys. Oceanogr.*, **30**, 1967-1987.

Overview of satellite studies of the Gulf Stream region				
Data	Region	Period		Resolution
Infrared ^a	91° – 44° W	1980-85	weekly	0.5°
Infrared ^b	86° – 70° W	1976-78	daily	pointwise
GEOSAT ^c	80° – 50° W	1986-88	weekly	0.5°
GEOSAT ^d	75° – 60° W	1986-88	10 days	0.25°
T/P ^e	80° – 30° W	cycles 3-54	10 days	1.0°
AVHRR ^f	75° – 60° W	1982-89	2 days	20 km
GEOSAT ^g	75° – 45° W	1986-89	1 day	1.0°
T/P ^h	80° – 30° W	74 cycles	10 days	1.0°
T/P ⁱ	97° – 32° W	154 cycles	10 days	1.0°

Table 4.1: Examples of studies of the Gulf Stream path and variability using satellite data. In the first column, the type of data source is sketched, with T/P indicating the TOPEX/Poseidon mission. The second and third columns provide the region and period, respectively, considered in each study and the fourth column gives the temporal and spatial resolution used. Pointwise indicates that no interpolation to a grid was done. ^a: Auer (1987), ^b: Maul et al. (1978), ^c: Vazquez et al. (1990), ^d: Vazquez (1993), ^e: Wang and Koblinsky (1995), ^f: Lee and Cornillon (1995), ^g: Kelly et al. (1996), ^h: Wang and Koblinsky (1996), ⁱ: This study (Schmeits and Dijkstra, 2000).

a period of 8 months and external forcing through bottom topography was suggested as the generation mechanism.

Using AVHRR-derived infrared images for the period April 1982 through December 1989, Lee and Cornillon (1995) found two dynamically distinct modes of variability of the path of the Gulf Stream. The first mode of variability is associated with large-scale lateral shifts of the mean path having an annual period. These shifts are presumably caused by atmospheric forcing, partly through the changes in downward heat flux (Wang and Koblinsky, 1996) and partly through the changes in wind forcing over the area (Kelly et al., 1999). The second mode of variability is associated with changes in meandering intensity having a 9-month dominant periodicity. The cause of the 9-month periodicity in meandering intensity is not explained but Lee and Cornillon (1995) suggest that it is related to internal oceanic dynamics.

From all the work above, it is clear that variations in the path of the Gulf Stream exist on a timescale that is slightly smaller than annual and that is unlikely to be caused directly by variations in atmospheric forcing. Internal ocean dynamics, that is, intrinsic variability due to nonlinear interactions in the current itself, are a likely origin, but the question is whether a clear candidate of such a mode of variability can be found.

Recently, the stability and variability of the double gyre wind-driven ocean circulation has been investigated systematically within an hierarchy of models (Jiang et al., 1995; Cessi and Ierley, 1995; Speich et al., 1995; Dijkstra and Katsman, 1997; Katsman et al., 1998; Dijkstra and Molemaker, 1999, section 1.3). Bifurcations mark the transitions between different regimes of behavior and a bifurcation diagram describes the behavior of the dynamical system in phase space. Hopf bifurcations are important in the study of the origin of a particular type of variability because they mark the transition to temporal behavior (Appendix B.1). Us-

ing 1.5-layer quasigeostrophic (QG) models (Cessi and Ierley, 1995; Dijkstra and Katsman, 1997) and 1.5-layer shallow-water (SW) models (Jiang et al., 1995; Dijkstra and Molemaker, 1999) in rectangular basins, it was found that the idealized double gyre flows become unstable to two types of barotropic modes: basin modes and gyre modes. The timescales of the former are a couple of months, whereas the latter instabilities have timescales in the order of years. In two-layer QG models (Dijkstra and Katsman, 1997; Katsman et al., 1998), additional baroclinic instabilities appear having an intermonthly timescale (see also chapter 2).

By using a hierarchy of β -plane models, starting from a 1.5-layer QG model in a rectangular basin with sinusoidal windstress forcing toward a 1.5-layer shallow-water model in a basin with realistic geometry and windstress forcing, Dijkstra and Molemaker (1999) found that the basic structure of the steady states and most unstable modes remains qualitatively intact. Multiple equilibria found in the QG model "deformed" into multiple flow paths of the Gulf Stream. Furthermore, the modes of variability remained closely related, seemed to depend only on the local properties of the gyres near the western boundary, and were not much influenced by the geometry of the basin.

Since some of these dynamical modes have near-annual timescales, we investigate in this paper the hypothesis that the origin of the 9-month variability found in the Gulf Stream region is a barotropic instability of the western boundary current/midlatitude jet system of the North Atlantic. The approach is along three paths: First, multivariate time series analysis techniques will be used to extract statistically significant modes of variability in sea surface temperature (SST) and T/P sea surface height (SSH) observations. Second, output from the Parallel Ocean Climate Model (POCM) (Semtner and Chervin, 1992; Stammer et al., 1996) is analyzed with the same statistical techniques giving information on the vertical structure of the variability. Finally, the instabilities of the barotropic North Atlantic wind-driven circulation will be studied within a full basin-scale barotropic shallow-water model with realistic geometry and forcing. The datasets used in this study and their preprocessing are presented in section 4.2. The results of the data analysis and of the shallow-water model's bifurcation analysis are given in sections 4.3 and 4.4, respectively, with a discussion in section 4.5.

4.2 Datasets and their preprocessing

The datasets used in this study are monthly SST fields from Reynolds and Smith (1994), relative sea surface height observations from the NASA TOPEX/Poseidon (T/P) Altimeter Pathfinder Dataset and the POCM output for the Gulf Stream region (section 3.2). The SST data are derived from a blend of remotely sensed and in situ data and then subjected to an optimum interpolation (OI) analysis (Reynolds and Smith, 1994). The monthly SST fields are provided on a regular 1° latitude/longitude grid. For the separate analysis of SST we use data in the Gulf Stream region ($24^\circ - 48^\circ N, 97^\circ - 32^\circ W$) from 1982-1996.

The T/P dataset consists of time, positions and relative sea surface height observations to which all types of corrections have been applied over cycles 1-154. The data processing used to construct the dataset has been described at <http://neptune.gsfc.nasa.gov/~krachlin/opf/algorithms.html>. The satellite orbit results in repeated ground tracks every 10 days. A mean relative sea surface height was computed at

each grid point for all 154 cycles. Residual SSH anomalies are then computed by subtracting the mean relative sea level from each observation. Outliers (SSH anomalies > 1.5 m) are excluded from the dataset.

The T/P SSH anomalies along ground tracks are interpolated in space to a regular 1° latitude/longitude grid and in time to a resolution of 10 days for the separate analysis of SSH and to 1 month for the combined analysis of SSH and SST. A Gaussian interpolation is used with a decorrelation scale of 2° and a cutoff radius of 6° in space and a decorrelation scale of 10 days and a cut off of 30 days in time. The cutoff radius of 6° corresponds to the Nyquist wavenumber for the 3-degree T/P track spacing. Although the Gaussian interpolation is not equivalent to a low-pass filter with a cut off of 6° , all wavelengths up to the decorrelation scale of 2° have been filtered out and about 65% of the amplitudes of the wavelength of 6° (Vossepoel, 1995). The choice of the spatial decorrelation scale is a compromise between avoiding aliasing on the one hand and retaining the interpolated signal well above the measurement error on the other hand. For the separate analysis of SSH and the combined analysis of SST and SSH we use data in the same region as above from November 1992 to November 1996.

The seasonal cycle has been eliminated from the SST dataset by computing anomalies about the 1982-96 monthly climatology, from the T/P dataset by calculating anomalies about the 1992-96 10-daily/monthly climatology, and from the POCM output by computing anomalies about the 1979-97 monthly climatology. In this way, effects of the seasonal atmospheric forcing have been removed from the datasets. Besides, all datasets have been prefiltered with principal component analysis (PCA) (Preisendorfer, 1988) in order to reduce the number of spatial degrees of freedom in the datasets. Finally, the statistical mean at each point has been removed prior to the analysis. The multivariate data are then analyzed with the aid of multivariate time series analysis techniques described in Appendix A.

4.3 Results of the data analysis

4.3.1 Spatiotemporal variability of SST observations

To reduce the number of spatial dimensions, we initially perform a conventional PCA of the normalized nonseasonal SST data and retain 24 PCs, which account for 90% of the variance. These PCs provide the L input channels for the M-SSA algorithm. We have 15 years of data, so $N = 180$, and use a standard window length M of 60 months.

The Monte Carlo significance test for M-SSA (Allen and Robertson, 1996) is applied first in order to investigate which oscillating patterns contain more variance than would be expected if the data were generated by red noise. Both data and surrogates are projected onto the ST-PCs of the null-hypothesis basis (Allen and Robertson, 1996) and the result is shown in Fig. 4.1a. Three data eigenvalues, with associated frequencies 0.11, 0.15, and 0.18 month^{-1} , are found to be significant. Now that we have used the null-hypothesis basis to establish that there is some evidence of oscillations, we have to examine the data-adaptive basis for pairs of ST-PCs, which characterize those oscillations (Allen and Robertson, 1996). In Fig. 4.1b both data and surrogates are projected onto the data ST-PCs. The test has picked out three pairs associated with the same frequencies as the ones that were indicated as significant in

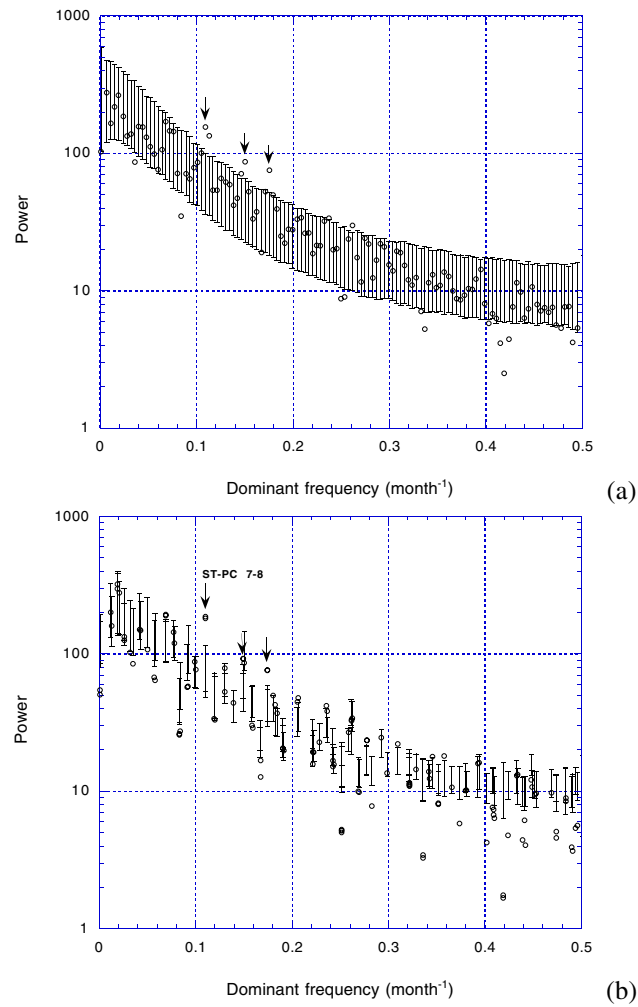


Figure 4.1: Monte Carlo significance test of nonseasonal monthly SST data in the Gulf Stream region for the period 1982-1996, using $L = 24$ PCs from a conventional PCA as the input channels. Shown are projections of the SST data onto (a) the AR(1) null-hypothesis basis and (b) the data-adaptive basis, with a 60-month window ($M = 60$). Open circles show the data eigenvalues, plotted against the dominant frequency of the corresponding ST-PC. The vertical bars show the 95% confidence interval computed from 1000 realizations of a noise model consisting of L independent AR(1) processes with the same variance and lag-1 autocorrelation as the input data channels.

Fig. 4.1a. The most dominant pair of these three is ST-PC 7-8 (Fig. 4.1b), which explains 7% of the variance in the 24 leading PCs. This is not much, but the test has indicated that the first six ST-PCs (which together explain 26% of the variance in the 24 leading PCs) contain no more variance than would be expected if the data would consist of a set of independent

AR(1) processes.

M (months)	significant periods (months)
40	9, 6
60	9, 7, 6
80	9, 6, 4

Table 4.2: Output from the Monte Carlo significance test for M -SSA on the SST data for M between 40 and 80 months.

To check the robustness of these results with respect to different values of the window length M , Table 4.2 shows the timescales, indicated as significant by the Monte Carlo test for M -SSA, for M between 40 and 80 months. It is clear from this table that the variability on timescales of 9 and 6 months is robust.

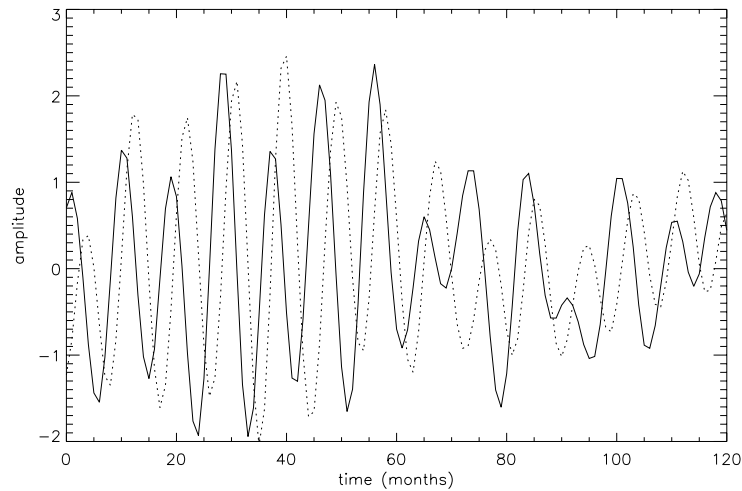


Figure 4.2: Time series of M -SSA principal component (ST-PC) pair 7-8 of Gulf Stream SST; the amplitude scale is arbitrary. The 10-year time span in the horizontal axis corresponds to $N - M + 1$, which is the length of the ST-PC time series.

As can be seen in Fig. 4.2, ST-PC 7 and 8 are in quadrature, which suggests that the pair represents an oscillating statistical mode (Plaut and Vautard, 1994) with a dominant period of 9 months. The same 9-month mode was also indicated as significant in the case where the domain of analysis was extended to the whole North Atlantic basin. In order to isolate the part of the signal involved with this oscillation RC 7-8 has been calculated and the reconstructed anomaly patterns of SST have been plotted in Fig. 4.3 for five phases during the oscillation. The starting time was chosen to be October 1985, when meandering intensity was at its maximum in the 1980s (Lee and Cornillon, 1995) and each subsequent picture is 1 month later; together the pictures show nearly half of the cycle of the oscillation. The maximum

amplitude of the anomalies is 0.6 K.

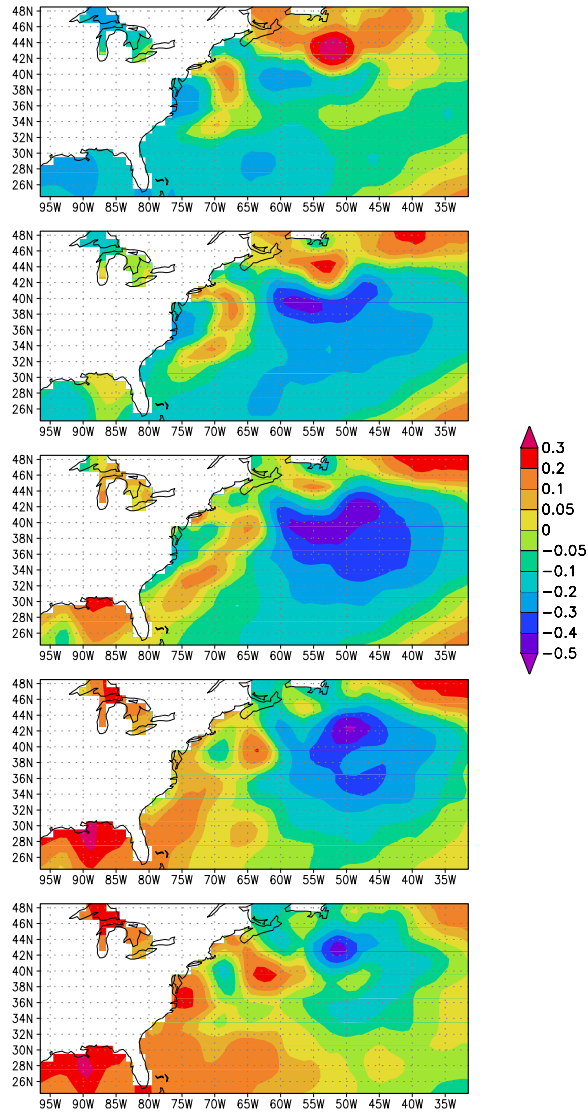


Figure 4.3: Reconstructed component (RC) pair 7-8 of Gulf Stream SST (K) describing the oscillating statistical mode having a 9-month timescale. The patterns are shown at a monthly interval, starting in October 1985, over one half-cycle of the oscillation; the other half-cycle is similar but with anomalies of reversed sign.

In Fig. 4.3 two SST anomalies of opposite sign are rotating in a counterclockwise fashion

in and just to the north of the mean axis of the Gulf Stream, whose latitudinal position increases from 39° to 44° *N* in the longitudinal band from 65° to 45° *W* (Auer, 1987). These anomalies are pinched off from another oscillation (in the region $30^\circ - 42^\circ$ *N*, $75^\circ - 65^\circ$ *W*), where two SST anomalies of opposite sign are rotating in a clockwise fashion. This is the region where the Gulf Stream has just separated from the North American continent. A third pair of opposite anomalies is rotating in a counterclockwise fashion in the Gulf of Mexico.

4.3.2 Spatiotemporal variability of T/P SSH observations

To investigate whether the 9-month periodicity found in the SST observations can also be found in another dataset, we have analyzed the T/P SSH dataset. Due to the removal of the seasonal cycle, the signature of the steric response to the seasonal heating cycle has been removed, leaving the signature of barotropic and baroclinic changes in ocean circulation (Kelly et al., 1999). As in the case of SST, the normalized nonseasonal SSH anomalies were first submitted to a standard PCA analysis and only the leading 22 PCs retained, which account for 91% of the variance. These PCs provide the L input channels for the M-SSA algorithm. We have 4 years of data, so $N = 144$. We have used a window length of 480 days ($M = 48$).

Again, first the Monte Carlo significance test for M-SSA has been applied. Because the test result depends on the values of the interpolation parameters (i.e., the decorrelation scales of the Gaussian interpolation), the result is shown for both the uninterpolated and interpolated datasets in Figs. 4.4a and b, respectively. In Fig. 4.4a, anomalous power against the red-noise hypothesis is observed in two different ST-PC pairs, associated with periods of 9 and 3 months, respectively. In the interpolated dataset the dominant timescale of 9 months belongs to ST-PC pair 5 – 6 (Fig. 4.4b), which explains 11% of the variance in the 22 leading PCs. This pair is, however, not significant at the 95% confidence level as a result of the smoothing process, which reduces the signal's amplitude to a large extent. The maximum amplitude of the 9-month statistical mode in the uninterpolated dataset is 31 cm, whereas the maximum amplitude of this mode in the interpolated dataset is only 5 cm. It turns out that ST-PC 5 and 6 are in quadrature as are the corresponding ST-EOF 5 and 6 (not shown), which suggests that the pair represents an oscillating statistical mode with a dominant period of 9 months. Also with the principal oscillation pattern (POP) analysis (Hasselmann, 1988; Von Storch et al., 1995), we found a similar oscillatory mode (with a period of 9 months and a decay time of 11 months) in the interpolated dataset and hence this statistical mode is quite robust in the data.

Fig. 4.5a represents the anomaly patterns of RC 5-6, computed from the interpolated T/P SSH dataset, for five phases during the oscillation. The starting time was chosen to be March 1995, when the amplitude of the statistical mode is quite large, and each subsequent picture is 1 month later; together the pictures show nearly half of the cycle of the oscillation. One can see in Fig. 4.5a that the anomalies are concentrated around the mean axes of the Gulf Stream, the North Atlantic Current, and the Azores Current. It is also evident that the anomalies are largest in the branching region. Moreover, there is an oscillation visible in the Gulf of Mexico. In Fig. 4.5b, we show the propagating SSH anomalies associated with this RC pair along 35° *N*. A series of positive and negative anomalies propagates westward, that is, upstream, with an average velocity of about 5 cm s^{-1} . The zonal wavelength associated with this RC pair is on the order of 12.5° , which corresponds to 1138 km at 35° *N*. In the T/P-ERS SSH dataset (section 5.2) a statistically significant RC pair has been found ($N = 158$, $M = 50$,

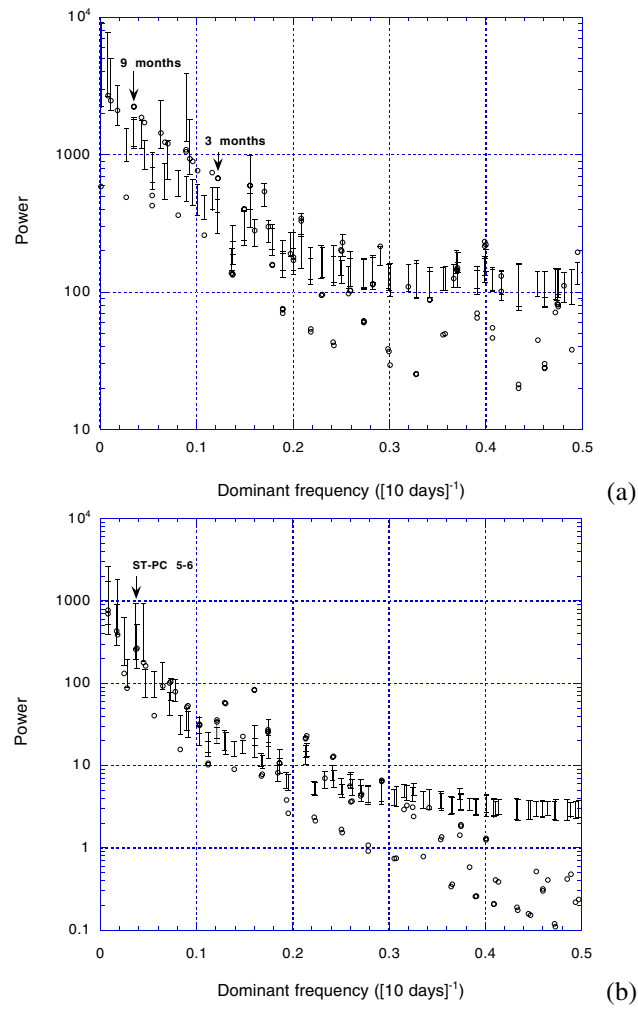


Figure 4.4: Monte Carlo significance test of (a) uninterpolated and (b) interpolated nonseasonal TOPEX/Poseidon SSH data in the Gulf Stream region for the period November 1992 - November 1996, using (a) $L = 41$ and (b) $L = 22$ PCs from a conventional PCA as the input channels. Shown are projections of the SSH data onto the data-adaptive basis, similar to that in Fig. 4.1b, with (a) $M = 50$ and (b) $M = 48$.

$L = 29$) with a similar timescale (8 months) and a similar spatial pattern (not shown) as RC 5-6 in the T/P SSH dataset. However, the spatial scales of the T/P-ERS anomalies are smaller than those of the T/P anomalies, which is probably a reflection of the ERS dataset's higher spatial resolution. This is not a trivial result as the two datasets overlapped only from April 1995 to November 1996 (sections 4.2 and 5.2), so that they are independent to a large extent.

Between 37° and 39° N, 65° and 60° W the New England Seamounts are situated and

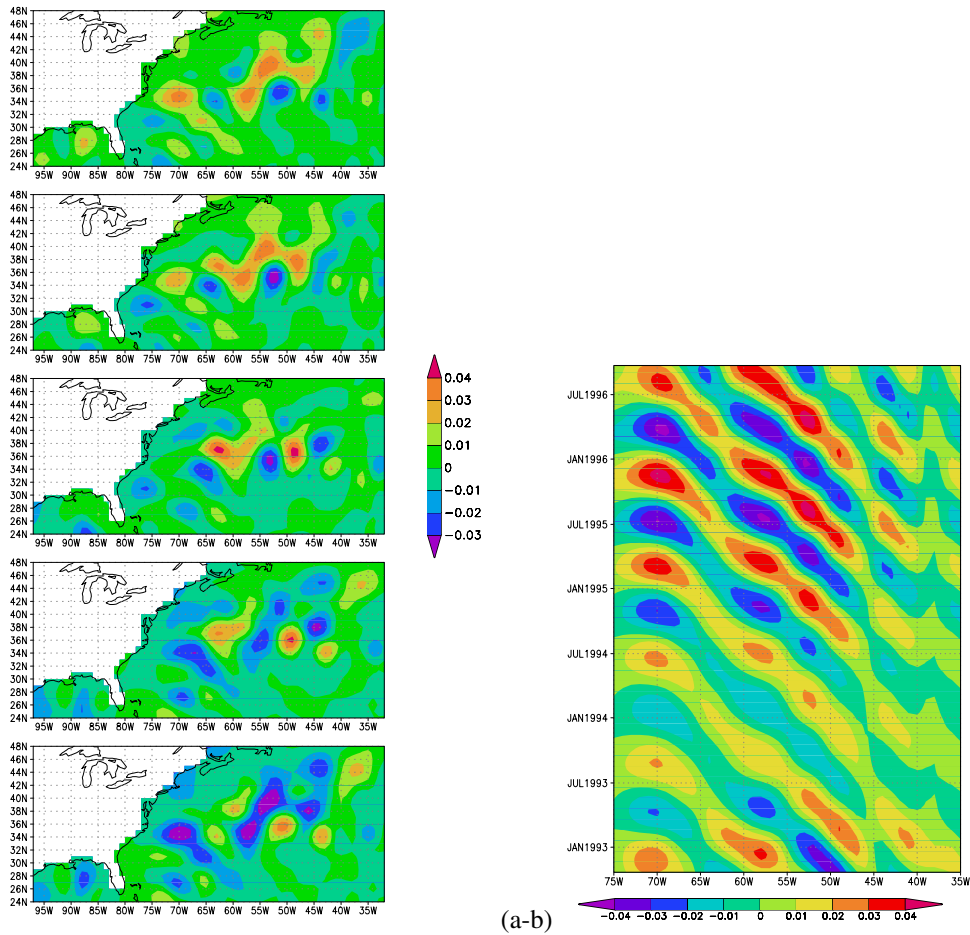


Figure 4.5: RC pair 5-6 of Gulf Stream SSH (m) describing the oscillating statistical mode having a 9-month timescale. (a) The patterns are shown at a monthly interval, starting in March 1995, over one half-cycle of the oscillation; the other half-cycle is similar but with anomalies of reversed sign. (b) The anomalies are shown along 35° N as a function of longitude and time.

there seems to be interaction of the mode with this bottom topographic feature. This is in accordance with Lee and Cornillon (1996), who found that the 9-month period meanders, which are relatively barotropic, are affected by the seamounts. Contrary to our result, however, they found a standing wave signature.

We can conclude that the spatial pattern of the reconstructed SSH anomalies of RC 5-6 (Fig. 4.5a) is quite different from the spatial pattern of the reconstructed SST anomalies (Fig. 4.3), although the frequencies are the same. This motivates one to study whether there is any variability in both fields that appears to be related.

4.3.3 Covarying patterns in SST and T/P SSH observations

To investigate whether the 9-month periodicities found in both SST and SSH are related, we investigated the coupled patterns of variability in both SST and SSH using the nonseasonal monthly mean datasets for the four years between November 1992 and November 1996 ($N = 48$). Now, M-SSA analysis is applied to the combined fields in order to find covarying propagating patterns in SST and SSH. To reduce the spatial dimensions, only the leading PCs of the separate PCA analyses, describing about 70% of the respective variances, are retained. These PCs, normalized by their singular values (in order that they contribute the same variance), provide the L input channels for the M-SSA algorithm. We have used a window length M of 16 months.

In this case the Monte Carlo significance test for M-SSA cannot be applied as the PCs of the two fields are not uncorrelated. The surrogate dataset would then be an L -channel multivariate AR(1) process, but it is inappropriate as a null hypothesis in a test for oscillatory behavior (Allen and Robertson, 1996) because it can itself support oscillations. It was found that the first four ST-EOFs correspond to variations with long, unresolved timescales. The fifth and sixth ST-EOFs, however, constitute a pair of eigenfunctions with similar eigenvalues and enhanced variance on a timescale of 8 months. This pair explains 13% of the variance in the leading PCs, and ST-PC 5 and 6 are in quadrature as are the corresponding ST-EOF 5 and 6, which suggests that the pair represents an oscillating statistical mode with a dominant period of 8 months. The patterns and propagation of the reconstructed SSH anomalies of RC 5-6 are very similar to the ones found using the individual dataset (Figs. 4.5a and 4.5b) and are therefore not shown. The SST anomaly pattern of RC 5-6 starts as a pattern very similar to the first EOF of SST, E1(SST) (Fig. 4.6a), and after one-quarter of a period the pattern is virtually E2(SST) (Fig. 4.6b). These patterns are different from the ones found using the individual dataset (Fig. 4.3), likely because of the use of a shorter time series.

This result contributes to the evidence of the existence of temporal variability with a dominant timescale of 8-9 months in the Gulf Stream area in accordance with earlier analyses (Lee and Cornillon, 1995; Kelly et al., 1996). The mechanism of this variability is not easily extracted from the patterns of the eigenvectors of the (separate) M-SSA analyses. The spatial patterns found in SST and SSH do not look much alike. SST anomalies of opposite sign are oscillating around each other in the areas where meandering intensity is largest (Auer, 1987). The SSH anomalies, which have smaller spatial scales than those of SST, are concentrated near the axes of the Gulf Stream, North Atlantic Current, and Azores Current and are propagating upstream. If one would look at only the patterns, it would not support any relationship between both fields. However, the combined M-SSA analysis suggests related physics causing the variability on this timescale in both fields. This is in accordance with Jones et al. (1998), who found that there is a relationship between SST and SSH anomalies in specific geographical regions associated with mesoscale variability. From the fact that these correlations are present at small and intermediate wavelengths, Jones et al. (1998) deduce that they are caused by large eddies, meanders, or Rossby waves rather than by the very large-scale seasonal response of the ocean to varying heat and water fluxes. In the next section, we investigate whether there is evidence of 9-month variability of the Gulf Stream in the POCM output.

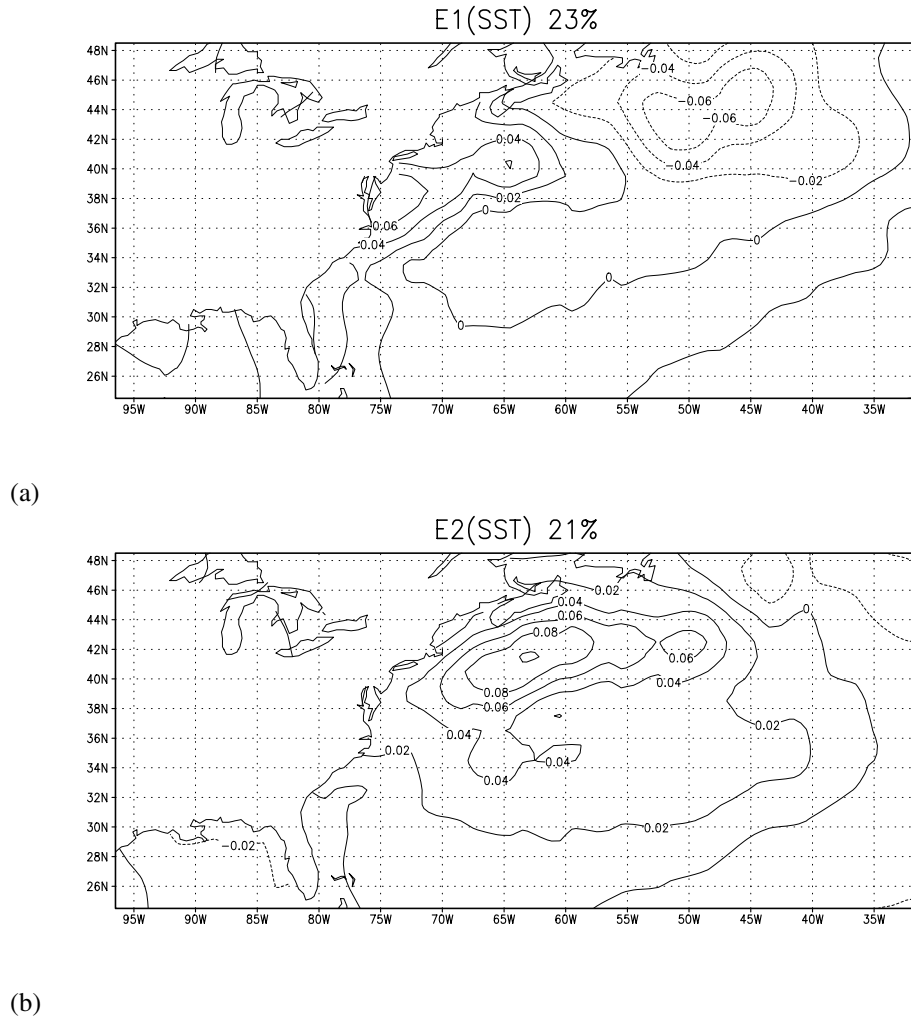


Figure 4.6: The first two EOFs of nonseasonal Gulf Stream SST, namely (a) $E1(SST)$ and (b) $E2(SST)$, based on data for the period November 1992 - November 1996. Negative contours are dashed. The fractions of variance of the data field explained by the respective PCs are indicated as well.

4.3.4 Spatiotemporal variability of POCM fields

To determine properties of the vertical structure of the 9-month mode, if present in POCM, we have analyzed simulated temperature fields at two depth levels, namely 310 m (T310) and 610 m (T610). In order to facilitate the comparison to the SST and SSH observations, we have also used the SST and SSH fields from POCM. For a general comparison between POCM output and T/P data, the reader is referred to Stammer et al. (1996). The analysis has been performed for each field separately. In all cases, the nonseasonal anomalies were

prefiltered with standard PCA and the leading PCs, which account for 80% of the variance, provide the L input channels for the M-SSA algorithm. We have obtained 19 years of model data, so $N = 228$, and use a standard window length M of 76 months.

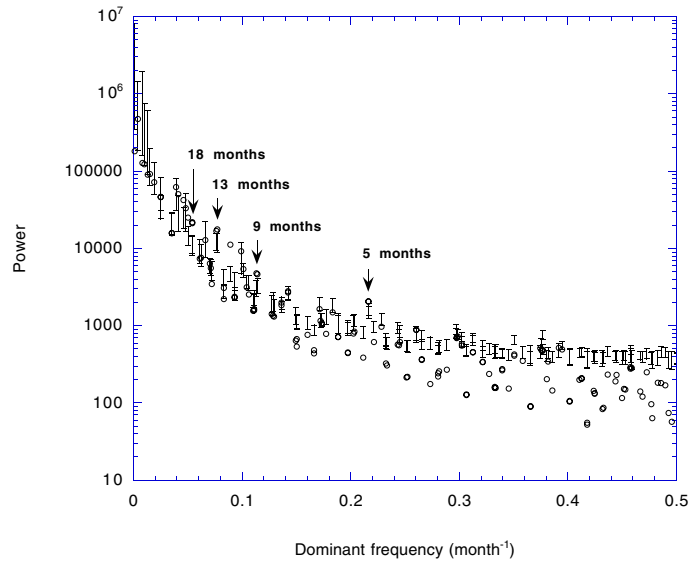


Figure 4.7: Monte Carlo significance test of nonseasonal POCM SSH data in the Gulf Stream region for the period 1979 - 1997, using $L = 21$ PCs from a conventional PCA as the input channels. Shown are projections of the SSH data onto the data-adaptive basis, similar to that in Fig. 4.1b, with a 76-month window ($M = 76$).

First, we show results from the M-SSA analysis of simulated SSH with $L = 21$. The result of the Monte Carlo significance test for M-SSA is shown for the data-adaptive basis in Fig. 4.7. Four data eigenvalue pairs, with associated periods of 18, 13, 9, and 5 months, are indicated as significant. The 9-month timescale belongs to a ST-PC pair that is in quadrature, which suggests that the pair represents an oscillating statistical mode.

The reconstructed anomaly patterns of SSH for this mode are shown in Fig. 4.8 for five phases during the oscillation. The starting time was chosen to be September 1980, when the amplitude of the statistical mode is quite large, and each subsequent picture is 1 month later; together the pictures show nearly half of the cycle of the oscillation. The anomalies are clearly present in the Gulf Stream region (Fig. 3.3) and have a maximum amplitude of 8 cm. As in the case of the 9-month statistical mode from the T/P altimeter data, the anomalies are concentrated around the mean axis of the Gulf Stream and they are propagating upstream. However, the spatial scales of the simulated SSH anomalies are smaller than the scales of the observed SSH anomalies, which may just be a reflection of the T/P dataset's lower spatial resolution capability (Greenslade et al., 1997). The wavelength associated with the RC pair of the simulated SSH anomalies is about 500 km. The 13-month statistical mode from POCM SSH displays a spatial pattern similar to this 9-month statistical mode.

Secondly, we show results from the M-SSA analyses of T310 ($L = 11$) and T610

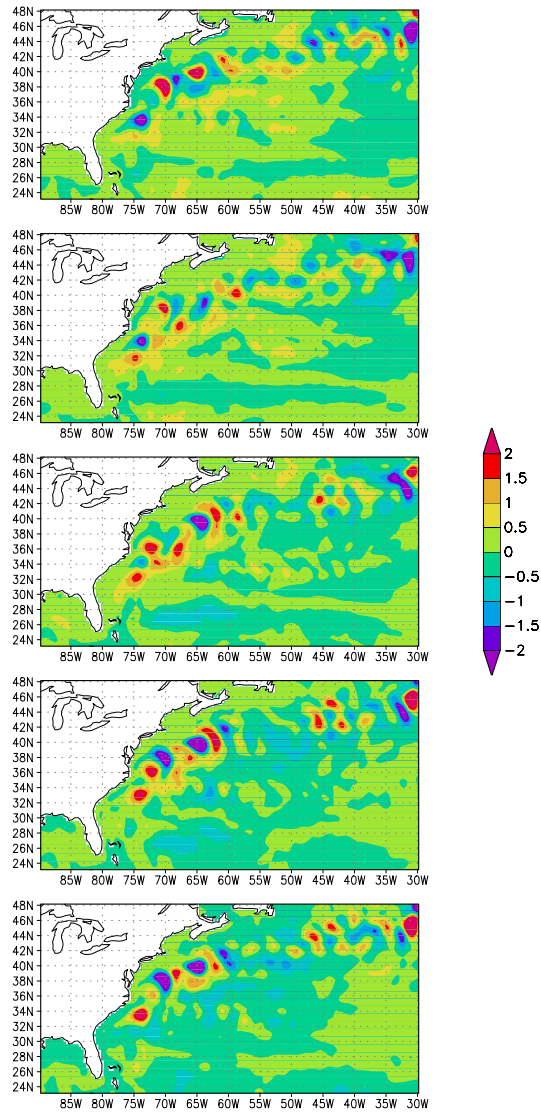
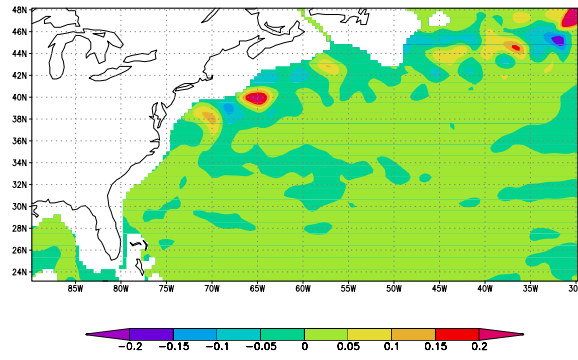


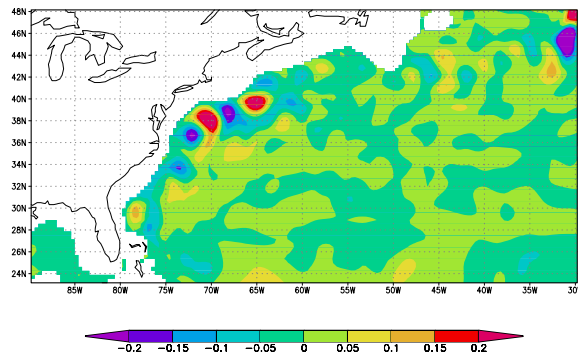
Figure 4.8: Reconstructed component of Gulf Stream SSH (cm) from POCM describing the oscillating statistical mode having a 9-month timescale. The patterns are shown at a monthly interval, starting in September 1980, over one half-cycle of the oscillation; the other half-cycle is similar but with anomalies of reversed sign.

($L = 20$). In both datasets, T310 and T610, there are statistically significant oscillating modes of variability with timescales of 20 and 13 months. Moreover, there is an oscillating

(a)



(b)



(c)

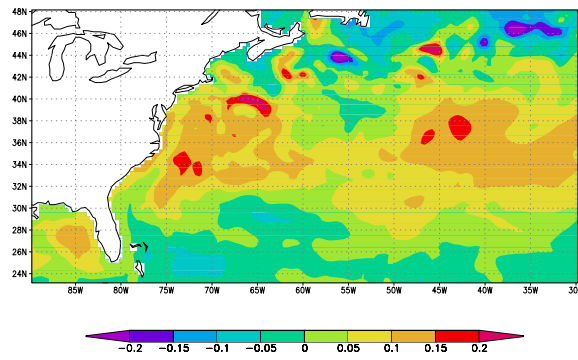


Figure 4.9: Snapshot of the reconstructed component of Gulf Stream (a) $T310$ (K), (b) $T610$ (K) and (c) SST (K) from POCM describing the statistical mode having a 9-month timescale; the patterns are shown for September 1980.

mode of variability with a timescale of 9 months present in both datasets, which is not statisti-

cally significant at the 95% confidence level. However, because the other analyses described above indicated the 9-month timescale as statistically significant, and we are interested in the vertical structure of the 9-month mode, we have computed the reconstructed anomaly patterns of T310 and T610 for this mode. The results are shown in Fig. 4.9a for T310 and in Fig. 4.9b for T610. The spatial patterns of T310 and T610 are very similar to the pattern of SSH (cf. upper panel of Fig. 4.8) and a comparison of Figs. 4.9a and 4.9b indicates that the structure of the 9-month mode is approximately equivalent barotropic. The spatial patterns of T310 and T610 for the 13 and 20-month statistical modes are very similar to the ones for the 9-month statistical mode. Indication of a 20-month timescale in observational data has been found by Speich et al. (1995) through spectral analysis of the Gulf Stream axis time series (their Fig. 18a). They derived this time series from the Comprehensive Ocean-Atmosphere Data Set (COADS) for the period 1970-92.

Finally, results are shown from the M-SSA analysis of simulated SST with $L = 25$. In this dataset there are also patterns of variability with timescales of 9 and 13 months present, which are, however, not statistically significant at the 95% confidence level. A snapshot of the reconstructed anomaly patterns of SST for the 9-month mode is shown in Fig. 4.9c. The anomalies are largest around the mean Gulf Stream axis and have a maximum amplitude of 0.7 K. A comparison of Fig. 4.9c and the upper panel of Fig. 4.8 indicates that the spatial patterns of SST and SSH for the 9-month mode are quite different, although there is a correspondence with regard to the positive anomaly at ($40^\circ N$, $65^\circ W$). The spatial pattern of the 13-month statistical mode in POCM SST (not shown) shows large-scale anomalies of opposite sign in the Gulf Stream separation region on the one hand and the extension region on the other hand. The Monte Carlo test of SST observations gives an indication of variability on a timescale of 14 months (see Fig. 4.1b), and the associated pattern of variability consists also of large spatial scales.

T (months)	SSH_P	T310_P	T610_P	SST_P	SST_O	SSH_O
9	*	*	*	*	*	*
13	*	*	*	*	*	
20		*	*		Speich et al. (1995)	

Table 4.3: Summary of common timescales T detected in the POCM output (P) and in the observations (O).

From the results of the M-SSA analyses described above, we can conclude that the connection between the spatial patterns of SST and SSH for the 9- and 13-month statistical modes is also unclear in the POCM output. In Table 4.3 the results of the M-SSA analyses of the POCM output and of the observations have been summarized. In the next section, we explore whether internal ocean dynamics may be the source of the 9-month variability in the Gulf Stream region.

4.4 Spatiotemporal variability within the barotropic shallow-water model

The shallow-water model is described in section 3.3, and the methods for dynamical systems analysis in Appendix B.2. The bifurcation diagram and the steady state solutions have already been shown in Fig. 3.7. In this section the oscillatory modes becoming unstable at the Hopf bifurcations are described. On the lower branch in Fig. 3.7a, a Hopf bifurcation occurs at $E = 2.5 \times 10^{-7}$ and is marked with H_1 . The steady state at this value of E is similar to Fig. 3.7b and therefore not shown. At H_1 the steady state becomes unstable to one oscillating dynamical mode. The pattern of this mode is determined from the eigenvector $\hat{\mathbf{x}} = \hat{\mathbf{x}}_R + i\hat{\mathbf{x}}_I$ associated with the eigenvalue $\sigma = \sigma_r + i\sigma_i$ in (B.10) (Appendix B.2). These span an oscillatory mode given by (1.1) with dimensional period $T = 2\pi r_0 / (U\sigma_i)$, i.e. 6 months for this mode. The perturbation is shown at four phases within half a period of the oscillation in Figs. 4.10a-d. The dynamical mode is located around the axis of the western boundary current and propagates northeastward, that is, downstream, instead of southwestward (upstream) which was stated in Schmeits and Dijkstra (2000). It has a wavelength of about 550 km. From Figs. 3.7b and 4.10a-d we can deduce that the perturbation adds cross-stream components to the flow in the western boundary current; that is, it causes the Gulf Stream to meander.

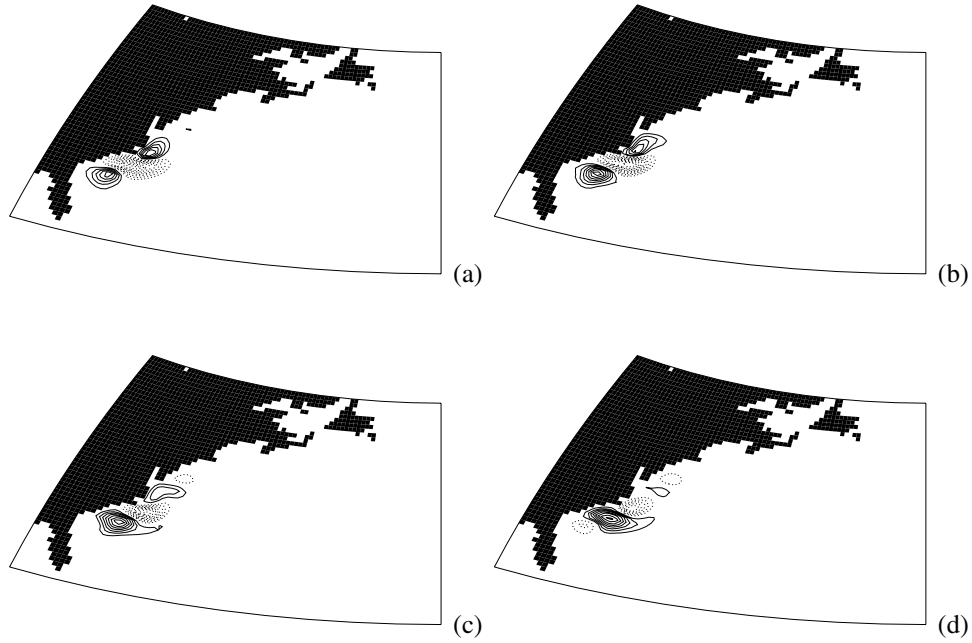


Figure 4.10: Contour plot of the layer thickness anomaly of the transition structure [(a)-(d)] of the neutral mode at the Hopf bifurcation H_1 in Figure 3.7a at several phases of the oscillation. (a) $\sigma_i t = -3\pi/4$; (b) $\sigma_i t = -\pi/2$; (c) $\sigma_i t = -\pi/4$; (d) $\sigma_i t = 0$.

To investigate the sensitivity of the results to the layer thickness D , we have computed a regime diagram separating steady from oscillatory behavior (Fig. 4.11a). At each value of D , the linear stability boundary is determined by the value of E at the Hopf bifurcation H_1 . It is obvious from Fig. 4.11a that the circulation gets more stable as D increases. This is a result of the fact that the same energy input by the windstress forcing is distributed over a deeper layer, which stabilizes the flow. The spatial pattern of the neutral mode does not change much with D , but the period of the oscillation increases from 6 to 11 months in the range of D considered (Fig. 4.11b). Of course, the average depth of the real Gulf Stream region depends on the domain chosen, but values slightly larger than 1 km do seem to be reasonable. Inclusion of bottom topography could change this mode and period substantially, but it has a large effect on the sea surface height in a barotropic model and hence it was not considered here.

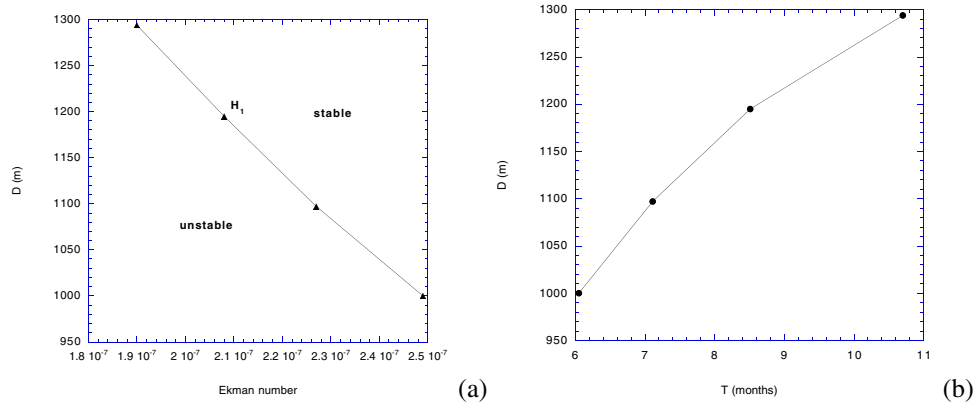


Figure 4.11: (a) Path of the first Hopf bifurcation H_1 (as in Fig. 3.7a), i.e. the linear stability boundary, in the (E, D) plane. (b) Oscillation period (T) of the neutral mode at H_1 as a function of the layer thickness D .

A second Hopf bifurcation (H_2) occurs at $E = 2.1 \times 10^{-7}$ on the branch of Gulf Stream solutions G_c^S and G_d^S (Fig. 3.7). The period of this oscillation is 2 months. The transition structure of the perturbation is shown in Figs. 4.12a-d, with the basic state being similar to that in Fig. 3.7c. Its maximum response is found in the high shear region to the southeast of Greenland, the propagation direction is westward and the perturbations have a typical wavelength of 500 km. The relevance of this dynamical mode to the variability in the northern part of the Atlantic basin is not further considered.

4.5 Discussion

As mentioned in the introduction, focus of this work was to find a plausible physical mechanism of the near-annual variability of the Gulf Stream. Both the M-SSA analyses of the individual fields of SST and T/P SSH observations clearly give a statistically significant mode

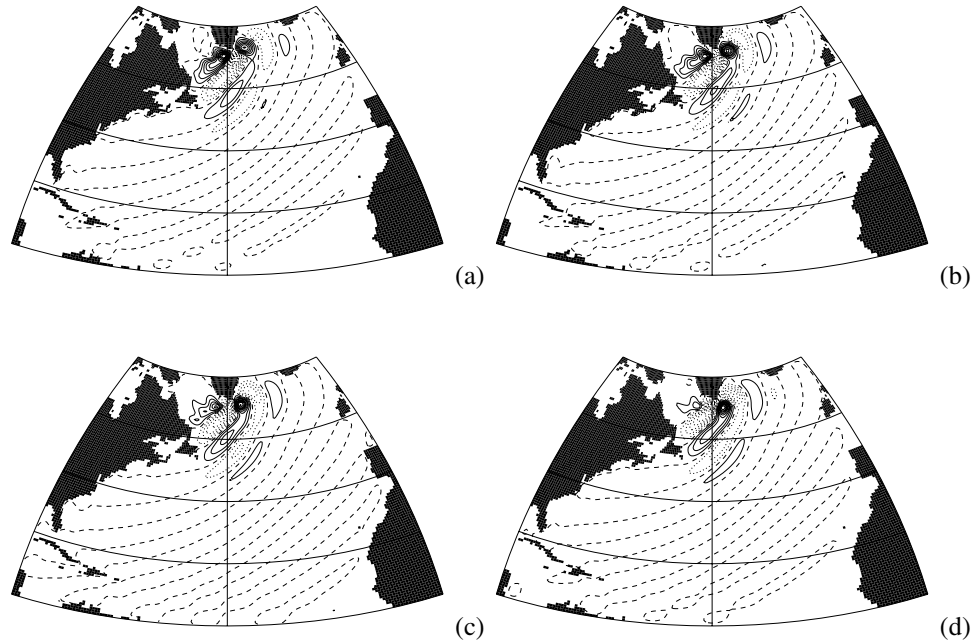


Figure 4.12: Contour plot of the layer thickness anomaly of the transition structure [(a)-(d)] of the neutral mode at the Hopf bifurcation H_2 in Figure 3.7a at several phases of the oscillation. (a) $\sigma_i t = -3\pi/4$; (b) $\sigma_i t = -\pi/2$; (c) $\sigma_i t = -\pi/4$; (d) $\sigma_i t = 0$.

of variability having a timescale of 9 months. This type of variability is very unlikely to be caused by red noise processes (Hasselmann, 1976). With the fact that this timescale of variability has also been found in other studies (Lee and Cornillon, 1995), we conclude that there is dominant variability on a 9-month timescale in the Gulf Stream region.

However, the patterns of both SST and SSH of this statistical mode have no direct correspondence. Large-scale SST anomalies are found over most of the basin with some hardly identifiable pattern of rotating anomalies in the Gulf Stream separation region. The SSH anomalies are of smaller scale, but they are present with comparable amplitude over the whole Gulf Stream region. Although the combined M-SSA analysis shows that the statistical modes of both SST and SSH on the intermonthly timescale may be related, the physical connection between both fields is not clear. This is partly due to the statistical techniques themselves because the statistically significant modes are not the patterns with highest variance and are therefore subjected to orthogonality constraints that may blur the connection between the pattern and the physics causing it.

M-SSA analysis of the POCM output also shows variability on a timescale of 9 months. Moreover, statistically significant modes with timescales of 13 and 20 months have been detected in the POCM output. Indication of a 14-month timescale has been found in the SST

observations (Fig. 4.1b) and a 20-month timescale has been detected by Speich et al. (1995) in the COADS dataset. The connection between SST and SSH for the 9- and 13-month statistical modes turned out to be unclear for both observations and POCM, as far as detected. As there is only a very weak restoring of POCM SST, the reason for this vague connection may be the same for both observations and POCM. In the future this connection may be studied in the framework of the shallow-water model by adding a surface mixed layer. Analysis of the POCM temperature fields at several vertical levels has indicated that the structure of the 9-, 13- and 20-month modes is approximately equivalent barotropic. Therefore, it seems legitimate to investigate the hypothesis of this paper, put forward in the introduction, in a barotropic model.

The shallow-water model used to study the transition to time dependence of wind-driven flows suffers from severe simplifications by being fully barotropic and discarding any effect of bottom topography. On the other hand, until now it is one of the most realistic models on which techniques of bifurcation analysis have been applied. As discussed in section 3.4.2, three mean flow patterns of the Gulf Stream are found of which the origin was discussed at length in Dijkstra and Molemaker (1999). These flows only differ with respect to their behavior along the North American coast, while being the same over the remainder of the basin.

The first oscillating dynamical mode to become unstable has a timescale on the order of months and is about 9 months for an average depth of the basin of 1200 m. Its perturbation pattern is localized in the recirculating cells, with very small amplitude over the remainder of the basin, and it causes the mean flow to meander. Its propagation direction is northeastward, i.e. downstream, which indicates that the mode is probably advected by the basic state flow. However, the zonal propagation direction of the mode itself should be westward, because the origin of this mode seems to be related to the ocean basin modes found in the 1.5-layer QG model (Dijkstra et al., 1999, subsection 1.3.3). Dijkstra and Molemaker (1999) have followed the latter modes through a hierarchy of 1.5-layer QG and SW models and found that the modes remained closely related. Therefore, the propagation mechanism of the oscillatory instability is similar to that of free Rossby waves, while the growth of the perturbation is related to the horizontal shear strength within the western boundary current (Dijkstra and Katsman, 1997). We will refer to this dynamical mode as the barotropic western boundary current (BWBC) mode below.

In the region of the Gulf Stream common features of the 9-month mode in POCM and the BWBC mode are that they both have a (near) barotropic structure, have similar timescales, and that the anomalies have wavelengths of about 500 km, and are concentrated around the mean axis of the Gulf Stream. Therefore, it is plausible that the 9-month mode in POCM (e.g., Fig. 4.8) is similar to the BWBC mode (Fig. 4.10). The connection with the observations is less obvious, as the spatial patterns of the SST and SSH modes do not correspond to the spatial pattern of the BWBC mode. They do, however, have a similar timescale of propagation. Besides, the anomalies of the SSH mode are also concentrated around the mean axis of the Gulf Stream, but they are present in the Gulf Stream Extension as well, whereas the BWBC mode is only present in the separation region. Therefore, it is impossible to claim that the physics of the BWBC mode is that causing the variability in the SST and SSH observations on that timescale. Instead, we claim something weaker, that is, that the BWBC mode contributes to the significance of the variability on this timescale, even if the dominant physics controlling

the variability would be caused by other processes (neglected in the SW model).

Other studies have strongly suggested that the 9-month variability is not related to variations in external forcing, such as the surface heat flux (Kelly et al., 1996) and that internal ocean dynamics is the most likely process to drive these changes in the flow field. The BWBC mode destabilizes the idealized Gulf Stream, which means that this perturbation pattern is able to extract energy out of the mean flow on this particular timescale. Hence, the energy level of this frequency can be easily increased due to the barotropic instability mechanism. Consequently, even if the physics of the variability is not caused by the BWBC mode, this mode may still contribute to its significance because it enhances the variance on this timescale in a totally different way as red noise processes would.

Suppose, on the other hand, that the underlying physics of this variability is indeed caused by the BWBC mode, then the question is why the statistical techniques do not find the pattern of this mode. That the spatial patterns of the dominant significant M-SSA modes in the SST and SSH observations and the BWBC mode in the SW model do not look alike may be explained by the property of M-SSA that it is able to discriminate between two oscillations with the same period only if they have spatially orthogonal patterns (Plaut and Vautard, 1994). Apart from the orthogonality constraints in the patterns as mentioned above, there are many processes contributing to the energy level on the particular timescale. Nonlinear interaction of baroclinic instabilities (which are modes of shorter timescale) can easily give a contribution on this timescale as can variations in atmospheric forcing. The statistical techniques, which are all in some way variance maximizing, pick up these signals and hence the resulting pattern on this timescale will show signatures not related to the main cause of the variability. If there were no clear non-red-noise-like source of energy at the particular frequency, as present here due to the BWBC mode, the pattern of the statistically determined patterns would likely not be significant. Hence, even though the significance is induced by the presence of the BWBC mode, the statistical technique would not be able to find its correct pattern.

With this argumentation, there is good reason to conjecture that the 9-month variability of the Gulf Stream is caused by a barotropic instability of the mean Gulf Stream path near its separation. Confirmation of this conjecture has been obtained through the connection between the 9-month mode from the POCM output and the BWBC mode in the SW model. This conjecture can be rejected if it turns out that stratification and other factors cause the BWBC mode, found here, to disappear.

Chapter 5

Physics of the 7-month variability in the Kuroshio region

5.1 Introduction

Like the Gulf Stream, the Kuroshio transports enormous amounts of heat northward, and not only its mean position, but also its variability is therefore important for the climate system. Similar to the 9-month variability in the Gulf Stream region (see chapter 4 and references therein), near-annual variability is also found in recent studies of the Kuroshio Extension. Wang et al. (1998) have used four years of data from the TOPEX/Poseidon (T/P) exact repeat mission (ERM) together with 2.3-yr data from the GEOSAT ERM. They have separated the low-frequency variability into intra-annual, annual and interannual variability through filtering processes, and here we concentrate on the results from the analysis of the intra-annual variability. Hövmöller diagrams (their Figs. 9 and 14) show that the intra-annual sea level height fluctuations are primarily propagating westward and they weaken away from the Kuroshio axis (at about $35^{\circ} N$). They have found that the dominant complex empirical orthogonal functions (CEOFs) have an average period of about 9 months, but the spatial structure differs between the CEOFs. The authors speculate that instability and/or external forcing might be responsible for the generation of the intra-annual variability. The authors conclude further that bottom topography plays a role in the generation of the intra-annual variability as well. Using both ECMWF atmospheric fields and GEOSAT data, Kelly et al. (1996) also found variability with timescales of 5-9 months in both the Gulf Stream and the Kuroshio. For both western boundary currents, they found correlations between surface transport and the path which suggest that there are structural changes in the recirculation gyres, associated with a path change. Although windstress (curl) is clearly correlated with surface transport, path and net surface heat flux in each ocean, there is no clear correlation between net surface heat flux and surface transport over the entire study region. They concluded that, at least in the North Atlantic, the structural changes in the recirculation gyres may not be related to surface heat flux variations.

In chapter 4 we have put forward the conjecture that the 9-month variability in the Gulf

Stream region is related to a barotropic instability of the wind-driven gyres. Because a close dynamical correspondence between the Kuroshio and the Gulf Stream is expected (e.g. chapter 3), we anticipate that the near-annual variability in the Kuroshio region may also be due to a barotropic instability of the wind-driven gyres. This hypothesis will be tested in this chapter following the same approach as in chapter 4. Again, the approach is along three paths: First, multivariate time series analysis techniques will be used to extract statistically significant modes of variability in T/P-ERS sea surface height (SSH) observations. Second, output from the Parallel Ocean Climate Model (POCM) (Semtner and Chervin, 1992; Stammer et al., 1996) is analyzed with the same statistical techniques giving information on the vertical structure of the variability. Finally, the instabilities of the barotropic North Pacific wind-driven circulation will be studied within a barotropic shallow-water model with realistic geometry and forcing. The datasets used in this study and their preprocessing are presented in section 5.2. The results of the data analysis and of the shallow-water model's bifurcation analysis are given in sections 5.3 and 5.4, respectively, with a discussion in section 5.5.

5.2 Datasets and their preprocessing

The datasets used in this study are maps of sea level anomalies from the combined TOPEX/Poseidon and ERS-2 missions (T/P-ERS) for the Kuroshio region ($25^\circ - 44^\circ N$, $120^\circ E - 170^\circ W$) and the POCM output for the Kuroshio region (section 3.2). The T/P-ERS dataset consists of interpolated altimeter data, that are corrected for all geophysical, media and instrument effects as well as for orbit error (ERS only). For more information on the data processing, the error estimation, and the gridding procedure the reader is referred to Le Traon et al. (1998). The T/P-ERS SSH anomalies have a spatial resolution of $0.25^\circ \times 0.25^\circ$ and a temporal resolution of 10 days. For the analysis of T/P-ERS SSH we use data from April 1995 - July 1999.

The seasonal cycle has been eliminated from the POCM output by computing anomalies about the 1979-98 monthly climatology. In this way, effects of the seasonal atmospheric forcing have been removed from the POCM output. Note that the seasonal cycle has not been eliminated from the T/P-ERS dataset. Besides, both datasets have been prefiltered with principal component analysis (PCA) (Preisendorfer, 1988) in order to reduce the number of spatial degrees of freedom in the datasets. Finally, the statistical mean at each point has been removed prior to the analysis. The multivariate data are then analyzed with the aid of multivariate time series analysis techniques described in Appendix A.

5.3 Results of the data analysis

5.3.1 Spatiotemporal variability of T/P-ERS SSH observations

The T/P-ERS SSH anomalies were prefiltered with standard PCA and the leading 24 PCs, which account for 76% of the variance, provide the L input channels for the M-SSA algorithm. We have more than 4 years of data ($N = 158$), and use a standard window length of 500 days ($M = 50$).

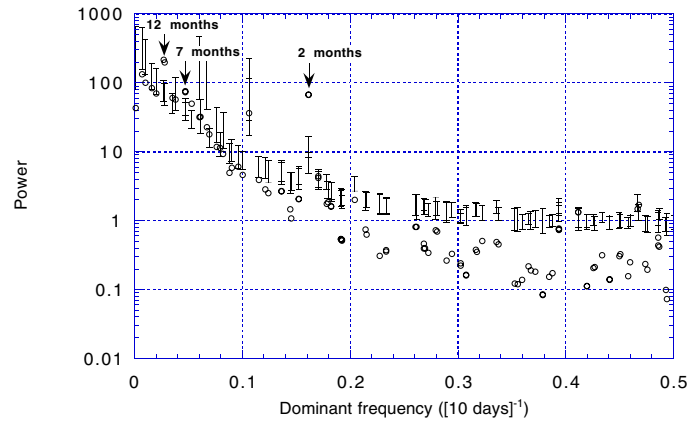


Figure 5.1: Monte Carlo significance test of T/P-ERS SSH data in the Kuroshio region for the period April 1995 - July 1999, using $L = 24$ PCs from a conventional PCA as the input channels. Shown are projections of the SSH data onto the data-adaptive basis, similar to that in Fig. 4.1b, with $M = 50$.

The result of the Monte Carlo significance test for M-SSA is shown for the data-adaptive basis in Fig. 5.1. Three data eigenvalue pairs, with associated periods of 12, 7, and 2 months, are indicated as significant. Because the seasonal cycle has not been removed from the T/P-ERS dataset (section 5.2), the signature of the steric response to the seasonal heating cycle shows up as the dominant ST-PC pair, explaining 26% of the variance in the 24 leading PCs. The 7-month timescale belongs to ST-PC pair 6-7 (Fig. 5.1), which explains 9% of the variance in the 24 leading PCs. ST-PC 6 and 7 are in quadrature, which suggests that the pair represents an oscillating statistical mode with a dominant period of 7 months. We have checked the robustness of this 7-month statistical mode with respect to a different value of the window length of 400 days ($M = 40$). For this value of M the 7-month timescale is also indicated as significant by the Monte Carlo test for M-SSA (not shown).

Fig. 5.2a represents the anomaly patterns of RC 6-7 for four phases during the oscillation. The starting time was chosen to be mid September 1997, when the amplitude of the statistical mode is quite large, and each subsequent picture is 1 month later; together the pictures show nearly half of the cycle of the oscillation. The anomalies are concentrated around the mean axis of the Kuroshio Extension (Fig. 5.2a) and their maximum amplitude is 31 cm. In Fig. 5.2b, we show the propagating SSH anomalies associated with this RC pair along $35^\circ N$. A series of positive and negative anomalies propagates westward, that is, upstream, with an average velocity of about 3 cm s^{-1} . The zonal wavelength associated with this RC pair is on the order of 6° , which corresponds to 546 km at $35^\circ N$. At $35^\circ N$ the continental rise is situated between about 140° and $143^\circ E$, and there seems to be interaction of the mode with this bottom topographic feature (Fig. 5.2b). No clear interaction is visible, however, with the other major bottom topographic features in the Kuroshio Extension region, namely the Shatsky Rise and Hess Rise. In the next section, we investigate whether there is evidence of 7-month variability of the Kuroshio in the POCM output.

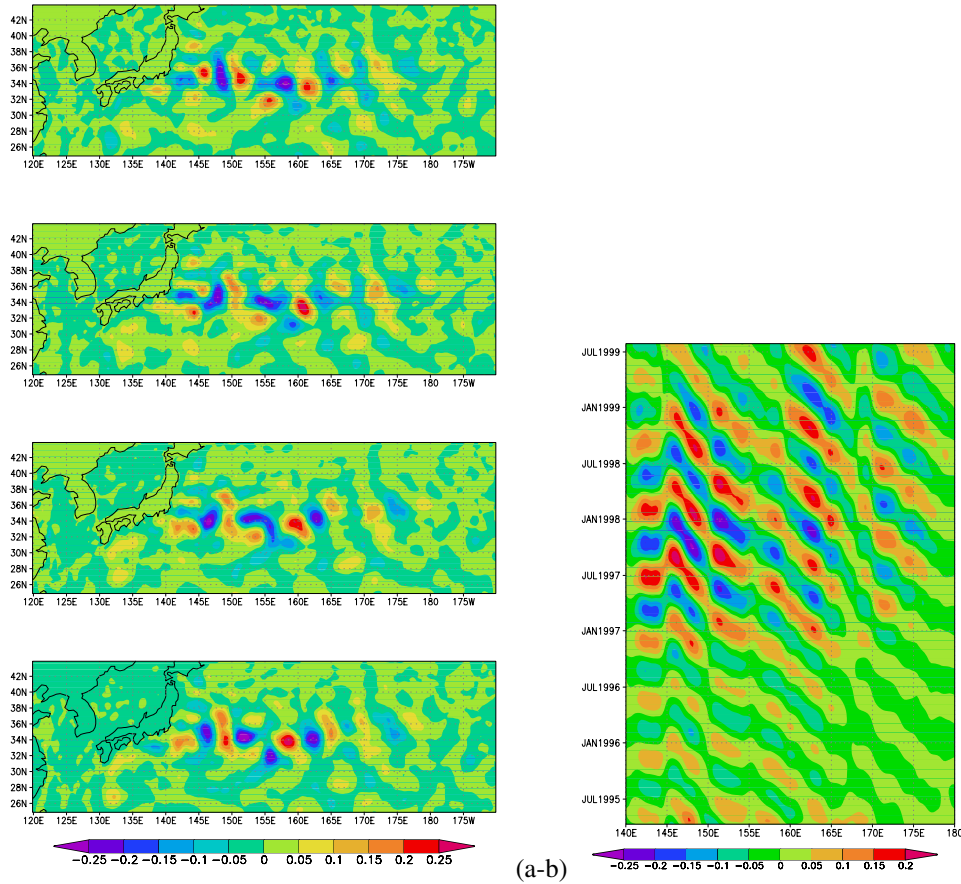


Figure 5.2: Reconstructed component (RC) pair 6-7 of Kuroshio SSH (m) describing the oscillating statistical mode having a 7-month timescale. (a) The patterns are shown at a monthly interval, starting in mid September 1997, over about one half-cycle of the oscillation; the other half-cycle is similar but with anomalies of reversed sign. (b) The anomalies are shown along 35° N as a function of longitude and time.

5.3.2 Spatiotemporal variability of POCM fields

To determine properties of the vertical structure of the 7-month mode, if present in POCM, we have analyzed simulated temperature fields at two depth levels, namely 160 m (T160) and 310 m (T310). The analysis has been performed for each field separately. In all cases described below, the nonseasonal anomalies were prefiltered with standard PCA and the leading PCs, which account for 70% or more of the variance, provide the L input channels for the M-SSA algorithm. We have obtained 20 years of data, so $N = 240$.

First, we report results from the M-SSA analyses of unfiltered T160 ($L = 17$) and T310 ($L = 14$) using a window length M of 80 months. In both datasets, T160 and T310, there is

an oscillating mode of variability with a timescale of 7 months, which is nearly statistically significant at the 95% confidence level. However, because the M-SSA analysis of T/P-ERS data indicated the 7-month timescale as statistically significant, and we are interested in the vertical structure of the 7-month mode, we are going to compute the reconstructed anomaly patterns of T160 and T310 for this mode after having filtered the datasets. As the eigenvalues corresponding to the 7-month mode in the unfiltered datasets have low rank-orders, we have filtered the nonseasonal T160 and T310 anomalies using a high-pass filter in order to remove timescales longer than 9 months. For the filtered datasets we have therefore used a window length M of 9 months.

Now, we show results from the M-SSA analyses of filtered T160 ($L = 38$) and T310 ($L = 35$). For each filtered dataset, the 7-month timescale belongs to ST-PC pair 3-4 that is in quadrature, which suggests that the pair represents an oscillating statistical mode. The reconstructed anomaly patterns of T160 and T310 for this mode are shown in Figs. 5.3 and 5.4, respectively, for four phases during the oscillation. The starting time was chosen to be January 1984, when the amplitude of the statistical mode is quite large, and each subsequent picture is 1 month later; together the pictures show nearly half of the cycle of the oscillation. The anomalies are rotating in the Kuroshio separation region (e.g. Fig. 3.1b), contrary to the anomalies associated with the 7-month statistical mode from the T/P-ERS altimeter data, which are also present in the Kuroshio Extension region (cf. Fig. 5.2a). However, there are also corresponding features: the anomalies of both statistical modes are concentrated around the mean axis of the Kuroshio and they have a wavelength in the same order of magnitude (around 500 km). The anomalies associated with the 7-month statistical mode from the POCM output have a maximum amplitude of 2.3 K and 2.2 K for T160 and T310, respectively. The spatial pattern of T160 is very similar to that of T310 and Figs. 5.3 and 5.4 indicate that the structure of the 7-month mode might be approximately equivalent barotropic. In the next section, we explore whether internal ocean dynamics may be the source of the 7-month variability in the Kuroshio region.

5.4 Spatiotemporal variability within the barotropic shallow-water model

The shallow-water model is described in section 3.3, and the methods for dynamical systems analysis in Appendix B.2. The bifurcation diagram and the steady state solutions have already been shown in Fig. 3.5. In this section the oscillatory modes becoming unstable at the Hopf bifurcations are described. On two branches in Fig. 3.5a, a Hopf bifurcation occurs at $E = 1.2 \times 10^{-7}$ and is marked with H_1 . The steady states at this value of E are similar to Figs. 3.5c and 3.5d and are therefore not shown. At H_1 the steady states become unstable to one oscillating dynamical mode. The pattern of this mode is determined from the eigenvector $\hat{\mathbf{x}} = \hat{\mathbf{x}}_R + i\hat{\mathbf{x}}_I$ associated with the eigenvalue $\sigma = \sigma_r + i\sigma_i$ in (B.10) (Appendix B.2). These span an oscillatory mode given by (1.1) with dimensional period $T = 2\pi r_0 / (U\sigma_i)$, i.e. 2 months for this mode. The perturbation is shown at four phases within half a period of the oscillation in Figs. 5.5a-d. Its maximum response is found in the high shear region to the south of Kamchatka, the propagation direction is eastward and the perturbations have a typical wavelength of 600 km. The relevance of this dynamical mode to the variability in the

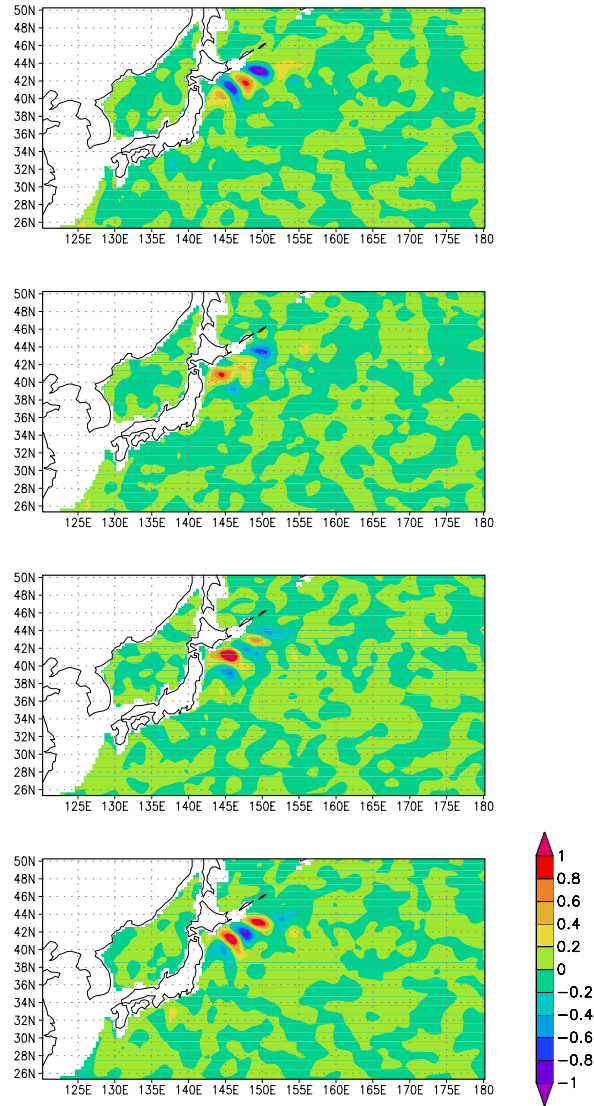


Figure 5.3: RC pair 3-4 of high-pass filtered Kuroshio T160 (K) from POCM describing the oscillating statistical mode having a 7-month timescale. The patterns are shown at a monthly interval, starting in January 1984, over one half-cycle of the oscillation; the other half-cycle is similar but with anomalies of reversed sign.

northwestern part of the Pacific basin is not further considered.

A second Hopf bifurcation (H_2) occurs at $E = 1.2 \times 10^{-7}$ on the upper branch in Fig.

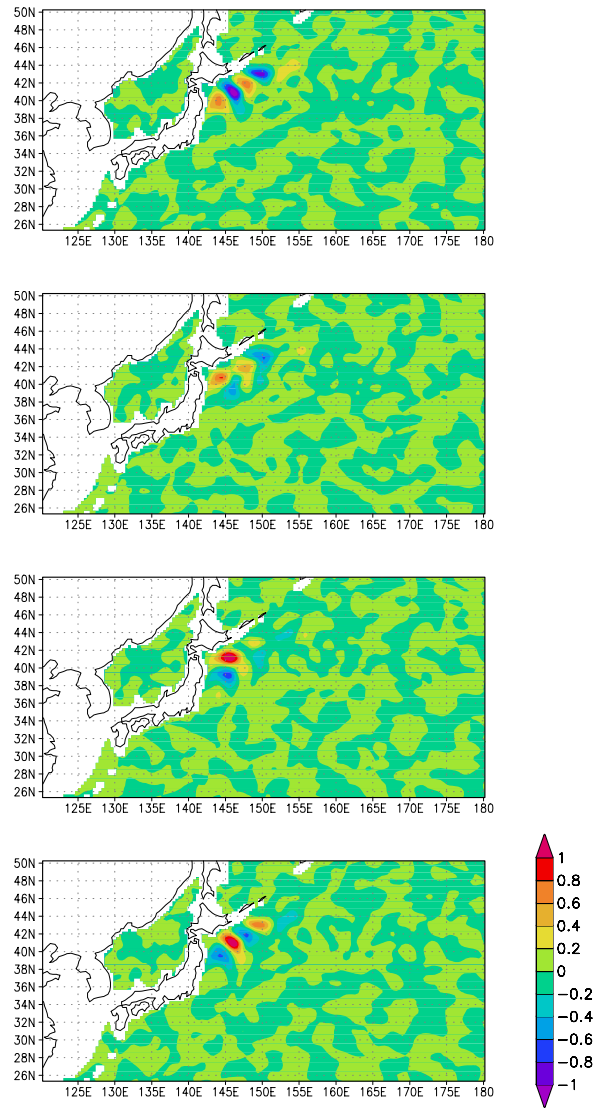


Figure 5.4: As Fig. 5.3, but for RC pair 3-4 of high-pass filtered Kuroshio T310 (K) from POCM.

3.5a. The transition structure of the perturbation is shown in Figs. 5.6a-d. The dynamical mode is located in the separation region of the Kuroshio and propagates eastward. It has a period of 3 months, and a wavelength of about 550 km. The timescale of this mode turns out to be insensitive to the layer thickness D , at least for values of D up to 1196 m.

Another oscillatory mode, which is also located in the separation region of the Kuroshio,

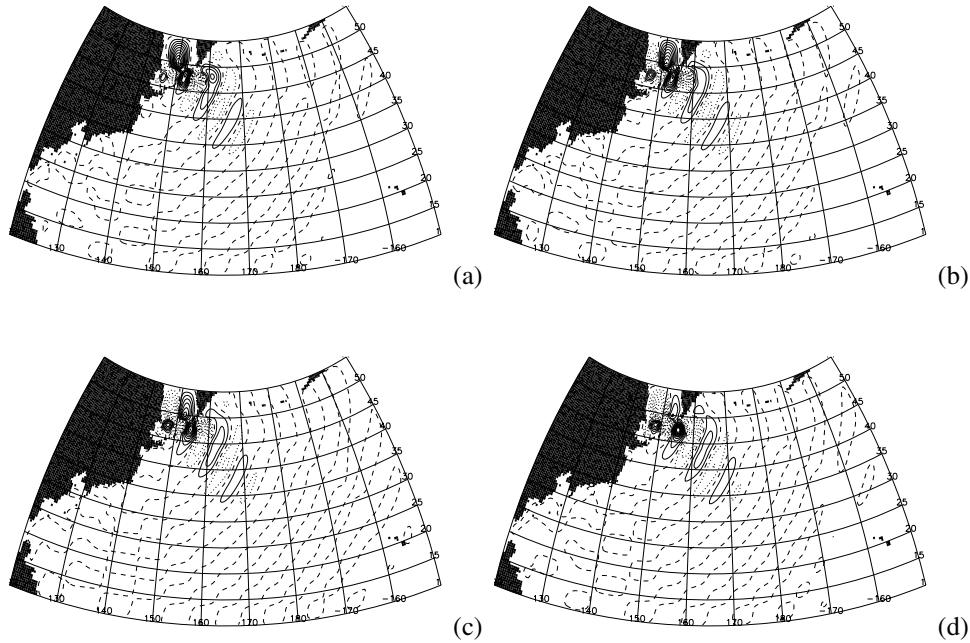


Figure 5.5: Contour plot of the layer thickness anomaly of the transition structure [(a)-(d)] of the neutral mode at the Hopf bifurcation H_1 in Figure 3.5a at several phases of the oscillation. (a) $\sigma_i t = 0$; (b) $\sigma_i t = \pi/4$; (c) $\sigma_i t = \pi/2$; (d) $\sigma_i t = 3\pi/4$.

has been found on the upper branch in Fig. 3.5a, but it is stable for the standard value of D . The period of this oscillation is about 5 months. We have investigated the sensitivity of this mode to the layer thickness D . It turns out that for slightly larger values of D , the mode becomes unstable, and we denote the associated Hopf bifurcation by H_3 . For $D = 1044$ m the Hopf bifurcation H_3 occurs at $E = 1.1 \times 10^{-7}$. The transition structure of the perturbation is shown in Figs. 5.7a-d, with the basic state being similar to that in Fig. 3.5c. The dynamical mode has a period of about 6 months, it propagates westward, that is, upstream and the perturbations have a typical wavelength of 450 km. From Figs. 3.5c and 5.7a-d we can deduce that the perturbation causes the southern recirculation gyre either to stretch or contract during one period of the oscillation.

For several values of D , the value of E is determined at which the Hopf bifurcation H_3 occurs (Fig. 5.8a). The spatial pattern of the neutral mode does not change much with D , but the period of the oscillation increases from 6 to 8 months in the range of D considered (Fig. 5.8b). Of course, the average depth of the real Kuroshio separation region is much larger, but the wind does not influence the circulation in the deeper ocean. Therefore, values slightly larger than 1 km do seem to be reasonable. Inclusion of bottom topography could change this mode and period substantially, but it has a large effect on the sea surface height

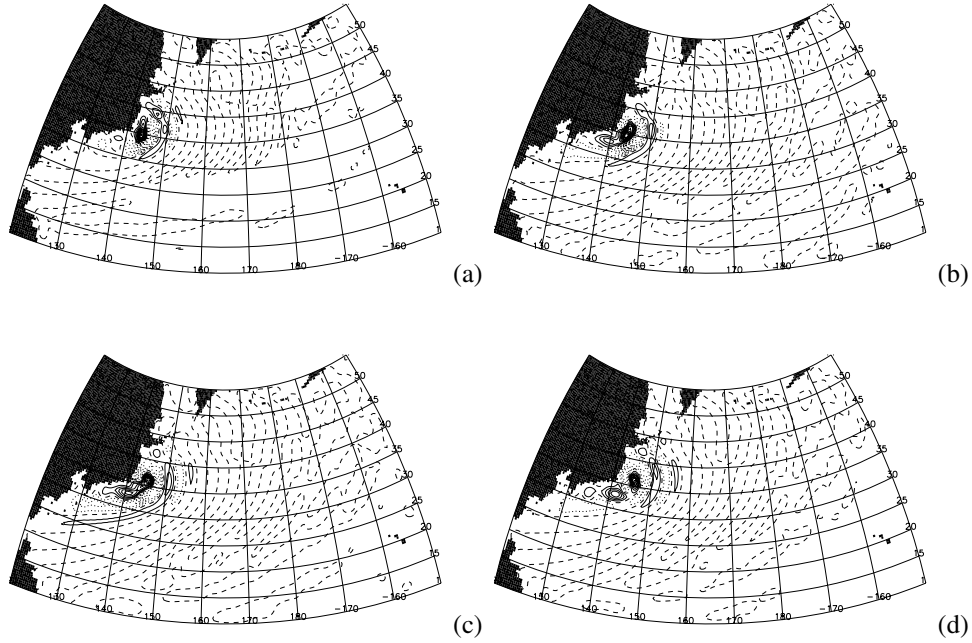


Figure 5.6: Contour plot of the layer thickness anomaly of the transition structure [(a)-(d)] of the neutral mode at the Hopf bifurcation H_2 in Figure 3.5a at several phases of the oscillation. (a) $\sigma_i t = 0$; (b) $\sigma_i t = \pi/4$; (c) $\sigma_i t = \pi/2$; (d) $\sigma_i t = 3\pi/4$.

in a barotropic model and hence it was not considered here.

5.5 Discussion

As mentioned in the introduction, focus of this work was to study whether the near-annual variability in the Kuroshio region may also be due to a barotropic instability of the wind-driven gyres, as was conjectured for the Gulf Stream (chapter 4). M-SSA analysis of T/P-ERS SSH observations clearly gives a statistically significant mode of variability having a timescale of 7 months. The anomalies are concentrated around the mean axis of the Kuroshio Extension (Fig. 5.2a) and they are propagating westward, that is, upstream (Fig. 5.2b). These features of the near-annual variability in the Kuroshio region are in correspondence with the study of Wang et al. (1998), although they found a somewhat longer timescale (9 months). With the fact that a similar timescale of variability (5-9 months) has also been found in another study (Kelly et al., 1996), we conclude that there is dominant variability on a 7-month timescale in the Kuroshio region.

M-SSA analysis of the POCM output also shows variability on a timescale of 7 months. Contrary to the observations, the anomalies associated with the 7-month statistical mode from

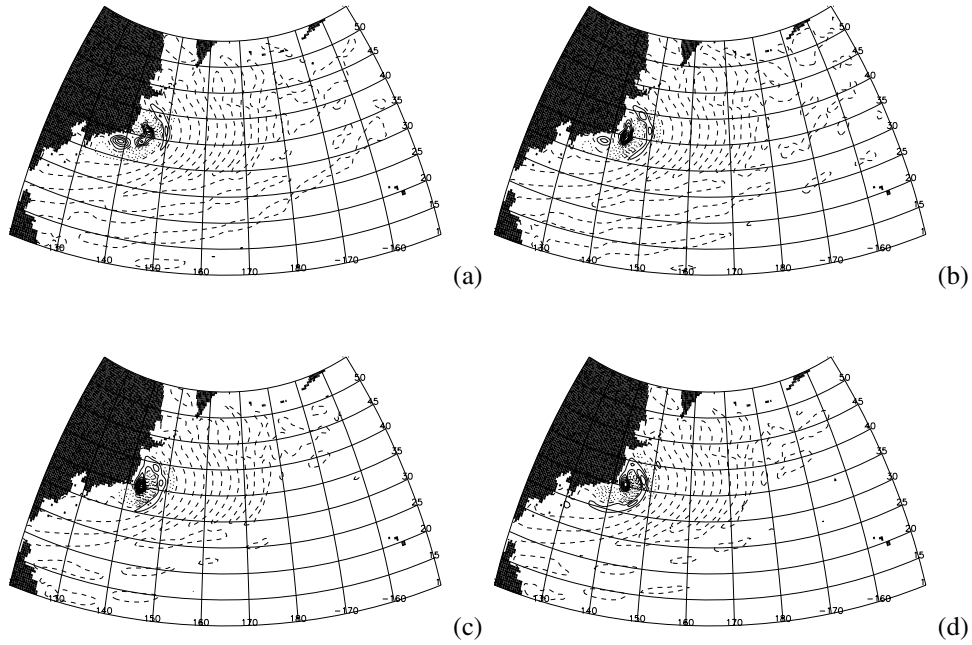


Figure 5.7: Contour plot of the layer thickness anomaly of the transition structure [(a)-(d)] of the neutral mode at the Hopf bifurcation H_3 for $D = 1044$ m (see also Fig.5.8a) at several phases of the oscillation. (a) $\sigma_i t = 0$; (b) $\sigma_i t = \pi/4$; (c) $\sigma_i t = \pi/2$; (d) $\sigma_i t = 3\pi/4$.

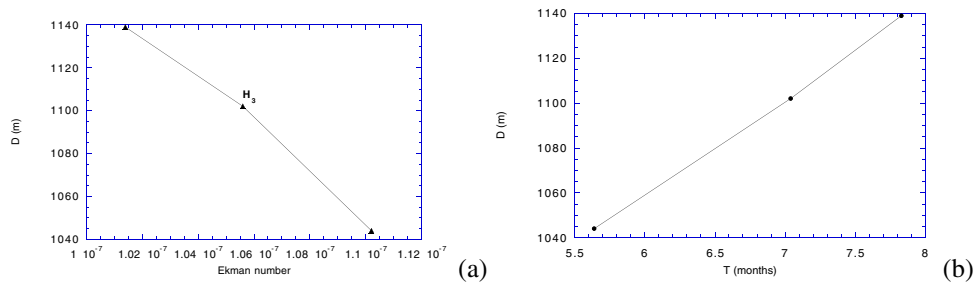


Figure 5.8: (a) Path of the Hopf bifurcation H_3 (see text) in the (E, D) plane. (b) Oscillation period (T) of the neutral mode at H_3 as a function of the layer thickness D .

the POCM output are concentrated in the Kuroshio separation region. However, there are also corresponding features: the anomalies of both statistical modes are concentrated around the mean axis of the Kuroshio and they have a wavelength in the same order of magnitude (between 400 and 500 km). Analysis of the POCM temperature fields at several vertical levels

(Figs. 5.3 and 5.4) has indicated that the structure of the 7-month mode might be approximately equivalent barotropic. Therefore, it seems legitimate to investigate the hypothesis of this paper, put forward in the introduction, in a barotropic shallow-water model, which is used to study the transition to time dependence of wind-driven flows.

As discussed in section 3.4.1, three mean flow patterns of the Kuroshio are found of which the origin was discussed at length in Dijkstra and Molemaker (1999). These flows only differ with respect to their meandering behavior near the southern coast of Japan, while being the same over the remainder of the basin.

One of the oscillating dynamical modes to become unstable has a timescale on the order of months and is about 7 months for an average depth of the basin of 1100 m (Fig. 5.8b). Its perturbation pattern is localized in the separation region of the Kuroshio, with very small amplitude over the remainder of the basin (Fig. 5.7), and it causes the southern recirculation gyre either to stretch or contract during one period of the oscillation. The origin of this mode seems to be related again to the ocean basin modes found in the 1.5-layer QG model (Dijkstra et al., 1999, subsection 1.3.3). As in section 4.5, we will refer to this dynamical mode as the barotropic western boundary current (BWBC) mode.

In the region of the Kuroshio common features of the 7-month mode in POCM and the BWBC mode are that they both have a (near) barotropic structure, have similar timescales, and that the anomalies have wavelengths of about 400 km, and are concentrated in the separation region of the Kuroshio. Therefore, it is plausible that the 7-month mode in POCM (e.g., Fig. 5.3) is similar to the BWBC mode (Fig. 5.7). The connection of the BWBC mode with the 7-month mode in the SSH observations (Fig. 5.2a) is also reasonable. They have a similar timescale of propagation and similar spatial scales as well. Besides, the anomalies of the 7-month SSH mode are also propagating westward, and have large amplitudes in the separation region of the Kuroshio. However, the 7-month SSH mode is also present in the Kuroshio Extension, whereas the BWBC mode is only present in the separation region. Despite this discrepancy, which has been extensively discussed in chapter 4, it is conjectured that the physics of the BWBC mode is that causing the variability in the SSH observations on the 7-month timescale. This is supported by the corresponding effect of both modes: the observational study of Kelly et al. (1996) has suggested that the dominant mode of variability in the North Pacific (as well as the North Atlantic) is a contraction and expansion of the recirculation gyres, which is associated with a large-scale path change, with timescales of 5-9 months.

To conclude: the conjecture from chapter 4 and from this chapter, i.e. that the near-annual variability of the Kuroshio (Gulf Stream) is caused by a barotropic instability of the mean Kuroshio (Gulf Stream) path near its separation, is supported by:

- the corresponding features of the near-annual statistical mode from the SSH observations, from the POCM output and the BWBC mode in the barotropic SW model for each current separately
- the expected close dynamical correspondence between the Kuroshio and the Gulf Stream
- the connection between the separate modes (from either the observations, the POCM output or the SW model) of both currents

- the correspondence in timescales between the statistical modes of both currents despite the difference in size of the North Atlantic and North Pacific basins.

Chapter 6

The influence of additive stochastic forcing on the variability in the barotropic shallow-water model

6.1 Introduction

In chapter 2 we have studied the connection between multivariate time series analysis and bifurcation analysis for the 2-layer QG model. It turned out that the dominant M-SSA modes (or POPs) could all be linked to neutral modes at Hopf bifurcations in either the 2-layer or 1.5-layer QG model. In this chapter the same connection will be studied, but now in the framework of the barotropic shallow-water model with and without additive stochastic forcing.

In section 3.5 we have seen that noise-induced transitions between multiple steady states occur in the barotropic shallow-water model for the North Atlantic basin. This indicates that the signatures of the multiple (unstable) steady states can still be found in the presence of additive stochastic forcing. One of the questions, we like to address in this chapter, is whether also the oscillatory modes that become unstable at the Hopf bifurcations (see sections 4.4 and 5.4) can still be found in the presence of additive stochastic forcing.

In this study we will investigate the effect of an additive stochastic forcing in a nonlinear flow regime contrary to Willebrand et al. (1980) who investigated the response to stochastic forcing in a linear flow regime. Specifically, Willebrand et al. (1980) have investigated the response of a barotropic SW model to stochastic windstress forcing only (i.e. zero mean) as computed from twice-daily weather maps for the period 1973-76. Their model geometry consisted of a rectangular basin of constant depth and with realistic dimensions. The horizontal resolution was 1° in longitude and 0.7° in latitude. They have used a value of $5 \times 10^3 \text{ m}^2\text{s}^{-1}$ for the lateral friction coefficient A_H , which corresponds to $E = 8.4 \times 10^{-7}$. The Rossby number is very small in their model and nonlinearities are therefore unimportant. It is shown that three distinct frequency bands characterize the wind-induced barotropic fluctuations:

- At periods between 10 and 30 days the response is primarily in the form of planetary Rossby waves so that westward phase propagation is prominent. Spectral peaks occur only at a few discrete frequencies and are caused by resonant basin modes.
- At periods between 1 and 10 days the response is no longer wavelike but is locally forced and the energy density increases steeply with decreasing frequency.
- At periods longer than a month there is a time-dependent quasi-Sverdrup balance and the frequency spectra are more or less white.

First, we will perform M-SSA (Appendix A.1) on output from the barotropic shallow-water model for the North Atlantic using both steady forcing and additive stochastic forcing (subsection 6.2.1). Second, we will do the same analysis for the North Pacific basin (subsection 6.2.2). Subject of study is again whether the dominant (and/or statistically significant) M-SSA modes can be linked to neutral modes at the Hopf bifurcations in the respective bifurcation diagrams.

6.2 Multivariate time series analysis of the barotropic SW model with(out) noise

In this section, M-SSA is performed on the transient flows computed with the barotropic SW model (see section 3.3). The time-dependent behavior of the SW model, forced with both steady (Fig. 3.4) and noisy wind forcing (subsection 3.5.1), is studied using implicit time integration (Appendix B.2). In all time integrations, described below, the SW model has been run with the standard set of parameters (Table 3.1) apart from the value of the Ekman number. In all cases described below, the SSH anomalies were prefiltered with standard PCA and the leading PCs, which account for 81% or more of the variance, provide the L input channels for the M-SSA algorithm. The sampling time (which is much larger than the time step) is 0.04 y, unless otherwise stated. Besides, the sample size N and the value of the window length M are given in each case.

6.2.1 North Atlantic

The bifurcation diagram (Fig. 3.7a) for the North Atlantic indicates the position of two Hopf bifurcation points and the neutral modes becoming unstable at these points have been described in section 4.4. For $E = 1.6 \times 10^{-7}$, which is a value smaller than the values at which the Hopf bifurcations occur (Fig. 3.7a), two trajectories were computed. As initial condition the unstable steady solution G_b^S (Fig. 3.7b) indicated by the point b in Fig. 3.7a was chosen which has been slightly perturbed into the direction of the most unstable mode in the case of the steady wind forcing.

For the first trajectory, the flow is forced by the steady wind forcing and values of the maximum northward transport have been shown in Fig. 3.10a. After an initial transient period, eventually the trajectory is attracted towards a stable limit cycle with a period of about two months, coming from the second Hopf bifurcation in Fig. 3.7a. This is confirmed by performing M-SSA on the last 2 years of this trajectory ($N = 52$, $M = 15$, $L = 4$). The

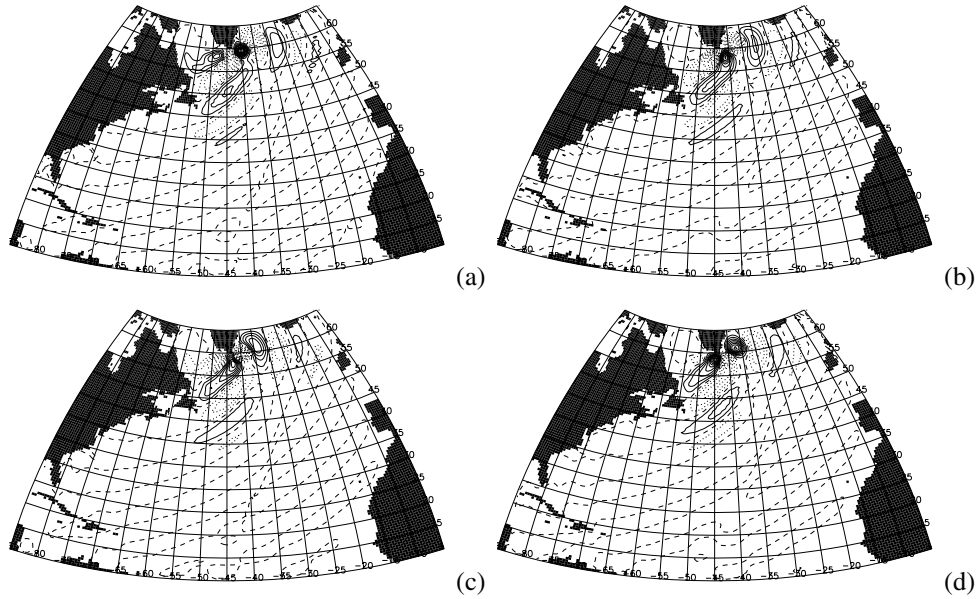


Figure 6.1: Reconstructed component (RC) pair 1-2 of SSH anomalies at several phases of the oscillation. (a) $t = 0$; (b) $t = \pi/2$; (c) $t = \pi$; (d) $t = 3\pi/2$. Contours are with respect to the absolute maximum of RC 1-2. The SSH anomalies are computed from the last 2 years of the 6-year time integration of the barotropic SW model on the North Atlantic domain with the steady windstress of Fig. 3.4b as forcing and $E = 1.6 \times 10^{-7}$.

dominant RC pair, that explains 99% of the variance, is shown in Fig. 6.1 for four phases during the oscillation. It can be clearly linked to the neutral mode at H_2 (cf. Fig. 4.12) and the oscillation period of 2 months is the same as that of the neutral mode at H_2 . The mean SSH pattern associated with the stable limit cycle has been shown in Fig. 3.10b; it is very similar to state G_c^P in POCM (cf. Fig. 3.3c).

For the second trajectory, the stochastic forcing is added to the steady forcing and values of R_i (as in (3.7)) have been shown in Fig. 3.11a (the correspondence between the value of i and the steady states is indicated in the figure caption). The trajectory stays more or less close to the unstable steady solution from which it started (G_b^S ; indicated by point b in Fig. 3.7a) during the first five years of the integration, but it is attracted towards one of the other unstable steady solutions (G_c^S ; indicated by point c in Fig. 3.7a) in the last part of the integration.

As the stochastic forcing can be approximated as white on timescales longer than a month (subsection 3.5.1), red noise can be expected to be a good null hypothesis for the response of the model ocean and therefore the Monte Carlo significance test for M-SSA has been applied again ($N = 150$, $M = 50$, $L = 17$). The result is shown in Fig. 6.2 and red noise indeed turns out to be a good null hypothesis on timescales longer than 1.5 months. Four data eigenvalue pairs, with associated periods between 2 and 3 months, are indicated as significant. The dominant RC pair explains 10% of the variance, it has a timescale of 2 months and is

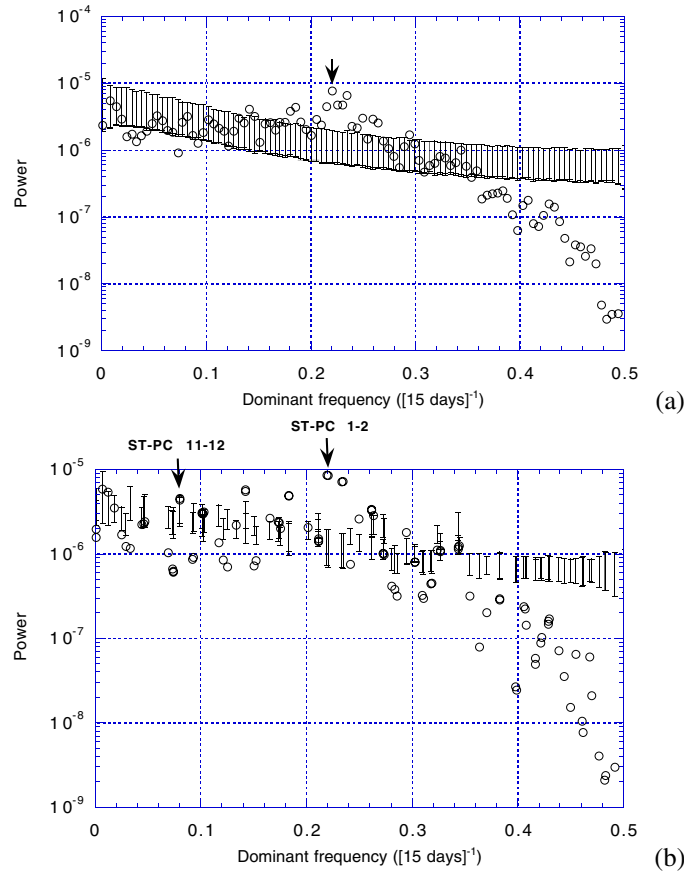


Figure 6.2: Monte Carlo significance test of 15-daily SSH anomalies, using $L = 17$ PCs from a conventional PCA as the input channels. The SSH anomalies are computed from the 6-year time integration of the barotropic SW model on the North Atlantic domain with the stochastic forcing added to the steady forcing and $E = 1.6 \times 10^{-7}$. Shown are projections of the SSH anomalies onto (a) the AR(1) null-hypothesis basis and (b) the data-adaptive basis, with a 2-year window ($M = 50$). Open circles show the data eigenvalues, plotted against the dominant frequency of the corresponding ST-PC. The vertical bars show the 95% confidence interval computed from 1000 realizations of a noise model consisting of L independent AR(1) processes with the same variance and lag-1 autocorrelation as the input data channels.

shown in Fig. 6.3 for four phases during the oscillation. The patterns can be clearly linked to the neutral mode at H_2 (cf. Fig. 4.12) again, which indicates that both the second Hopf bifurcation and the associated limit cycle "survive" the addition of stochastic forcing to the system. The other three significant RC pairs cannot be linked to oscillatory instabilities that are known from the linear stability analysis and are therefore not shown. Some of these modes may be stable in the deterministic system and excited by noise.

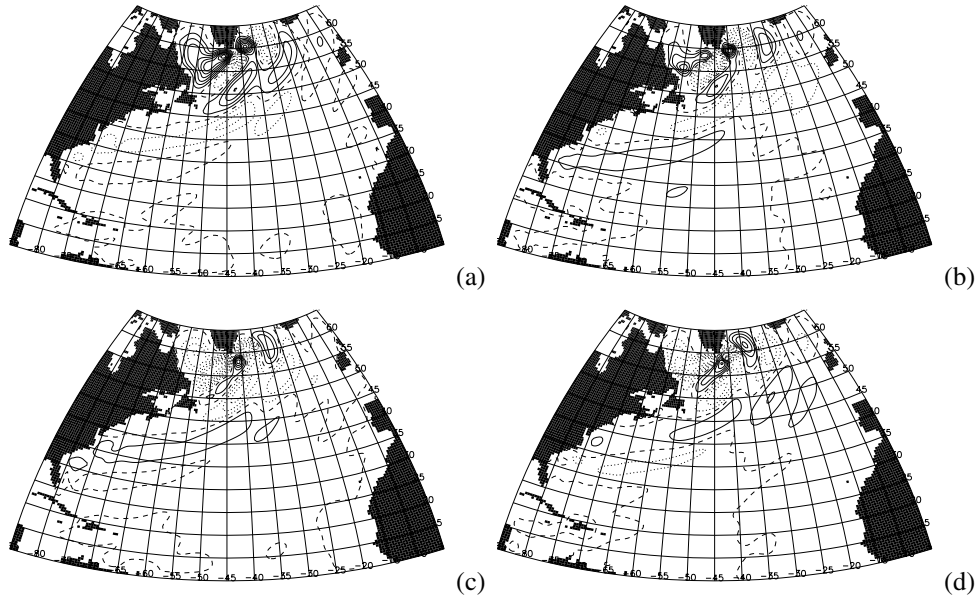


Figure 6.3: RC pair 1-2 of SSH anomalies at several phases of the oscillation. (a) $t = 0$; (b) $t = \pi/2$; (c) $t = \pi$; (d) $t = 3\pi/2$. The SSH anomalies are computed from the 6-year time integration of the barotropic SW model on the North Atlantic domain with the stochastic forcing added to the steady forcing and $E = 1.6 \times 10^{-7}$.

As the trajectory stays more or less close to G_b^S during the first five years of the integration (Fig. 3.11a), which is unstable to the mode associated with the first Hopf bifurcation, we would expect to find also signatures of that mode. Indeed, although the candidate eigenvalue pair (i.e. 11-12) is not statistically significant at the 95% confidence level (Fig. 6.2), the associated RC pair's timescale (6 months) and spatial pattern in the separation region may be linked to the neutral mode at H_1 (section 4.4). However, it also consists of large-scale anomalies in the rest of the basin, which may just be due to the passive response of the model ocean to the stochastic forcing. Because this statistical mode cannot unambiguously be linked to the neutral mode at H_1 , another trajectory has been computed for $E = 2.4 \times 10^{-7}$, which is a value just below the value at which the first Hopf bifurcation occurs (Fig. 3.7a). As initial condition, the unstable steady solution on the lower branch of Fig. 3.7a, with a pattern similar to that of G_b^S (Fig. 3.7b), has been chosen. Again, this state is slightly perturbed into the direction of the most unstable mode.

For this trajectory, the flow is forced by the steady wind forcing and values of the maximum northward transport are shown in Fig. 6.4. The trajectory is attracted towards a limit cycle with a dominant period of about 6 months, coming from the first Hopf bifurcation in Fig. 3.7a. This is confirmed by performing M-SSA on the last 3 years of this trajectory ($N = 72$, $M = 24$, $L = 5$). The dominant RC pair, that explains 93% of the variance, is shown in Fig. 6.5 for four phases during the oscillation. It can be clearly linked to the neutral

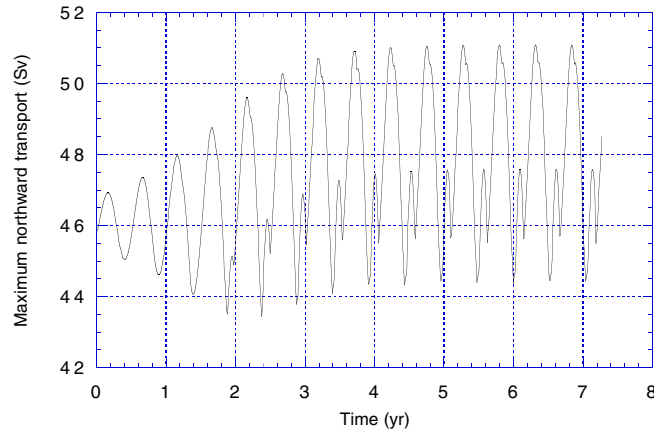


Figure 6.4: Maximum northward transport for the 7-year time integration of the barotropic SW model on the North Atlantic domain with the steady windstress of Fig. 3.4b as forcing and $E = 2.4 \times 10^{-7}$.

mode at H_1 (cf. Fig. 4.10) and the oscillation period of 6 months is the same as that of the neutral mode at H_1 . RC pair 3-4 explains only 4% of the variance, it has a timescale of 3 months and it has its maximum amplitude in the Gulf Stream separation region as well (not shown). Probably, it is due to non-linear self-interaction of the mode coming from H_1 , so it is a harmonic of that mode. The question what happens to the mode coming from the first Hopf bifurcation for lower values of the Ekman number will not be answered, as we would have to compute several other trajectories which are computationally quite expensive. We can hypothesize from the results of chapter 2, however, that the limit cycle probably destabilizes at some stage, but there might be regions in phase-parameter space where the mode is dominantly present again.

6.2.2 North Pacific

The bifurcation diagram (Fig. 3.5a) for the North Pacific indicates the position of two Hopf bifurcation points and the neutral modes becoming unstable at these points have been described in section 5.4. For $E = 1.1 \times 10^{-7}$, which is a value smaller than the values at which the Hopf bifurcations occur (Fig. 3.5a), two trajectories were computed. As initial condition, the unstable steady solution on the upper branch of Fig. 3.5a, with a pattern similar to that of K_c^S (Fig. 3.5c), was chosen. Again, this state is slightly perturbed into the direction of the most unstable mode in the case of the steady wind forcing.

For the first trajectory, the flow is forced by the steady wind forcing and values of the maximum northward transport have been shown in Fig. 3.12a. As we have discussed in section 3.5, there are no transitions to states similar to the other steady state solutions in Fig. 3.5a. Again, we have performed M-SSA on the last 4 years of this time series of SSH fields (sampling time = 0.1 y, $N = 40$, $M = 13$, $L = 10$). It turns out that the dominant RC pair in the time series explains 68% of the variance, and its pattern (Fig. 6.6) can be clearly linked to that of the mode becoming unstable at H_1 (cf. Fig. 5.5). However, its oscillation

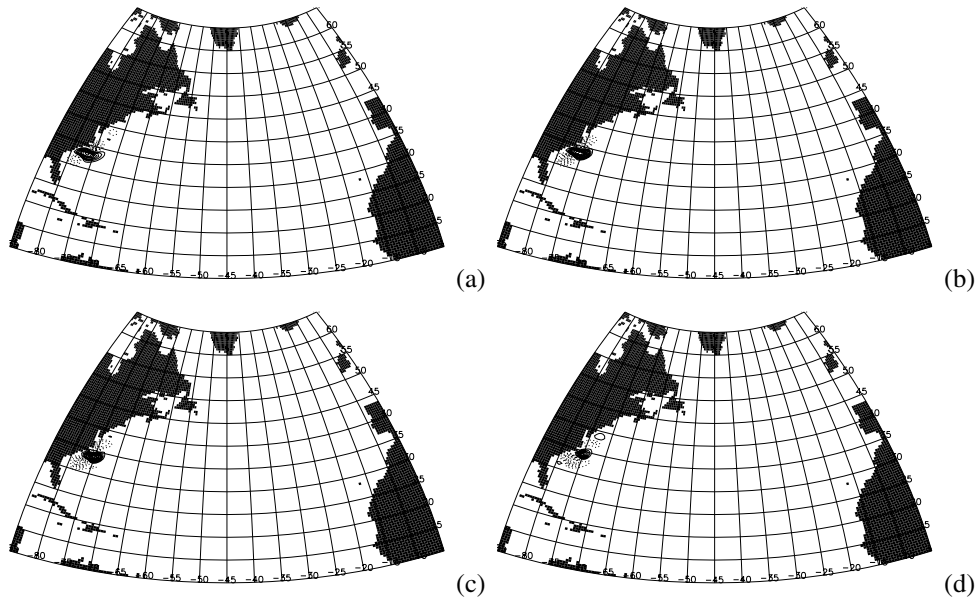


Figure 6.5: RC pair 1-2 of SSH anomalies at several phases of the oscillation. (a) $t = 0$; (b) $t = \pi/4$; (c) $t = \pi/2$; (d) $t = 3\pi/4$. The SSH anomalies are computed from the last 3 years of the 7-year time integration of the barotropic SW model on the North Atlantic domain with the steady windstress of Fig. 3.4b as forcing and $E = 2.4 \times 10^{-7}$.

period of about 4 months is twice as large as that of the neutral mode at H_1 . The next RC pair, i.e. RC 7-8, explains only 5% of the variance, and its pattern (Fig. 6.7) as well as its timescale (3 months) can be clearly linked to that of the mode becoming unstable at H_2 (cf. Fig. 5.6). In Fig. 3.12b the mean SSH field over the last year of the integration has been plotted, the pattern being quite similar to the starting solution.

For the second trajectory, the stochastic forcing is added to the steady forcing and values of R_i (as in (3.7)) have been shown in Fig. 3.13a. In this case, the trajectory stays also relatively close to the unstable steady solution from which it started. The Monte Carlo significance test for M-SSA has been applied again ($N = 198$, $M = 65$, $L = 21$). The result is shown in Fig. 6.8 and red noise turns out to be a good null hypothesis on timescales longer than 1 month. Four data eigenvalue clusters, with associated periods between 1 and 3 months, are indicated as significant. The dominant RC pair explains 7% of the variance, it has a timescale of 3 months and is shown in Fig. 6.9 for four phases during the oscillation. The pattern can neither be linked to the neutral mode at H_1 nor to that at H_2 , but it has similar features as the basin mode in the QG model (cf. Fig. 1.9a). Willebrand et al. (1980) have also found resonant basin modes as the dominant response to stochastic forcing but at intra-monthly frequencies. The next two significant RC pairs cannot be linked to oscillatory instabilities that are known from the linear stability analysis and are therefore not shown. Some of these modes may be stable in the deterministic system and excited by noise.

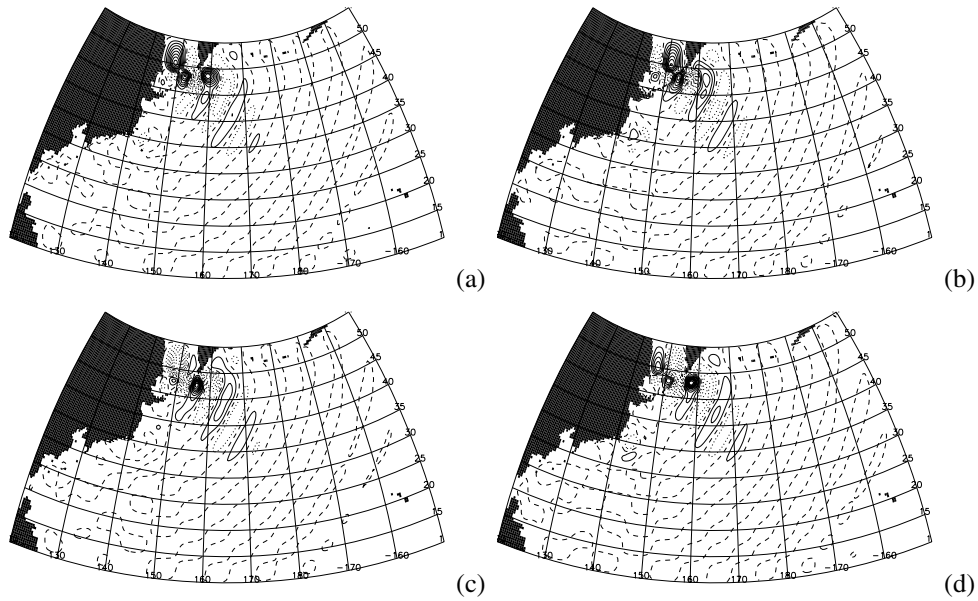


Figure 6.6: (a-d) RC pair 1-2 of SSH anomalies at several phases of the oscillation. (a) $t = 0$; (b) $t = \pi/2$; (c) $t = \pi$; (d) $t = 3\pi/2$. The SSH anomalies are computed from the last 4 years of the 6-year time integration of the barotropic SW model on the North Pacific domain with the steady windstress of Fig. 3.4a as forcing and $E = 1.1 \times 10^{-7}$.

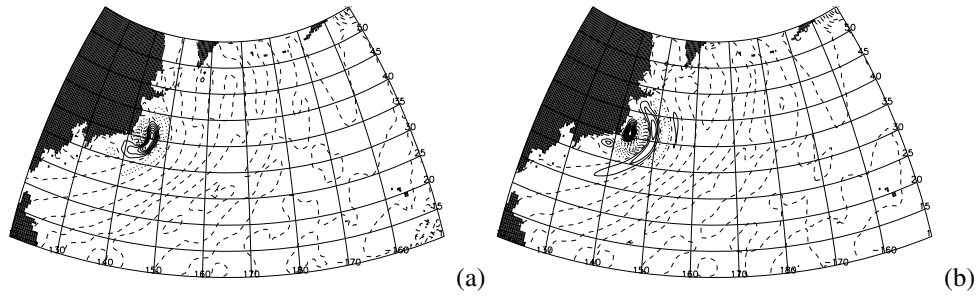


Figure 6.7: (a-b) As Fig. 6.6, but for RC pair 7-8 at two phases of the oscillation. (a) $t = 0$; (b) $t = \pi$.

The fourth significant RC cluster, i.e. RC 23-27, does not consist of a pair but of a quintet (Fig. 6.8b). It explains 6% of the variance, has a timescale of about 2 months and is shown in Fig. 6.10 for four phases during the oscillation. It can be clearly linked to the mode becoming unstable at H_1 (cf. Fig. 5.5), but it has an inverse propagation direction.

As the trajectory stays relatively close to the steady solution similar to K_c^S (Fig. 3.13a), which is only marginally stable to the mode associated with H_3 in the deterministic system for the standard value of D (section 5.4) and which mode may therefore be excited by noise, we

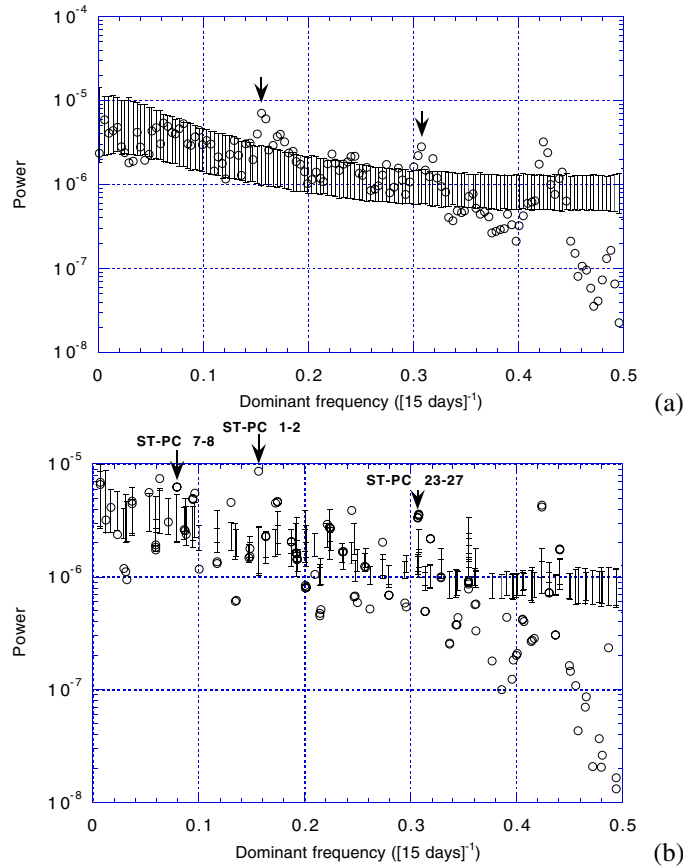


Figure 6.8: Monte Carlo significance test of 15-daily SSH anomalies, using $L = 21$ PCs from a conventional PCA as the input channels. The SSH anomalies are computed from the 8-year time integration of the barotropic SW model on the North Pacific domain with the stochastic forcing added to the steady forcing and $E = 1.1 \times 10^{-7}$. Shown are projections of the SSH anomalies onto (a) the AR(1) null-hypothesis basis and (b) the data-adaptive basis, similar to that in Fig. 6.2, with a 2.6-year window ($M = 65$).

would expect to find also signatures of that mode. Indeed, although the candidate eigenvalue pair (i.e. 7-8) is again not statistically significant at the 95% confidence level (Fig. 6.8), the associated RC pair's timescale (6 months) and spatial pattern in the separation region may be linked to the mode associated with H_3 . However, the pattern also consists of large-scale anomalies in the rest of the basin. Therefore, the statistical mode cannot unambiguously be linked to the marginally stable mode associated with H_3 . Another trajectory, again with the additive stochastic forcing but using a smaller value of the Ekman number ($E = 7.3 \times 10^{-8}$), shows similar spatiotemporal variability (not shown).

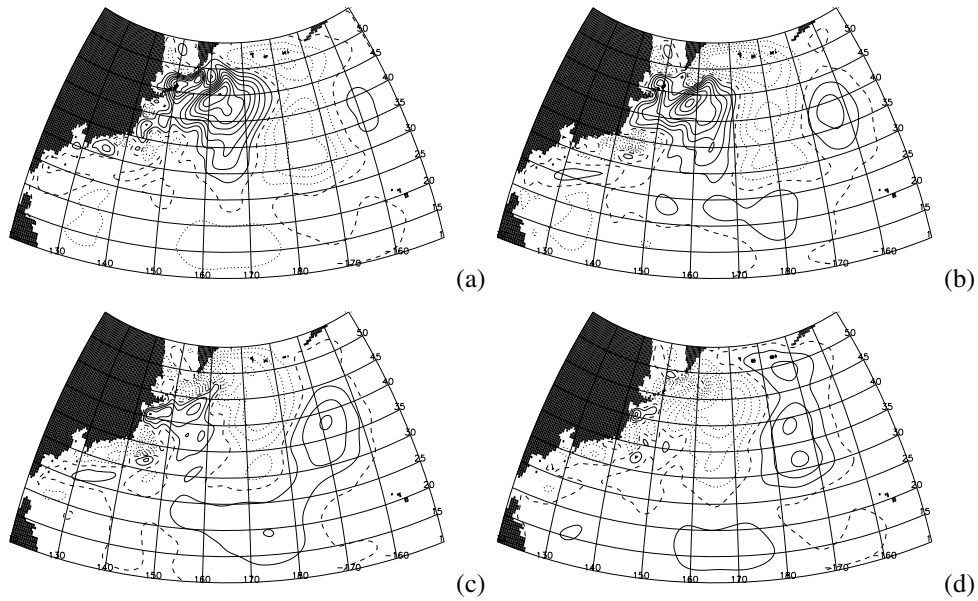


Figure 6.9: (a-d) RC pair 1-2 of SSH anomalies at several phases of the oscillation. (a) $t = 0$; (b) $t = \pi/3$; (c) $t = 2\pi/3$; (d) $t = \pi$. The SSH anomalies are computed from the 8-year time integration of the barotropic SW model on the North Pacific domain with the stochastic forcing added to the steady forcing and $E = 1.1 \times 10^{-7}$.

6.3 Discussion

By performing M-SSA on the transient flows computed with the barotropic SW model we have found signatures of modes known from bifurcation analysis, which remain if noise is added. Besides, this indicates that M-SSA is successful in extracting dynamically meaningful patterns, even for the case with additive noise. Apart from the modes known from bifurcation analysis, we have also found other patterns in the case of additive noise, and these may be caused either by modes deeper in the spectrum that are excited or by resonances. An example is the dominant statistically significant RC pair that was computed from M-SSA of the 8-year time integration of the barotropic SW model on the North Pacific domain with the stochastic forcing added to the steady forcing and $E = 1.1 \times 10^{-7}$ (Fig. 6.9). This mode has similar features as the basin mode in the QG model (cf. Fig. 1.9a), and has been identified as a resonant basin mode in correspondence with the study of Willebrand et al. (1980).

Further, we can conjecture from the results described in this chapter that the stability of the limit cycle appears to be important. The limit cycle in the deterministic case is stable for the North Atlantic and unstable for the North Pacific. When noise is added to the system the dominant statistically significant RC pair for the North Atlantic is still associated with the limit cycle, whereas the dominant statistically significant RC pair for the North Pacific is not associated with the dominant RC pair in the deterministic case. The latter shows up much

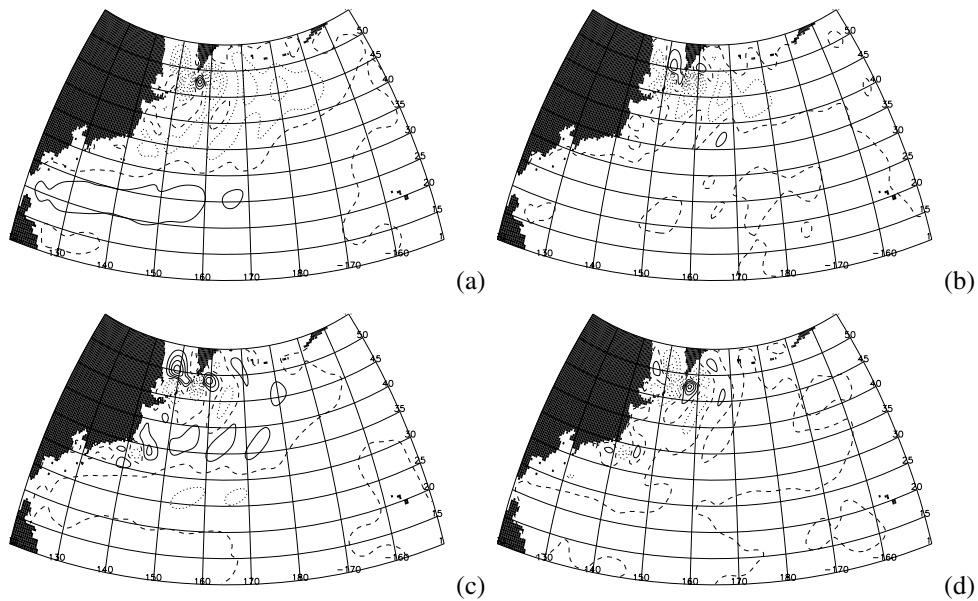


Figure 6.10: (a-d) As Fig. 6.9, but for RC quintet 23-27 at several phases of the oscillation. (a) $t = 0$; (b) $t = 2\pi/3$; (c) $t = 4\pi/3$; (d) $t = 2\pi$.

deeper in the M-SSA eigenvalue spectrum of the model with noise, although statistically significant. These results might indicate that a stable limit cycle "survives" the addition of noise, whereas dominant features of an unstable limit cycle are harder to detect when noise is added to a deterministic system.

The results described in this chapter can also be viewed as a justification *a posteriori* of the use of the Monte Carlo significance test for M-SSA (Allen and Robertson, 1996) for extracting oscillatory behavior from observations. Although the number of degrees of freedom in the barotropic SW model is certainly much smaller than that in the real ocean, the dynamical modes are known from the bifurcation analysis, and the model with the addition of noise can therefore serve as a prototype to test the performance of the Monte Carlo significance test for M-SSA. As the test was successful in labeling some of the dynamical modes as statistically significant, we can conclude that the test is at least capable of identifying some of the dynamical modes in a noisy system.

Chapter 7

Discussion

In this chapter, we will first focus on the implications of the results in this thesis for the behavior of other western boundary currents. As was discussed in chapter 3, the observed (possible) bimodal behavior of the Kuroshio (Gulf Stream) can likely be explained by transitions between multiple steady states. The existence of the multiple steady states has its origin in symmetry breaking in the barotropic quasigeostrophic double gyre rectangular basin model (section 1.3.2). The transitions between the states may be caused by stochastic forcing (Gulf Stream) and/or effects not included in the barotropic shallow-water model, like bottom topography and/or stratification (Kuroshio). In observations indications are found for bimodal behavior of other major western boundary currents as well.

Olson et al. (1988) explored the variability of separation latitudes of the western boundary currents in the South Atlantic Ocean, i.e. the Brazil and Malvinas (or Falkland) Currents (Fig. 1.1), using satellite and drifter data. A histogram of the separation latitude of the Brazil Current for a 3-year time series of NOAA AVHRR High Resolution Picture Transmission (HRPT) digital data shows a significant bimodal distribution (Fig. 7.1; from Olson et al., 1988). The major peak in the histogram of the separation latitude occurs between 36° and $36.5^\circ S$, with a secondary peak between 33.5° and $34^\circ S$. Unlike the Brazil Current, the Malvinas separation is unimodal about the mean separation point (at about $39^\circ S$).

Using a 4-year time series of expendable bathythermograph (XBT) sections between New Zealand and Fiji, Roemmich and Cornuelle (1990) investigated the variability of the subtropical gyre in the South Pacific Ocean. They found two distinct gyre-scale patterns in circulation with a reversal in geostrophic velocity at the sea surface south of Fiji (Fig. 7.2; from Roemmich and Cornuelle, 1990). One of these quasi-steady states was more persistent, being maintained for up to two years, and the transitions from one state to the other were rather abrupt. Whether there is also bimodal behavior of the western boundary current in the South Pacific Ocean, i.e. the East Australian Current (Fig. 1.1), connected with the existence of these two different gyral circulations cannot directly be inferred from their study. Finally, as far as the western boundary current in the Indian Ocean, i.e. the Agulhas Current (Fig. 1.1) is concerned, there are no indications for bimodal behavior to my knowledge.

The hypothesis can be put forward that a similar explanation can be given for the bimodal behavior in the South Atlantic and South Pacific as was given for both the Kuroshio in the

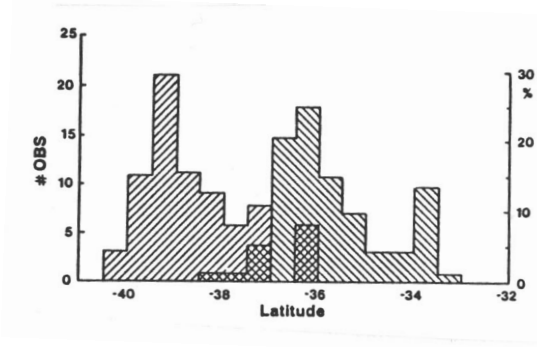


Figure 7.1: Histograms of the separation latitude for a 3-year time series of NOAA AVHRR HRPT digital data. The histogram to the left is for the Malvinas (upper right to lower left hatching) and to the right for the Brazil Current. Cross-hatched areas denote overlapping of the Malvinas and Brazil Current histograms. (From Olson et al., 1988).

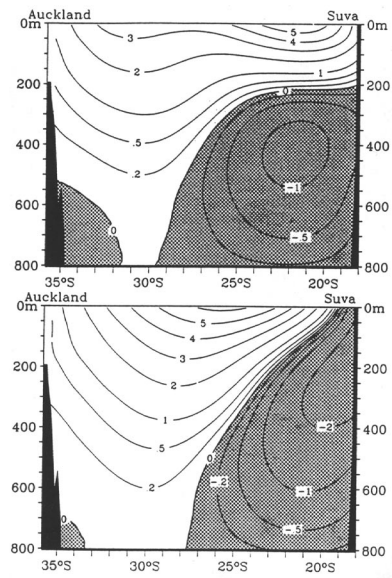


Figure 7.2: The two states of the subtropical gyre in the South Pacific Ocean. Smoothed geostrophic velocity from cruises in 1986 and early 1989 are averaged in Fig. 7.2a, and from cruises in 1987-88 and late 1989-90 in Fig. 7.2b. (From Roemmich and Cornuelle, 1990).

North Pacific and the Gulf Stream in the North Atlantic. However, to test this hypothesis a similar study to the one described in chapter 3 has to be performed.

As was discussed in chapters 4 and 5, the observed variability of the Gulf Stream and the Kuroshio on the 9-month and 7-month timescale, respectively, can be conjectured to be

related to a barotropic instability of the wind-driven gyres in the North Atlantic and North Pacific, respectively. The origin of the barotropic instabilities with near-annual timescales (called the BWBC modes in chapters 4 and 5) seems to be related to the ocean basin modes found in the barotropic quasigeostrophic double gyre rectangular basin model (section 1.3.3). A preliminary study of the observed variability of the other major western boundary currents indicates that there is also statistically significant variability on intermonthly timescales in these currents.

Using the T/P SSH dataset (section 4.2), we have performed a similar analysis for the Brazil and Malvinas Currents, the Agulhas Current and the East Australian Current as has been performed for the Gulf Stream in subsection 4.3.2. The following timescales are indicated as significant by the Monte Carlo test for M-SSA with $N = 148$ and $M = 50$ (Appendix A.1): The Brazil/Malvinas region ($L = 38$) shows dominant statistically significant variability on a timescale of 79 days, the Agulhas Retroflexion region ($L = 34$) on a timescale of 8 months, and the East Australian Current region ($L = 33$) on a timescale of 106 days.

The hypothesis can be put forward that a similar explanation can be given for the 8-month variability in the Agulhas Retroflexion region as was given for the northern hemispheric western boundary currents. Again, to test this hypothesis a similar study to the one described in chapters 4 and 5 has to be performed. However, baroclinic instability processes are expected to play an important role in the variability of the other southern hemispheric western boundary currents on the shorter timescales.

The bifurcation diagrams of the perturbed pitchforks (Figs. 3.5a and 3.7a) and the regime diagrams of the transition to oscillatory behavior (Figs. 4.11a and 5.8a) can be viewed as endpoints for the barotropic models of the North Atlantic and North Pacific. They demonstrate that internal ocean dynamics can give rise to different mean states under the same forcing conditions and that they can induce preference for some frequencies of variability. A similar hierarchy of baroclinic models may be studied in the future to investigate the robustness of the phenomena described in this thesis and the importance of baroclinic instabilities. In a two-layer model, i.e. the simplest model where baroclinic instability can occur, the bottom layer is always motionless in steady state, because it is unforced, and therefore the steady state solutions and the associated perturbed pitchfork bifurcation structure will be unaltered with respect to the barotropic case. However, the addition of the second layer will introduce baroclinic oscillatory instabilities into the system. The latter instabilities have been shown to play an important role in the variability of a "simple" baroclinic model, i.e. the two-layer quasigeostrophic double gyre rectangular basin model (Dijkstra and Katsman, 1997, see also chapter 2). The barotropic basin mode also plays a dominant role in the variability of this model. It has to be sorted out, however, whether the associated BWBC mode, as found in the barotropic shallow-water model on the sphere, still plays a role in the variability of a baroclinic version of the shallow-water model on the sphere. The same holds for the robustness with respect to bottom topography. Ideally, these recommended additional studies may lead to a "unification" theory of the multiple mean paths and internal variability of western boundary currents.

In the remainder of this chapter, we address some of the problems associated with the approach followed in this thesis. As is apparent throughout the thesis, interpretation problems are encountered when trying to connect analyses of variability of the Gulf Stream and the

Kuroshio using three different sources of information. The first source of information has been the observations, which represent the state of the real ocean. However, they also have their complications. The first complication is the complexity of the real ocean, and therefore it is very difficult to formulate physical mechanisms because of the multitude of physical effects which can influence a phenomenon under study. The second complication is the relatively short time series of high resolution data that is available. The third complication is that most of the data are from the surface of the ocean and therefore the vertical structure of the variability (and of the mean state) is unknown. Besides, there is an analysis problem, because we have to use statistical techniques to analyze the data, but the question is to what extent they are capable to extract dynamically relevant modes from the datasets. This question has been addressed in both chapter 2 and chapter 6, where it has been shown, in the context of intermediate ocean models with(out) additive noise, that the dominant (and/or statistically significant) statistical modes have dynamical relevance.

The second source of information has been the output from a global eddy-permitting OGCM, i.e. POCM. OGCMs are state-of-the-art ocean models, but they also have their complications. The first complication is that OGCMs are nearly as complex as the real ocean, and therefore it is again very difficult to formulate physical mechanisms. The second complication is that the mean state of eddy-permitting OGCMs differs from the mean state of the real ocean, in particular with respect to the separation and penetration of western boundary currents. Thus, there is quite a discrepancy between the real ocean and eddy-permitting OGCMs, when studying the behavior of western boundary currents. The situation is much better with respect to truly eddy-resolving OGCMs, but their output has only recently become available (Chassignet et al., 2001; Hurlburt and Hogan, 2000; Smith et al., 2000). Besides, we have again an analysis problem, as described above. However, advantages with regard to observations are that there is a longer time series available and that the vertical structure of the variability can be determined.

The third source of information has been an intermediate ocean model, i.e. the barotropic shallow-water model, which can be considered as an extensively stripped down version of POCM (Dijkstra, 2000). It contains no bottom topography, no baroclinic effects and a very simple parameterization of lateral friction, i.e. downgradient Laplacian diffusion. In other words, it is quite simple when compared to the real ocean or OGCMs, which is an advantage and a disadvantage at the same time. The disadvantage is of course that the discrepancy between the real ocean and such an intermediate ocean model is even larger than between the real ocean and eddy-permitting OGCMs. On the other hand, as we have seen in chapter 3, the correspondence between the patterns of the different states in POCM and the multiple steady states in the barotropic shallow-water model indicates that there is hardly any discrepancy between POCM and the barotropic shallow-water model in this respect. The advantage is that the physics of the variability can be described relatively easily because of the "simplicity" of the model. We also do not have an analysis problem because we are able to perform bifurcation analysis on this type of models. To conclude: despite the interpretation problems mentioned above, the results in chapters 3-5 have indicated that the approach of combining analyses of these three different sources of information has provided a framework to understand the observed bimodality and intermonthly variability of the Gulf Stream and the Kuroshio.

In the near future it will be possible to include also the thermohaline circulation in an

ocean model with quite high horizontal and vertical resolution, such that still steady state solutions and their linear stability can be computed. Then, the connection between the multiple steady state solutions in the wind-driven circulation and those in the thermohaline circulation can be studied, and the robustness of each of them can be considered. Maybe even totally new multiple steady state solutions will be introduced. This is an exciting direction in physical oceanographic research and may ultimately lead to a new (dynamical systems) theory for the global ocean circulation and its variability.

Appendix A

Multivariate time series analysis

The multivariate time series from the datasets and the model output are analyzed with the aid of two multivariate time series analysis techniques designed to empirically infer the characteristics of the space-time variations of a complex system. The following techniques are used in this thesis: multichannel singular spectrum analysis (M-SSA) (Plaut and Vautard, 1994, see section A.1) and principal oscillation patterns (POPs) (Hasselmann, 1988; Von Storch et al., 1995, see section A.2).

A.1 Multi-channel Singular Spectrum Analysis (M-SSA)

The principal technique that we used is M-SSA (Plaut and Vautard, 1994), which produces propagating patterns that are optimal in representing variance. The aim of using M-SSA is to identify coherent space-time patterns, given a regularly sampled archive of maps. M-SSA is mathematically equivalent to extended EOF analysis (EEOF) (Weare and Nasstrom, 1982), but in M-SSA focus is on the temporal structure of the variability, whereas in EEOF the spatial variability is emphasized.

The essentials of the technique are summarized here to introduce terminology used throughout the thesis. Let a dataset \mathbf{X} consist of a multichannel time series $\mathbf{X}_{l,i}$, $i = 1, \dots, N$; $l = 1, \dots, L$, where i represents time and l the channel number. Index l may represent a point number on a specific grid or a principal component (PC) if the data are prefiltered with principal component analysis (PCA). We assume that \mathbf{X} has zero mean and is stationary. By making M lagged copies of \mathbf{X} , the state vector at time i is given by

$$(\mathbf{X}_{1,i+1}, \mathbf{X}_{1,i+2}, \dots, \mathbf{X}_{1,i+M}, \mathbf{X}_{2,i+1}, \dots, \mathbf{X}_{2,i+M}, \dots, \mathbf{X}_{L,i+1}, \dots, \mathbf{X}_{L,i+M}). \quad (\text{A.1})$$

where M is the window length. The cross-covariance matrix \mathbf{T} for a chosen window length M has a general block-Toeplitz form in which each block $\mathbf{T}_{ll'}$ is the lag covariance matrix (with maximum lag M) between channel l and channel l' . The $L \times M$ real eigenvalues λ_k of the symmetric matrix \mathbf{T} are sorted in decreasing order where an eigenvector (referred to as a ST-EOF) \mathbf{E}^k is associated with the k -th eigenvalue λ_k . The \mathbf{E}^k are M -long time sequences of vectors, describing space-time patterns of decreasing importance as their order k increases.

A space-time principal component (referred to as a ST-PC) a^k can be computed by projecting \mathbf{X} onto \mathbf{E}^k ; λ_k is the variance in a^k . In this way, the M-SSA expansion of the original data series is given by

$$\mathbf{X}_{l,i+j} = \sum_{k=1}^{L \times M} a_i^k \mathbf{E}_{lj}^k, j = 1, \dots, M \quad (\text{A.2})$$

PCA (Preisendorfer, 1988) and single-channel singular spectrum analysis (SSA) (Vautard and Ghil, 1989; Vautard et al., 1992) are particular cases of M-SSA: PCA can be derived from M-SSA with $M = 1$, and SSA with $L = 1$.

When two consecutive eigenvalues are nearly equal and the two corresponding \mathbf{E}^k as well as the associated a^k are in quadrature, then the data possess an oscillation whose period is given by that of a^k and whose spatial pattern is that of \mathbf{E}^k (Plaut and Vautard, 1994). The sum in the right-hand side of (A.2), restricted to one or several terms, describes the part of the signal behaving as the corresponding \mathbf{E}^k . The components constructed in this way are called reconstructed components (RCs). In this way, the part of the signal involved with an oscillation can be isolated. The original signal is exactly the sum of all the RCs.

As Allen and Robertson (1996) have pointed out, the presence of an eigenvalue pair is not sufficient grounds to conclude that the data exhibits an oscillation. Moreover, low-frequency eigenvalue pairs, which are entirely due to red noise, will appear high in the eigenvalue rank-order. A Monte Carlo red-noise significance test for M-SSA was therefore constructed (Allen and Robertson, 1996). This is an objective hypothesis test for the presence of oscillations at low signal-to-noise ratios in multivariate data. Rejection of the red-noise null hypothesis using the test should be considered a necessary condition for M-SSA to have detected an oscillation, although in certain situations nonoscillatory processes might also lead to rejection.

The test is built up as follows. Surrogate data segments are constructed by superposing L uncorrelated AR(1) processes having the same variance and lag-1 autocorrelation as the PCs (from standard PCA) of the dataset. Data and surrogate data segments are then projected onto a ST-PC basis of rank $N - M + 1$. This basis is either derived from the data cross-covariance (Toeplitz) matrix (referred to as the data-adaptive basis) or from the AR(1) process cross-covariance matrix (referred to as the null-hypothesis basis). The matrix of projections Λ is:

$$\Lambda \equiv \mathbf{P}^T \mathbf{Y} \mathbf{Y}^T \mathbf{P} \quad (\text{A.3})$$

where \mathbf{Y} is the augmented data matrix of either red-noise surrogate data, or the sample time series, and \mathbf{P} is the ST-PC basis. The method is described in detail by Allen and Robertson (1996).

A.2 Principal Oscillation Pattern (POP) analysis

The basic idea of the POP analysis is to isolate one- and two-dimensional subsystems of the full system that are controlled by linear dynamics (Von Storch et al., 1995). POPs may be regarded as the eigenmodes of the (simple) linear system. POPs are described in detail in Hasselmann (1988) and Von Storch et al. (1995). Here, a short summary of the method is given which is based on Von Storch et al. (1995).

To start with, the following relationship is hypothesized:

$$\mathbf{x}(t+1) = \mathbf{A} \cdot \mathbf{x}(t) + \text{noise} \quad (\text{A.4})$$

Multiplication of (A.4) from the righthand side by the transposed $\mathbf{x}^T(t)$ and taking expectations \mathcal{E} leads to

$$\mathbf{A} = \mathcal{E}[\mathbf{x}(t+1)\mathbf{x}^T(t)] \cdot [\mathcal{E}[\mathbf{x}(t)\mathbf{x}^T(t)]]^{-1} \quad (\text{A.5})$$

In practice, the first expectation value on the righthand side is estimated by deriving the sample lag-1 covariance matrix and the second expectation value is estimated by deriving the sample covariance matrix. In general, the matrix \mathbf{A} is not symmetric and some or all of its eigenvalues λ and eigenvectors \mathbf{p} are complex. The eigenvectors of (A.5) are called principal oscillation patterns.

The eigenvalues $\lambda = |\lambda| \exp(-i\eta)$ always satisfy $|\lambda| < 1$ for a stationary time series. The e-folding (or damping) time $\tau = -1/\ln(|\lambda|)$ characterizes the statistical significance of a POP (Von Storch et al., 1995). The imaginary and real parts of a complex eigenvector describe the temporal evolution of the system in the two-dimensional POP space:

$$\mathbf{p}^i[0] \rightarrow \mathbf{p}^r[T/4] \rightarrow -\mathbf{p}^i[T/2] \rightarrow -\mathbf{p}^r[3T/4] \rightarrow \mathbf{p}^i[T] \rightarrow \dots \quad (\text{A.6})$$

The period $T = 2\pi/\eta$ is the time needed to fulfil one complete cycle in (A.6).

If all eigenvalues are different (which is usually the case), then the eigenvectors form a linear basis. So, the state \mathbf{x} at any time t may be uniquely expressed in terms of the eigenvectors \mathbf{p}_j :

$$\mathbf{x}(t) = \sum_j z_j(t) \cdot \mathbf{p}_j \quad (\text{A.7})$$

The time coefficients z are called POP coefficients. They were derived by a least-squares fit of the data \mathbf{x} by minimizing

$$\| \mathbf{x} - \sum_j z_j \mathbf{p}_j \| \quad (\text{A.8})$$

The rate of variance explained by the POPs is not optimal and has to be calculated from the POP coefficients.

Appendix B

Dynamical systems analysis*

B.1 Bifurcation theory

Many introductory textbooks to bifurcation theory and its applications are available nowadays (Kuznetsov, 1995; Nayfeh and Balachandran, 1995). The simplest type of bifurcations are those which involve only one parameter in the system under study and are called codimension-one bifurcations. An example of such a simple bifurcation occurs in the one-dimensional autonomous dynamical system

$$\frac{dx}{dt} = f(x, \mu) = \mu x - x^3 \quad (\text{B.1})$$

where x is the state variable and μ the control parameter. For $\mu < 0$, there is only one stationary state (or fixed point) $\bar{x} = 0$ as a solution of $f(\bar{x}, \mu) = 0$. For $\mu > 0$, three fixed points exist, i.e. $\bar{x} = 0$, $\bar{x} = \sqrt{\mu}$ and $\bar{x} = -\sqrt{\mu}$ and hence the number of fixed points changes as μ crosses zero. The latter two solutions are symmetry related, because $f(-x, \mu) = -f(x, \mu)$.

To determine the stability of the fixed points, the evolution of perturbations \tilde{x} on \bar{x} are considered. Substituting $x = \bar{x} + \tilde{x}$ into (B.1), linearizing in \tilde{x} leads to

$$\frac{d\tilde{x}}{dt} = (\mu - 3\bar{x}^2)\tilde{x} \quad (\text{B.2})$$

and hence growth of perturbations is determined by the sign of the eigenvalues σ of the Jacobian matrix $\partial f / \partial x = \mu - 3\bar{x}^2$. For $\bar{x} = 0$, it follows that $\sigma = \mu$, indicating that $\bar{x} = 0$ is stable for $\mu < 0$ but unstable for $\mu > 0$. For both additional fixed points existing at $\mu > 0$, it follows that $\sigma = -2\mu$, showing that these are both stable.

The bifurcation diagram of the system (B.1) is shown in Fig. B.1a as a graph of x against μ where stable fixed points are drawn and unstable states are dashed. At $\mu = 0$, the system undergoes a qualitative change, since the number of fixed points changes from one to three. The corresponding bifurcation is called a pitchfork bifurcation. Two other bifurcation

*This appendix is based on section 2 of Dijkstra, H. A., M. J. Schmeits, and C. A. Katsman, 1999: Internal variability of the North Atlantic wind-driven ocean circulation. *Surveys in Geophysics*, **20**, 463-503.

diagrams, those for the saddle node bifurcation and the transcritical bifurcation are shown in Figs. B.1b and B.1c, respectively, and the simplest one-dimensional system (as in (B.1)) which exhibits such a bifurcation is provided in the caption.

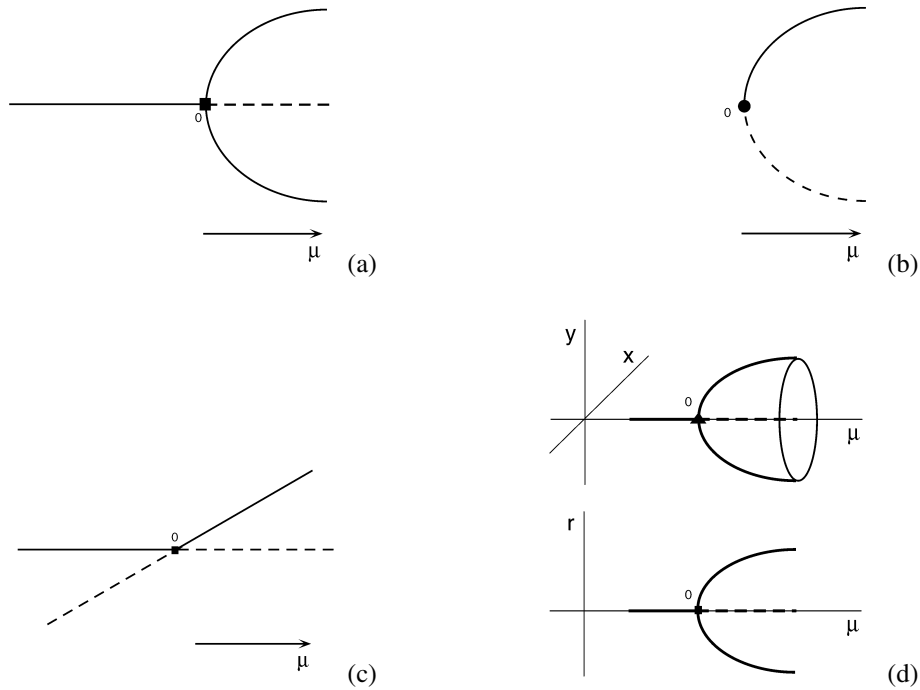


Figure B.1: Overview of the codimension-one bifurcations and the simplest dynamical system exhibiting this bifurcation. The convention is to mark pitchfork and transcritical bifurcations with a filled square, saddle node bifurcations by a filled circle and Hopf bifurcations with a filled triangle. In the plots, the origin of the coordinate frame is labelled with a "0". (a) Pitchfork bifurcation, $dx/dt = \mu x - x^3$ (b) Saddle node bifurcation, $dx/dt = \mu - x^2$; this bifurcation is also referred to as a limit point. (c) Transcritical bifurcation, $dx/dt = \mu x - x^2$ (d) Hopf bifurcation, $dx/dt = \mu x - \omega y - x(x^2 + y^2)$; $dy/dt = \mu y + \omega x - y(x^2 + y^2)$. From Dijkstra et al. (1999).

Whereas in the previous bifurcations, the number or stability of fixed points changes as a parameter is varied, it is also possible that the character of the solution changes from stationary to oscillatory as a single parameter is changed. An example of a simple dynamical system undergoing such a transition is the two-dimensional autonomous system given by

$$\frac{dx}{dt} = \mu x - \omega y - x(x^2 + y^2) \quad (\text{B.3a})$$

$$\frac{dy}{dt} = \mu y + \omega x - y(x^2 + y^2) \quad (\text{B.3b})$$

By the transformation $x = r \cos \theta$ and $y = r \sin \theta$, (B.3) transfers into

$$\frac{dr}{dt} = \mu r - r^3 \quad (\text{B.4a})$$

$$\frac{d\theta}{dt} = \omega \quad (\text{B.4b})$$

Comparing (B.4a) with (B.1), it can be seen that a pitchfork bifurcation occurs at $\mu = 0$ in the (r, μ) plane. For $\mu < 0$, only one stable fixed point exists, which corresponds to a stationary solution of the original equations (B.3). However, for $\mu > 0$ the stable nontrivial fixed points of (B.4a) now correspond to a periodic solution of the original equations (B.3) with a frequency ω , according to (B.4b). The bifurcation diagram for this case is shown in Fig. B.1d. For $\mu < 0$ only one stable stationary state exists, but for $\mu > 0$ this state becomes unstable and a stable periodic solution appears. At $\mu = 0$ the system undergoes a qualitative change and the bifurcation is called a Hopf bifurcation.

The examples above illustrate that multiple steady states can occur due to a pitchfork, transcritical or saddle node bifurcation, whereas a Hopf bifurcation may introduce temporal variability in the system. More complicated bifurcations may arise when more than one parameter in the system is changed. For example, codimension-two bifurcations may arise through intersection of paths of codimension-one bifurcations as a second parameter is varied. Complicated behavior is usually found, when parameters are increased to large values above criticality and different routes from regular to chaotic behavior have been identified (Nayfeh and Balachandran, 1995).

B.2 Numerical methods

If one wants to use this systematic methodology on meaningful models of the ocean circulation, one must be able to determine at least the most simple bifurcation points. In recent years, much effort has been put in the development of techniques to follow branches of steady states and the calculation of bifurcation points in parameter space (Dijkstra et al., 1995) for dynamical systems of very large dimension (up to 10^5). At the moment, one is able to carry out a bifurcation analysis for a large class of models of intermediate complexity.

The basic technique for bifurcation analysis is comprised of two main pieces: a continuation method to advance one step on a branch of steady states as a parameter is varied, and an eigenvalue solver to determine the linear stability of the computed steady state. Each intermediate complexity model used in this thesis can be written in operator form as follows

$$\mathcal{M} \frac{\partial \mathbf{u}}{\partial t} + \mathcal{L} \mathbf{u} + \mathcal{N}(\mathbf{u}) = \mathbf{F} \quad (\text{B.5})$$

where \mathcal{L} , \mathcal{M} are linear operators, \mathcal{N} is a nonlinear operator, \mathbf{u} is the vector of dependent quantities and \mathbf{F} contains the forcing of the system. Appropriate boundary conditions also have to be prescribed.

To determine the steady states $\bar{\mathbf{u}}$ of the system of equations when parameters are changed, the problem

$$\mathcal{L} \bar{\mathbf{u}} + \mathcal{N}(\bar{\mathbf{u}}) = \mathbf{F} \quad (\text{B.6})$$

has to be solved. When this set of partial differential equations is discretized by some finite difference, spectral or finite element method, a system of nonlinear algebraic equations of the form

$$\mathbf{G}(\mathbf{x}, \mathbf{p}) = 0 \quad (\text{B.7})$$

emerges. Here \mathbf{x} is a d -dimensional vector (typically $d = \mathcal{O}(10^4 - 10^5)$) consisting of the unknowns at the gridpoints, \mathbf{p} is the p -dimensional vector of parameters and \mathbf{G} is a nonlinear mapping from $R^d \times R^p \rightarrow R^d$. To determine branches of steady solutions of (B.7) as one of the parameters (say μ) is varied, the pseudo-arclength method is often used (Keller, 1977; Seydel, 1994). The branches $(\mathbf{x}(s), \mu(s))$ are parametrized by an "arclength" parameter s and an additional equation is obtained by an approximation of the normalization condition of the tangent, i.e.

$$\dot{\mathbf{x}}_0^T (\mathbf{x} - \mathbf{x}_0) + \dot{\mu}_0 (\mu - \mu_0) - \Delta s = 0 \quad (\text{B.8})$$

where (\mathbf{x}_0, μ_0) is a known starting solution or a previously computed point on a particular branch, Δs is the steplength and the dot indicates differentiation to s . To follow steady solutions along branches in parameter space, an Euler-Newton scheme is used (Seydel, 1994).

When a steady state is determined, the linear stability of the solution is considered and transitions that mark qualitative changes such as transitions to multiple equilibria (pitchfork or saddle node bifurcations) or periodic behavior (Hopf bifurcations) can be detected. To determine the linear stability of the steady state, perturbations $\tilde{\mathbf{u}}$ are considered. With $\mathbf{u} = \bar{\mathbf{u}} + \tilde{\mathbf{u}}$, linearizing (B.5) around $\bar{\mathbf{u}}$ and separating $\tilde{\mathbf{u}} = \hat{\mathbf{u}}e^{\sigma t}$ gives an eigenvalue problem of the form

$$(\mathcal{L} + \mathcal{N}_u)\hat{\mathbf{u}} = -\sigma\mathcal{M}\hat{\mathbf{u}} \quad (\text{B.9})$$

where \mathcal{N}_u is the derivative of the operator \mathcal{N} with respect to \mathbf{u} . In most applications, discretization of this eigenvalue problem leads to a generalized algebraic eigenvalue problem of the form

$$\mathcal{A}\hat{\mathbf{x}} = \sigma\mathcal{B}\hat{\mathbf{x}} \quad (\text{B.10})$$

where \mathcal{A} and \mathcal{B} are non-symmetric matrices. Bifurcations are detected from crossings of σ with the imaginary axis. Solution techniques for these problems are presented in Dijkstra et al. (1995).

A nice spin-off of steady state solvers is the immediate availability of an implicit time integration scheme. Using a time step Δt , and a time index n , a class of two-level schemes can be written as

$$\mathcal{M} \frac{\mathbf{u}^{n+1} - \mathbf{u}^n}{\Delta t} + \Theta \mathbf{G}(\mathbf{u}^{n+1}) + (1 - \Theta) \mathbf{G}(\mathbf{u}^n) = 0 \quad (\text{B.11})$$

For $\Theta = 1$, this is the Backward Euler scheme and for $\Theta = \frac{1}{2}$, it is the Crank-Nicholson scheme. The equations for \mathbf{u}^{n+1} are solved by the Newton-Raphson technique and lead to large systems of nonlinear algebraic equations, similar to those for the steady state computation. It is well-known that the Crank-Nicholson scheme is unconditionally stable for linear equations. However, the time step is still constrained by accuracy.

Bibliography

- Allen, M. R. and A. W. Robertson, 1996: Distinguishing modulated oscillations from coloured noise in multivariate datasets. *Climate Dyn.*, **12**, 775 – 784.
- Auer, S. J., 1987: Five-year climatological survey of the Gulf Stream system and its associated rings. *J. Geophys. Res.*, **92**, 11709 – 11726.
- Bane, J. M. and W. K. Dewar, 1988: Gulf Stream bimodality and variability downstream of the Charleston bump. *J. Geophys. Res.*, **93**, 6695–6710.
- Beckmann, A. C. W., C. W. Böning, J. Köberle, and J. Willebrand, 1994: Effects of increased horizontal resolution in a simulation of the North-Atlantic ocean. *J. Phys. Oceanogr.*, **24**, 326–344.
- Berloff, P. S. and S. P. Meacham, 1998: On the stability of the wind-driven circulation. *J. Mar. Res.*, **56**, 937–993.
- Blanke, B., J. D. Neelin, and D. Gutzler, 1997: Estimating the effect of stochastic wind stress forcing on ENSO irregularity. *J. Climate*, **10**, 1473–1486.
- Bretherton, C. S., C. Smith, and J. M. Wallace, 1992: An intercomparison of methods for finding coupled patterns in climate data. *J. Climate*, **5**, 541–560.
- Broecker, W. S., 1991: The Great Ocean Conveyor. *Oceanography*, **4**, 79–89.
- Broecker, W. S., D. M. Peteet, and D. Rind, 1985: Does the ocean-atmosphere system have more than one stable mode of operation? *Nature*, **315**, 21–26.
- Bryan, F. O., C. W. Böning, and W. R. Holland, 1995: On the midlatitude circulation in a high-resolution model of the North-Atlantic. *J. Phys. Oceanogr.*, **25**, 289–305.
- Cessi, P. and G. R. Ierley, 1995: Symmetry-breaking multiple equilibria in quasi-geostrophic, wind-driven flows. *J. Phys. Oceanogr.*, **25**, 1196–1205.
- Chao, S.-Y., 1984: Bimodality of the Kuroshio. *J. Phys. Oceanogr.*, **14**, 92–103.
- Charney, J. G. and G. R. Flierl, 1981: Ocean analogues of large-scale atmospheric motions. In *Evolution of Physical Oceanography*, Warren, B. and Wunsch, C., editors. The MIT Press, 504-548.

- Chassignet, E. P., Z. D. Garraffo, R. D. Smith, and H. E. Hurlburt, 2001: High resolution Gulf Stream modeling. *Submitted to Geophys. Res. Letters*.
- Cox, M., 1987: An eddy-resolving model of the ventilated thermocline: time-dependence. *J. Phys. Oceanogr.*, **17**, 1044–1056.
- Dengg, J., A. Beckmann, and R. Gerdes, 1996: The Gulf Stream separation problem. In *The warmwatersphere of the North Atlantic Ocean*, Kraus, W. A., editor. Borntraeger, 253–290.
- Dijkstra, H. A., 2000: *Nonlinear Physical Oceanography*. Kluwer Academic Publishers, 456 + xviii pp.
- Dijkstra, H. A. and C. A. Katsman, 1997: Temporal variability of the wind-driven quasi-geostrophic double gyre ocean circulation: Basic bifurcation diagrams. *Geophys. Astrophys. Fluid Dyn.*, **85**, 195–232.
- Dijkstra, H. A. and M. J. Molemaker, 1999: Imperfections of the North-Atlantic wind-driven ocean circulation: continental geometry and windstress shape. *J. Mar. Res.*, **57**, 1–28.
- Dijkstra, H. A., M. J. Molemaker, A. J. Van der Ploeg, and E. F. F. Botta, 1995: An efficient code to compute nonparallel flows and their linear stability. *Comp. Fluids*, **24**, 415–434.
- Dijkstra, H. A., M. J. Schmeits, and C. A. Katsman, 1999: Internal variability of the North Atlantic wind-driven ocean circulation. *Surveys in Geophysics*, **20**, 463–503.
- Fofonoff, N. P., 1954: Steady flow in a frictionless homogeneous ocean. *J. Mar. Res.*, **13**, 254–262.
- Fuglister, F. C., 1972: Cyclonic rings formed by the Gulf Stream 1965–1966. In *Studies in physical oceanography*, Gordon, A. L., editor, volume 1. Gordon and Breach, New York, 137–168.
- Ghil, M. and S. Childress, 1987: *Topics in geophysical fluid dynamics: atmospheric dynamics, dynamo theory and climate dynamics*. Springer-Verlag.
- Golubitsky, M. and D. Schaeffer, 1985: *Singularities and groups in bifurcation theory*. Springer-Verlag, 533 pp.
- Gordon, A. L., 1986: Interocean exchange of thermocline water. *J. Geophys. Res.*, **91**, 5037–5046.
- Greenslade, D., D. Chelton, and M. Schlax, 1997: The midlatitude resolution capability of sea level fields constructed from single and multiple satellite altimeter datasets. *J. Atmos. Oceanic Technol.*, **14**, 849–870.
- Grove, J. M., 1988: *The Little Ice Age*. Methuen, London and New York.
- Guckenheimer, J. and P. Holmes, 1983: *Nonlinear oscillations, dynamical systems and bifurcations of vector fields*. Springer-Verlag.

- Hansen, D., 1970: Gulf Stream meanders between Cape Hatteras and the Grand Banks. *Deep-Sea Res.*, **17**, 495–511.
- Hasselmann, K., 1976: Stochastic climate models. Part I. Theory. *Tellus*, **28**, 473–485.
- Hasselmann, K., 1988: PIPs and POPs: The reduction of complex dynamical systems using principal interaction and oscillation patterns. *J. Geophys. Res.*, **93**, 11015–11021.
- Hellerman, S. and M. Rosenstein, 1983: Normal monthly wind stress over the world ocean with error estimates. *J. Phys. Oceanogr.*, **13**, 1093–1104.
- Hogg, N. G., R. S. Pickart, R. M. Hendry, and W. J. Smethie, 1986: The northern recirculation gyre of the Gulf Stream. *Deep-Sea Res.*, **33**, 1139–1165.
- Holland, W. R. and P. B. Rhines, 1980: An example of eddy-induced ocean circulation. *J. Phys. Oceanogr.*, **10**, 1010–1031.
- Hughes, C. W., 2000: A theoretical reason to expect inviscid western boundary currents in realistic oceans. *Ocean Modelling*, **2**, 73–83.
- Hurlburt, H. E. and P. J. Hogan, 2000: Impact of $1/8^\circ$ to $1/64^\circ$ resolution on Gulf Stream model-data comparisons in basin-scale subtropical Atlantic Ocean models. *Dyn. Atmos. Ocean.*, **32**, 283–329.
- Hurlburt, H. E., A. J. Wallcraft, W. J. Schmitz, P. J. Hogan, and E. J. Metzger, 1996: Dynamics of the Kuroshio/Oyashio current system using eddy-resolving models of the North Pacific Ocean. *J. Geophys. Res.*, **101**, 941–976.
- Jiang, S., F. F. Jin, and M. Ghil, 1995: Multiple equilibria and aperiodic solutions in a wind-driven double gyre, shallow water model. *J. Phys. Oceanogr.*, **25**, 764–786.
- Johns, W. E., T. J. Shay, J. M. Bane, and D. R. Watts, 1995: Gulf Stream structure, transport and recirculation near 68° W. *J. Geophys. Res.*, **100**, 817–838.
- Jones, M., M. Allen, T. Guymmer, and M. Saunders, 1998: Correlations between altimetric sea surface height and radiometric sea surface temperature in the South Atlantic. *J. Geophys. Res.*, **103**, 8073–8087.
- Katsman, C. A., 2001: *Internal variability of the wind-driven ocean circulation*. PhD thesis, Utrecht University, Utrecht, the Netherlands.
- Katsman, C. A., H. A. Dijkstra, and S. S. Drijfhout, 1998: The rectification of wind-driven flow due to its instabilities. *J. Mar. Res.*, **56**, 559–587.
- Kawabe, M., 1986: Transition processes between the three typical paths of the Kuroshio. *J. Oceanogr. Soc. Japan*, **42**, 174–191.
- Kawabe, M., 1995: Variations of current path, velocity, and volume transport of the Kuroshio in relation with the large meander. *J. Phys. Oceanogr.*, **25**, 3103–3117.

- Keller, H. B., 1977: Numerical solution of bifurcation and nonlinear eigenvalue problems. In *Applications of bifurcation theory*, Rabinowitz, P. H., editor. Academic Press, New York, USA.
- Kelly, K. A., M. J. Caruso, S. Singh, and B. Qiu, 1996: Observations of atmosphere-ocean coupling in midlatitude western boundary currents. *J. Geophys. Res.*, **101**, 6295–6312.
- Kelly, K. A., S. Singh, and R. Huang, 1999: Seasonal variations of sea surface height in the Gulf Stream region. *J. Phys. Oceanogr.*, **29**, 313–327.
- Kuznetsov, Y. A., 1995: *Elements of applied bifurcation theory*. Springer-Verlag.
- Le Traon, P. Y., F. Nadal, and N. Ducet, 1998: An improved mapping method of multi-satellite altimeter data. *J. Atmos. Oceanic Technol.*, **25**, 522–534.
- Lee, T. and P. Cornillon, 1995: Temporal variation of meandering intensity and domain-wide lateral oscillations of the Gulf Stream. *J. Geophys. Res.*, **100(C7)**, 13,603–13,613.
- Lee, T. and P. Cornillon, 1996: Propagation and growth of Gulf Stream meanders between 75° and 45° W. *J. Phys. Oceanogr.*, **26**, 225–241.
- Legeckis, R. V., 1976: The influence of bottom topography on the path of the Gulf Stream at latitude 31 N from NOAA's satellite imagery (abstract). *Eos Trans. AGU*, **57**, 260.
- Legras, B. and M. Ghil, 1985: Persistent anomalies, blocking, and variations in atmospheric predictability. *J. Atmos. Sci.*, **42**, 433–471.
- Maltrud, M. E., R. D. Smith, A. J. Semtner, and R. C. Malone, 1998: Global eddy-resolving ocean simulations driven by 1985-1995 atmospheric winds. *J. Geophys. Res.*, **103**, 30825–30853.
- Masuda, A., 1982: An interpretation of the bimodal character of the stable Kuroshio path. *Deep-Sea Res.*, **29**, 471–484.
- Maul, G., P. DeWitt, A. Yanaway, and S. Baig, 1978: Geostationary satellite observations of Gulf Stream meanders: infrared measurements and time series analysis. *J. Geophys. Res.*, **83(C12)**, 6123–6135.
- McWilliams, J. C., 1996: Modeling the ocean general circulation. *Ann. Rev. Fluid Mechanics*, **28**, 215–248.
- Miller, A. J., W. R. Holland, and M. C. Hendershott, 1987: Open-ocean response and normal mode excitation in an eddy-resolving general circulation model. *Geophys. Astrophys. Fluid Dyn.*, **37**, 253–278.
- Munk, W., 1950: On the wind-driven ocean circulation. *J. Meteor.*, **7**, 79–93.
- Nayfeh, A. H. and B. Balachandran, 1995: *Applied nonlinear dynamics*. John Wiley.

- Olson, D. B., O. B. Brown, and S. R. Emmerson, 1983: Gulf Stream frontal statistics from Florida Straits to Cape Hatteras derived from satellite and historical data. *J. Geophys. Res.*, **88**, 4569–4577.
- Olson, D. B., G. P. Podesta, R. H. Evans, and O. B. Brown, 1988: Temporal variations in the separation of Brazil and Malvinas Currents. *Deep-Sea Res.*, **35**, 1971–1990.
- Özgökmen, T. M., E. P. Chassignet, and A. M. Paiva, 1997: Impact of wind forcing, bottom topography, and inertia on midlatitude jet separation in a quasigeostrophic model. *J. Phys. Oceanogr.*, **27**, 2460–2476.
- Pedlosky, J., 1987: *Geophysical Fluid Dynamics*. Springer-Verlag, New York.
- Pedlosky, J., 1996: *Ocean Circulation Theory*. Springer, New York, Berlin.
- Peixoto, J. P. and A. H. Oort, 1992: *Physics of Climate*. AIP Press.
- Plaut, G. and R. Vautard, 1994: Spells of low-frequency oscillations and weather regimes in the Northern Hemisphere. *J. Atmos. Sci.*, **51**, 210–236.
- Preisendorfer, R. W., 1988: *Principal Component Analysis in Meteorology and Oceanography*. Elsevier, Amsterdam.
- Prohaska, J., 1976: A technique for analyzing the linear relationships between two meteorological fields. *Mon. Wea. Rev.*, **104**, 1345–1353.
- Qiu, B. and T. M. Joyce, 1992: Interannual variability in the mid- and low-latitude western North Pacific. *J. Phys. Oceanogr.*, **22**, 1062–1079.
- Qiu, B. and W. Miao, 2000: Kuroshio path variations south of Japan: bimodality as a self-sustained internal oscillation. *J. Phys. Oceanogr.*, **30**, 2124–2137.
- Reynolds, R. W. and T. M. Smith, 1994: Improved global sea surface temperature analysis using optimum interpolation. *J. Climate*, **7**, 929–948.
- Richardson, P., 1980: Benjamin Franklin and Timothy Folger's first printed chart of the Gulf Stream. *Science*, **207**, 643–645.
- Roemmich, D. and B. Cornuelle, 1990: Observing the fluctuations of gyre-scale ocean circulation: a study of the subtropical South Pacific. *J. Phys. Oceanogr.*, **20**, 1919–1934.
- Schmeits, M. J. and H. A. Dijkstra, 2000: Physics of the 9-month variability in the Gulf Stream region: combining data and dynamical systems analyses. *J. Phys. Oceanogr.*, **30**, 1967–1987.
- Semtner, A. J. and R. M. Chervin, 1992: Ocean general circulation from a global eddy-resolving model. *J. Geophys. Res.*, **97**, 5493–5550.
- Seydel, R., 1994: *Practical bifurcation and stability analysis: from equilibrium to chaos*. Springer-Verlag, New York, USA.

- Smith, R. D., M. E. Maltrud, F. O. Bryan, and M. W. Hecht, 2000: Numerical simulation of the North Atlantic Ocean at $\frac{1}{10}^\circ$. *J. Phys. Oceanogr.*, **30**, 1532–1561.
- Speich, S., H. Dijkstra, and M. Ghil, 1995: Successive bifurcations in a shallow-water model applied to the wind-driven ocean circulation. *Nonl. Proc. Geophys.*, **2**, 241–268.
- Stammer, D., R. Tokmakian, A. Semtner, and C. Wunsch, 1996: How well does a $1/4^\circ$ global circulation model simulate large-scale oceanic observations? *J. Geophys. Res.*, **101**, 25779–25811.
- Stern, M. E., 1975: Minimal properties of planetary eddies. *J. Mar. Res.*, **33**, 1–13.
- Stommel, H., 1948: The westward intensification of wind-driven ocean currents. *Trans. Amer. Geophysical Union*, **29**, 202–206.
- Sura, P., K. Fraedrich, and F. Lunkeit, 2001: Regime transitions in a stochastically forced double-gyre model. *J. Phys. Oceanogr.*, **31**, 411–426.
- Taft, B. A., 1972: Characteristics of the flow of the Kuroshio south of Japan. In *Kuroshio, physical aspects of the Japan current*, Stommel, H. and Yoshida, K., editors. University of Washington Press, 165–214.
- Tansley, C. E. and D. P. Marshall, 2000: On the influence of bottom topography and the Deep Western Boundary Current on Gulf Stream separation. *J. Mar. Res.*, **58**, 297–325.
- Trenberth, K., J. Olson, and W. Large, 1989: A global ocean wind stress climatology based on ECMWF analyses. Technical report, National Center for Atmospheric Research, Boulder, Colorado.
- Vautard, R., 1995: Patterns in time: SSA and M-SSA. In *Analysis of climate variability*, Von Storch, H. and Navarra, A., editors. Springer, 259–279.
- Vautard, R. and M. Ghil, 1989: Singular spectrum analysis in nonlinear dynamics with applications to paleoclimatic time series. *Physica D*, **35**, 395–424.
- Vautard, R., P. Yiou, and M. Ghil, 1992: Singular spectrum analysis: A toolkit for short, noisy chaotic signals. *Physica D*, **58**, 95–126.
- Vazquez, J., 1993: Observations on the long-period variability of the Gulf Stream downstream of Cape Hatteras. *J. Geophys. Res.*, **98(C11)**, 20133–20147.
- Vazquez, J., V. Zlotnicki, and L.-L. Fu, 1990: Sea level variabilities in the Gulf Stream between Cape Hatteras and 50° W: A Geosat study. *J. Geophys. Res.*, **95(C10)**, 17957–17964.
- Von Storch, H., G. Buerger, R. Schnur, and J.-S. von Storch, 1995: Principal oscillation patterns: a review. *J. Climate*, **8**, 377–400.
- Vossepoel, F., 1995: Processing of altimeter and infrared radiometer data for eddy detection in the Gulf Stream. Master's thesis, Delft University of Technology, Delft, the Netherlands.

- Wang, L. and C. Koblinsky, 1995: Low-frequency variability in regions of the Kuroshio Extension and the Gulf Stream. *J. Geophys. Res.*, **100(C9)**, 18313–18331.
- Wang, L. and C. Koblinsky, 1996: Annual variability of the subtropical recirculations in the North Atlantic and North Pacific: a Topex/Poseidon study. *J. Phys. Oceanogr.*, **26**, 2462–2479.
- Wang, L., C. Koblinsky, and S. Howden, 1998: Annual and intra-annual sea level variability in the region of the Kuroshio Extension from TOPEX/POSEIDON and Geosat altimetry. *J. Phys. Oceanogr.*, **28**, 692–711.
- Weare, B. C. and J. N. Nasstrom, 1982: Examples of extended empirical orthogonal function analyses. *Mon. Wea. Rev.*, **110**, 481–485.
- Willebrand, J., S. G. H. Philander, and R. C. Pacanowski, 1980: The oceanic response to large-scale atmospheric disturbances. *J. Phys. Oceanogr.*, **10**, 411–429.

Summary

The large-scale ocean circulation is driven both by windstress forcing and by fluxes of heat and freshwater at the ocean-atmosphere surface. At midlatitudes, the most prominent features of the mainly wind-driven surface circulation are the large coherent circulation patterns (gyres) (chapter 1: Fig. 1.1). In the North Atlantic and North Pacific a relatively strong anti-cyclonic (subtropical) gyre is seen and a relatively weak cyclonic (subpolar) gyre. Along the western boundaries of the ocean basins strong currents exist. These currents are referred to as western boundary currents and the poleward-flowing currents carry warm water from the tropics to midlatitudes. Hence, they play an important role in the climate system. The major western boundary currents in the North Atlantic and North Pacific are called the Gulf Stream and Kuroshio, respectively.

For a long time, observations have been pointing out that the Kuroshio displays bimodal meandering behavior off the southern coast of Japan (chapter 1: Fig. 1.4). For the Gulf Stream, weakly and strongly deflected paths near the coast of South Carolina have been observed (chapter 1: Fig. 1.3). This suggests that bimodal behavior may occur in the Gulf Stream as well, although less pronounced than in the Kuroshio. Apart from this bimodality, both currents show dominant variability on intermonthly timescales.

Within a hierarchy of equivalent barotropic models on a β -plane (chapter 1), it is found that multiple mean flows are dynamically possible for the North Atlantic wind-driven circulation. Besides, the modes of intermonthly variability arising as instabilities on the mean states are closely linked within this hierarchy of models. Therefore, the two main questions addressed in this thesis (chapters 3-5) are:

- Can the observed (possible) bimodal behavior of the Kuroshio (Gulf Stream) be explained by transitions between multiple steady states?
- Can the observed variability of the Gulf Stream and the Kuroshio on intermonthly timescales be explained by instabilities of the wind-driven ocean circulation?

The approach that is followed in this thesis to answer these questions is to combine data analysis of observations and Ocean General Circulation Models, and dynamical systems analysis of intermediate complexity models. This approach is new, and therefore the connection between both types of analyses is studied in this thesis as well. The associated question is to what extent the statistical techniques are capable to extract dynamically relevant modes from the datasets. This question is addressed in both chapter 2 and chapter 6, where it is shown, in

the context of intermediate ocean models with(out) additive noise, that the dominant (and/or statistically significant) statistical modes have dynamical relevance.

In chapter 3 evidence is given from a high resolution simulation of the Parallel Ocean Climate Model (POCM) and from intermediate complexity models to support the hypothesis that multiple mean paths of both the Kuroshio and the Gulf Stream are dynamically possible. These paths are found as multiple steady states in a barotropic shallow-water model using techniques of numerical bifurcation theory. In POCM, transitions between similar mean paths are found, with the patterns having similarity to the ones in the observations as well. To study whether atmospheric noise can induce transitions between the multiple steady states, a stochastic component is added to the annual mean wind stress forcing in the barotropic shallow-water model and differences between the transition behavior in the Gulf Stream and Kuroshio are considered.

In chapter 4 dominant patterns of variability are determined using multivariate time series analyses of nonseasonal altimeter data and sea surface temperature observations of the North Atlantic, and more specific the Gulf Stream region. A statistically significant propagating mode of variability with a timescale close to 9 months is found, the latter timescale corresponding to dominant variability found in earlier studies. In addition, output from POCM is analyzed, which also displays variability on a timescale of 9 months, although not statistically significant at the 95% confidence level. The vertical structure of this 9-month mode turns out to be approximately equivalent barotropic. Following the idea that this mode is due to internal ocean dynamics, instabilities on the mean states are determined within the same barotropic shallow-water model as used in chapter 3. Within this model, the three different mean flow paths of the Gulf Stream all become unstable to oscillatory modes. For reasonable values of the parameters, an oscillatory instability having a timescale of 9 months is found. This mode is called the barotropic western boundary current (BWBC) mode. The connection between results from the bifurcation analysis, from the analysis of the observations and from the analysis of the POCM output, is explored in more detail and leads to the conjecture that the 9-month variability is related to a barotropic instability of the wind-driven gyres.

In chapter 5 a similar study to the one in chapter 4 is performed, but for the 7-month variability in the Kuroshio region. The conjecture from chapters 4 and 5, i.e. that the near-annual variability of the Kuroshio (Gulf Stream) is caused by a barotropic instability of the mean Kuroshio (Gulf Stream) path near its separation, is supported by:

- the corresponding features of the near-annual statistical mode from the sea surface height observations, from the POCM output and the BWBC mode in the shallow-water model for each current separately
- the expected close dynamical correspondence between the Kuroshio and the Gulf Stream
- the connection between the separate modes (from either the observations, the POCM output or the shallow-water model) of both currents
- the correspondence in timescales between the statistical modes of both currents despite the difference in size of the North Atlantic and North Pacific basins.

Samenvatting

De grootschalige oceaancirculatie wordt zowel geforceerd door de windschuifspanning als door uitwisseling van warmte en vocht (neerslag minus verdamping) aan het oceaana-atmosfeer grensvlak. Op gematigde breedtes zijn grote coherente circulatiepatronen ("gyres") zichtbaar (hoofdstuk 1: Fig. 1.1) als onderdelen van de hoofdzakelijk windgedreven oppervlaktecirculatie. In de Noord-Atlantische en Noordelijke Stille Oceaan is een relatief sterke anticyclonale (subtropische) "gyre" aanwezig en een relatief zwakke cyclonale (subpolaire) "gyre". Langs de westranden van de oceaانبekkenen bestaan sterke stromingen. Deze stromingen worden westelijke grenslaagstromingen genoemd en de poolwaarts gerichte stromingen transporteren warm water van de tropen naar gematigde breedtes. Zodoende spelen ze een belangrijke rol in het klimaatsysteem. De belangrijkste westelijke grenslaagstromingen in de Noord-Atlantische en Noordelijke Stille Oceaan worden respectievelijk de Golfstroom en de Kuroshio genoemd.

Langdurige waarnemingen laten zien dat de Kuroshio bimodaal meanderend gedrag vertoont ten zuiden van Japan (hoofdstuk 1: Fig. 1.4). Voor de Golfstroom zijn zowel zwak als sterk deflecterende paden waargenomen voor de kust van South Carolina (hoofdstuk 1: Fig. 1.3). Dit suggereert dat de Golfstroom wellicht ook bimodaal gedrag vertoont, hoewel minder uitgesproken dan de Kuroshio. Naast deze bimodaliteit laten beide stromingen ook dominante variabiliteit op intermaandelijke tijdschalen zien.

Een hiërarchie van equivalent barotrope oceaanmodellen op een β -vlak (hoofdstuk 1) heeft laten zien dat meervoudige evenwichten dynamisch mogelijk zijn voor de Noord-Atlantische windgedreven oceaancirculatie. Daarnaast zijn de modi van intermaandelijke variabiliteit, die ontstaan als instabiliteiten op de gemiddelde toestanden, sterk met elkaar verbonden binnen deze hiërarchie van modellen. Uit het bovenstaande volgen nu de twee hoofdvragen die in dit proefschrift (hoofdstuk 3-5) behandeld worden:

- Kan het waargenomen (mogelijk) bimodaal gedrag van de Kuroshio (Golfstroom) verklaard worden door overgangen tussen meervoudige evenwichten?
- Kan de waargenomen variabiliteit van de Golfstroom en de Kuroshio op intermaandelijke tijdschalen verklaard worden door instabiliteiten van de windgedreven oceaancirculatie?

De aanpak die in dit proefschrift gevolgd is om deze vragen te beantwoorden is het combineren van data-analyse van observaties en algemene oceaancirculatiemodellen, en dynamische systeemanalyse van intermediaire oceaanmodellen. Deze aanpak is nieuw en daarom

wordt de connectie tussen beide analysetypes ook bestudeerd in dit proefschrift. De geassocieerde vraag is in welke mate de statistische technieken in staat zijn om dynamisch relevante modi uit de datasets te extraheren. Deze vraag wordt behandeld in zowel hoofdstuk 2 als hoofdstuk 6, waar gedemonstreerd wordt, in de context van intermediaire oceaanmodellen zonder en met additieve ruis, dat de dominante (en/of statistisch significante) statistische modi dynamische relevantie hebben.

In hoofdstuk 3 wordt de hypothese dat meervoudige evenwichtspaden van zowel de Kuroshio als de Golfstroom dynamisch mogelijk zijn, ondersteund door resultaten uit een hoge resolutie simulatie van het Parallel Ocean Climate Model (POCM) en uit intermediaire oceaanmodellen. Deze paden zijn als meervoudige evenwichtstoestanden gevonden in een barotroop ondiep-water model met behulp van technieken uit de numerieke bifurcatietheorie. In POCM zijn overgangen tussen twee verschillende gemiddelde paden gevonden, welke zowel lijken op de meervoudige evenwichtstoestanden in het barotroop ondiep-water model als op de twee verschillende gemiddelde paden in de waarnemingen. Om te onderzoeken of atmosferische ruis overgangen tussen meervoudige evenwichten kan induceren, is er een stochastische component toegevoegd aan de jaargemiddelde windschuifspanningsforcering in het barotrope ondiep-water model en de verschillen in het transitiegedrag tussen de Golfstroom en de Kuroshio worden beschouwd.

In hoofdstuk 4 zijn dominante patronen van variabiliteit bepaald met behulp van multivariate tijdreeksanalyses van satellietwaarnemingen van de hoogte en temperatuur van het zeeoppervlak in de Noord-Atlantische Oceaan en meer specifiek de Golfstroom regio. Er is een statistisch significante propagerende modus van variabiliteit met een tijdschaal van ongeveer 9 maanden gevonden, waarbij deze tijdschaal correspondeert met dominante variabiliteit die in eerdere studies gevonden is. Daarnaast is de uitvoer van POCM geanalyseerd, welke ook variabiliteit op een tijdschaal van 9 maanden laat zien, hoewel deze niet statistisch significant is op het 95% betrouwbaarheidsniveau. De verticale structuur van deze 9-maanden modus blijkt ongeveer equivalent barotroop te zijn. Uitgaande van het idee dat deze modus het gevolg is van interne oceaandynamica zijn instabiliteiten op de gemiddelde toestanden bepaald binnen hetzelfde barotrope ondiep-water model als gebruikt in hoofdstuk 3. Binnen dit model worden de drie verschillende evenwichtstoestanden van de Golfstroom allemaal instabiel ten opzichte van oscillatorische modi. Voor realistische parameterwaarden is een oscillatorische instabiliteit met een tijdschaal van 9 maanden gevonden. Deze modus wordt de "barotropic western boundary current" (BWBC) modus genoemd. De connectie tussen de resultaten van de bifurcatie-analyse, van de analyse van de satellietwaarnemingen en van de POCM uitvoer is nader beschouwd en leidt tot het vermoeden dat de 9-maanden variabiliteit gerelateerd is aan een barotrope instabiliteit van de windgedreven "gyres".

In hoofdstuk 5 wordt een analoge studie aan die in hoofdstuk 4 beschreven, maar dan voor de 7-maanden variabiliteit in de Kuroshio regio. Het vermoeden van de hoofdstukken 4 en 5, namelijk dat de bijna-jaarlijkse variabiliteit van de Kuroshio (Golfstroom) veroorzaakt wordt door een barotrope instabiliteit van het gemiddelde Kuroshio (Golfstroom) pad dichtbij het separatiepunt, wordt ondersteund door:

- de overeenkomstige kenmerken van de bijna-jaarlijkse statistische modus uit de satellietwaarnemingen van de hoogte van het zeeoppervlak, uit de POCM uitvoer en de BWBC modus in het ondiep-water model voor elke stroming afzonderlijk

- de verwachte dynamische correspondentie tussen de Kuroshio en de Golfstroom
- de connectie tussen de afzonderlijke modi (of uit de waarnemingen, of uit de POCM uitvoer of uit het ondiep-water model) voor beide stromingen
- de correspondentie in tijdschalen tussen de statistische modi van beide stromingen ondanks het verschil in afmetingen tussen de Noord-Atlantische Oceaan en de Noordelijke Stille Oceaan.

Dankwoord

Nu mijn proefschrift af is, is het tijd om die mensen te bedanken die bijgedragen hebben tot de totstandkoming ervan.

In de allereerste plaats wil ik mijn co-promotor, Henk Dijkstra, bedanken voor zijn enthousiaste en leerzame begeleiding. Zijn grote betrokkenheid bij mijn werk heb ik erg gewaardeerd. Henk heeft met het NWO-PIONIER project "Stability and variability of the climate system" een nieuwe onderzoekslijn opgezet. Ik hoop dat mijn werk, als onderdeel ervan, een bijdrage levert aan de promotie van deze lijn bij de fysisch oceanografische gemeenschap. In de tweede plaats wil ik mijn promotor, Will de Ruijter, bedanken voor zijn interesse in mijn onderzoek en zijn kritische lezing van het manuscript. Hij heeft mij ook geattendeerd op de prachtige satellietfoto, die een plaats op de omslag heeft gekregen.

Further, I am grateful to Robin Tokmakian (Naval Postgraduate School (NPS), Monterey, California, USA) for supplying the POCM output, and for giving me the opportunity to visit NPS. Besides, I would like to thank Andy Robertson (UCLA, Los Angeles, California, USA) for providing the M-SSA software. Verder wil ik Jeroen Molemaker bedanken voor het ontwikkelen van het SW model, Frank Selten (KNMI, NL) voor het ter beschikking stellen van de data-analyse software van het KNMI, en Femke Vossepoel en Mathijs Schouten voor het ter beschikking stellen van de interpolatie software voor de TOPEX/Poseidon data. Mathijs wil ik ook nog bedanken voor de handige data-analyse programmaatjes, waarvan ik dankbaar gebruik heb gemaakt. Piet Jonker en Marcel Portanger waren onmisbaar om respectievelijk Unix en Mac problemen op te lossen. De ondersteuning door het (helaas steeds wisselende) secretariaat mag hier ook niet onvermeld blijven.

Met mijn parttime kamergenoot Caroline Katsman heb ik veel van gedachten gewisseld. Ik denk dat we beide geprofitteerd hebben van het feit dat onze promotie-onderwerpen zo dicht bij elkaar lagen. Bovendien werd ze, doordat zij een stukje op mij voor lag, in de slotfase een vraagbaak voor mij voor alles wat op organisatorisch vlak met het promoveren te maken had. Daarnaast had ze meermalen een oplossing voor diverse LaTeX perikelen, waardoor ik niet steeds opnieuw het wiel hoefde uit te vinden. Further, I would like to thank my former office room-mate, Nathalie Ritemard, for the many interesting discussions both about science and about differences between France and the Netherlands. Hierbij wil ik ook de andere mensen van de PIONIER-groep van Henk bedanken voor de prettige werksfeer. In het bijzonder wil ik nog Ernst van der Avoird, Mathijs Schouten en Laura de Steur noemen, met wie ik in Jan Primus, de Vogel of de Zaak de ins en outs van het promovendusschap en andere belangrijke zaken in het leven heb besproken.

Mijn paranimfen, Harriën van Dijk en Yvonne Cox-Vleeshouwers, vroegen zich soms af

of ze niet meer konden doen ter voorbereiding van de "grote dag". Dat hoefde niet, want ik heb jullie niet tot paranimf benoemd om mij het organisatorische werk uit handen te nemen, maar omdat ik erg hecht aan onze vriendschap. Dit wil niet zeggen dat mijn andere vrienden mij niet dierbaar zijn, integendeel, maar er kunnen er nu eenmaal maar twee paranimf zijn. Tot slot wil ik mijn ouders en mijn broer Bart bedanken voor hun interesse, steun en liefde.

Maurice Schmeits

Utrecht, april 2001

Curriculum Vitae

Maurice Schmeits werd geboren op 4 maart 1971 te Sittard. In 1983 ging hij naar het Serviam Lyceum te Sittard en behaalde het Gymnasium- β diploma in 1989. In datzelfde jaar ging hij Geofysica studeren aan de Universiteit Utrecht en behaalde het propedeutisch examen van deze opleiding in 1990. Aansluitend begon hij aan de doctoraalopleiding Meteorologie en Fysische Oceanografie. Het diploma van deze opleiding behaalde hij in 1995, waarna hij toegevoegd onderzoeker werd aan het Instituut voor Marien en Atmosferisch onderzoek Utrecht (IMAU). In 1996 begon hij als onderzoeker in opleiding aan zijn promotie-onderzoek bij het IMAU met dr. ir. H.A. Dijkstra als begeleider. Dit onderzoek maakte deel uit van het NWO-PIONIER project "Stability and variability of the climate system" en de resultaten ervan staan beschreven in dit proefschrift. Sinds februari 2001 is Maurice werkzaam als postdoc bij het IMAU op bovengenoemd NWO-PIONIER project.